Structure and seismic signature of subsidiary damage around natural and artificial fractures

Catherine Gillian Hatton

Thesis submitted for the degree of Doctor of Philosophy

University of Edinburgh

1992

Abstract

The observed fractal nature of both fault length distributions and earthquake magnitude-frequency distributions suggests that there may be a direct relationship between the structure of active fault systems and the resulting seismicity. In much previous theoretical work, a positive correlation between the exponent D from the fracture length distribution and the seismic or AE b-value has been inferred from a simple dislocation model of the seismic source. The main aim of this project was to test this relation quantitatively, for tensile fracture, using results from controlled laboratory experiments. Field work on natural tensile fracture systems was also carried out to test that the results from the artificial fracture in the laboratory were relevant to the natural fractures that were being simulated.

First, a series of double torsion tensile tests on crystalline rock, carried out at the Fracture Mechanics Laboratory, University College London, is described. A program of tests was carried out on two rock types, granodiorite and granite of different grain size, to test the effects of rock type and specimen size on the laboratory results. The main controlling variables, used during the tests, that affect the results, are the presence or absence of fluid, at ambient temperature and pressure, in the crack tip environment, and stress intensity (and hence crack velocity). Microseismic acoustic emissions (AE) were monitored during subcritical crack growth under controlled conditions of constant stress intensity, K_I, and quantitative structural analyses of the resulting fracture patterns were carried out on the same specimens. AE microseismicity is found to reflect different aspects of microcrack propagation in the laboratory. AE b-values range from 1.0 to 2.4 and vary depending upon fluid presence at the crack tip. The greater the fluid-rock interaction, the higher the relative proportion of smaller seismic sources (thus producing a higher b-value). The b-values correlate negatively with the normalised stress intensity K_I / K_{IC}. At

high stress intensities and high crack velocity, the chemical environment has less influence on crack propagation. The structure of the microfracture systems in the laboratory specimens is quantified using the crack length distribution exponent D, which ranges from 1.0 to 2.25. Fluid presence also has a first order effect on the nature of the fracture systems. The exponent D is shown to correlate positively, and with statistical significance, with the AE b-value. This implies that small fractures produce low amplitude AE. Rock type and specimen size appear to have a second order effect on this relation. The relation between 2-dimensional areal exponents and 3-dimensional volumetric exponents is also discussed.

Results from one field season mapping in the Krafla Fissure Swarm, north east Iceland, suggest that the artificial fracture from the laboratory tests do provide a good analogy to natural tensile fracture. Length-width relations measured from the natural fracture populations indicate that there is a lower limit to the scale invariance of such fracture systems. This has specific significance to fault growth models.

Acknowledgements

I would like to thank the two main supervisors of this project, Ian Main at Edinburgh University and Phil Meredith at University College London, for their exceptional encouragement and enthusiasm throughout the three years. I must also thank Agust Gudmundsson at the Nordic Volcanological Institute, Reykjavik, for his encouragement in getting me to Iceland, and his valuable help and advice during the fieldwork. Thanks also must go to Bob Cheeney for his help with the Scotland fieldwork and collection of the rock samples, and also for his advice on statistics.

In addition, I would like to thank the following: at University College London: Chris Stuart for his help with the LOCAN-AT and for providing programs for AE analysis, Pete Sammonds for initial advice on the project, Sean Holding for help with specimen preparation, John Bowles and Steve Boon for helping me with the loading machine and fixing it when I managed to break it (twice); at Edinburgh: Diana Baty for her patient help with photography; and in general: Sigyn Eríksdóttir for her field assistance in Iceland, Dave Sayer for his help in the field in Scotland, and Patience Cowie for her helpful suggestions.

Financial support was provided by the Natural Environment Research Council (award GT4/89/GS/033).

Finally, I would like to thank my family for putting up with me through all this.

Contents

Symbol notation

a half crack length (section 1.3.2; equations 1.6 and 1.7); crack length (section 2.3.1; equation 2.2); specimen notch length (section 2.3.1); constant (equation 1.11)

α dimensionless parameter (section 1.3.2; equation 1.7)

A area of displacement surface (section 1.4.2; equation 1.12); AE amplitude (section 1.4.5; equation 1.18)

AE acoustic emission

b AE or seismic b-value (equations 1.11; 1.18; 3.1)

β finite specimen width correction (section 2.3.2; equation 2.3)

B constant (section 2.3.1; equation 2.1; figure 2.5)

c constant (equation 1.11)

C constant (section 2.3.1; equation 2.1)

d thickness of double torsion specimen (Chapter 2); constant (section 1.4.2; equation 1.16); slip at a point on a fault (section 1.4)

d_n specimen thickness within guide groove (Chapter 2)

d_c critical slip at a point on a fracture (section 1.4)

D generalised dimension - length distribution exponent

D_A area dimension (2-D)

D_V volume dimension (3-D)

D_H Hausdorff-Besicovitch fractal dimension

D_T topological Euclidean dimension

D_{BC} Box-counting fractal dimension

D_{CL} Cluster analysis fractal dimension

ε strain

E Young's modulus

ϕ dimensionless parameter (section 1.3.2; equation 1.7)

G strain energy release rate (equation 1.6, 1.8)

G_C critical strain energy release rate

G_M mechanical energy release rate (equation 1.5)

G_R energy rate resistance (equation 1.5)

η constant (section 4.2)

H activation energy

k compliance

K_I stress intensity factor (mode I)

K_{IC} critical stress intensity factor

L length (of a fracture or fault); length of double torsion specimen (section 2.1.1)

m magnitude

m_L local magnitude

m_S surface wave magnitude

m_b body wave magnitude

μ rigidity/shear modulus

M_o seismic moment

n subcritical crack growth index

N number

p pore fluid pressure

P applied load

r yardstick length (fractal analysis); Pearson's product-moment correlation coefficient (statistical analysis)

R gas constant

σ stress ($\sigma_1 > \sigma_2 > \sigma_3$)

σ_e effective stress

σ_T tensile stress

σb error on b-value (90% confidence) (section 3.1.2; equation 3.2)

SE standard error (66% confidence)

τ period (seismic wave)

τ_D duration time

τ_R rise time

T absolute temperature

u average slip (on a fault)

ua accumulated slip

U total free energy

U_m mechanical energy

$-U_p$ potential energy

U_ε elastic strain energy

U_s surface energy

ν Poisson's ratio

V rupture velocity (crack extension velocity)

V_R rupture velocity of a crack front (section 1.4.3)

V_S slip velocity (section 1.4.3)

W width of double torsion specimen (Chapter 2)

W_m semi moment arm distance of double torsion loading geometry (Chapter 2)

y displacement

$\dot{y}$ displacement rate

Chapter 1 Introduction

1.1 General introduction

This study is concerned with the mechanisms of tensile rock fracture both in the laboratory and in the earth. Of particular interest are the effects of fluid-rock interactions in promoting the subcritical crack growth associated with time-dependent failure at low strain rates. Tensile fracture involves any discrete break in a rock mass where the movement is an opening perpendicular to the strike, with no significant shear displacement. In the earth, this includes veins, joints and most dykes as well as tensile fractures. Tensile failure, in the form of dilatant microcracking, is also thought to be significant in earthquake nucleation, even though the dominant tectonic movement may be shear (Scholz, 1990). Therefore, tensile fractures are abundant and important natural features, although their study has lagged far behind that of shear fractures and faults. Open fractures are also significant in both the storage and the movement of fluids within the earth's crust, and so control many metamorphic reactions and the dissolution and deposition of hydrothermal minerals. Thus, the fluid-rock interactions which are allowed by tensile opening are fundamental to the understanding of the combined processes of fracture and fluid transport. Examples include the pressure solution of stressed minerals, and stress corrosion cracking of minerals weakened by chemical processes at crack tips.

Much previous work on rock fracture has concentrated on either the structure of the fracture systems, usually observed in the field (for example, Wise, 1964; Segall and Pollard, 1983; Hancock, 1985; Delaney et al., 1986; Engelder, 1987; Mastin and Pollard, 1988), or the seismicity produced during fracture, either natural earthquake data in the field (for example, Kanamori and Anderson, 1975; Kanamori, 1978) or

artificially induced acoustic emission from laboratory testing (for example, Meredith and Atkinson, 1983; Meredith et al., 1990). It is only recently that the possible association between the structure of fault systems and earthquake seismicity has been recognised and inferred to be significant, (for example by Main et al., 1990; Scholz, 1990). It is the purpose of this study to integrate these usually isolated aspects of brittle failure in a quantitative way. This is done by comparing the scaling properties of the structure of the fracture system with the seismicity produced during fracture propagation. A series of tensile fracture experiments, where the main controlling variables were stress intensity and fluid presence, was carried out to allow contemporaneous examination of the seismicity and structure from a single incremental fracture system on the same test specimen. The seismicity was recorded in the form of acoustic emissions, and the structure quantified by examination of the geometry of the fracture system. Tensile fracture was chosen as the mode of failure since the open geometry of the tensile test specimens facilitates the direct examination of the structure of the microcracks, without producing the extra damage to the specimen that is necessarily involved in sectioning compressional specimens for analysis. This work is then compared both with natural earthquake seismicity and a field study of natural tensile fracture systems.

This is an interdisciplinary project which involves aspects of experimental fracture mechanics, structural geology and seismology. In this chapter, basic concepts from these essential disciplines are introduced and discussed, as well as the broader background concerning the project as a whole. An overview of the methods used to integrate the structure and seismicity of fracture is then given, followed by a brief summary of the contribution of this project to the general objective of relating structural and seismological observations.

1.2 Fractal geometry of fault systems and earthquakes

Scale invariance and self-similarity

It is common in any geological investigation to observe identical features over a range of different scales, so that a scale bar is essential to determine the relative size of the feature. This phenomenon is termed scale invariance. Virtually all structures that occur in deformed rocks may be found at scales ranging from millimeters to kilometers. For example, a joint system may contain joints of lengths varying from tens of millimeters to hundreds of meters (Segall and Pollard, 1983; Segall, 1984). Major joints can be tens of kilometers in length. Folds of all types also occur at a wide range of scales, although a specific study into this scale invariance has not yet been documented. However, recently the scale invariance of fracture systems has been widely recognised. For example figure 1.1 illustrates the scale invariance of shear fault systems (after Shaw and Gartner, 1986). The maps of four shear systems at various scales, from the millimeter scale of a shear box experiment (Tchalenko, 1970) to the kilometer scale of regional shear faults in California (Howard et al., 1978), show a distinct visual similarity; they are all dominated by a single throughgoing macrofracture with an array of more minor fractures. In this thesis, the hypothesis that tensile fracture exhibits a similar scale invariance is evaluated, allowing the possibility of scaling up laboratory fracture results to the natural earth.

The concept of self-similarity has a slightly stricter definition. For a system to show a self-similar geometry, it should contain an intrinsic dimensionality that is evident when the system is observed at any scale. The recognition of these characteristics is useful if such systems are to be quantified. The geometric property of self-similarity is fundamental to the definition of the recently developed quantitative concept of fractals, which is discussed in the next section.

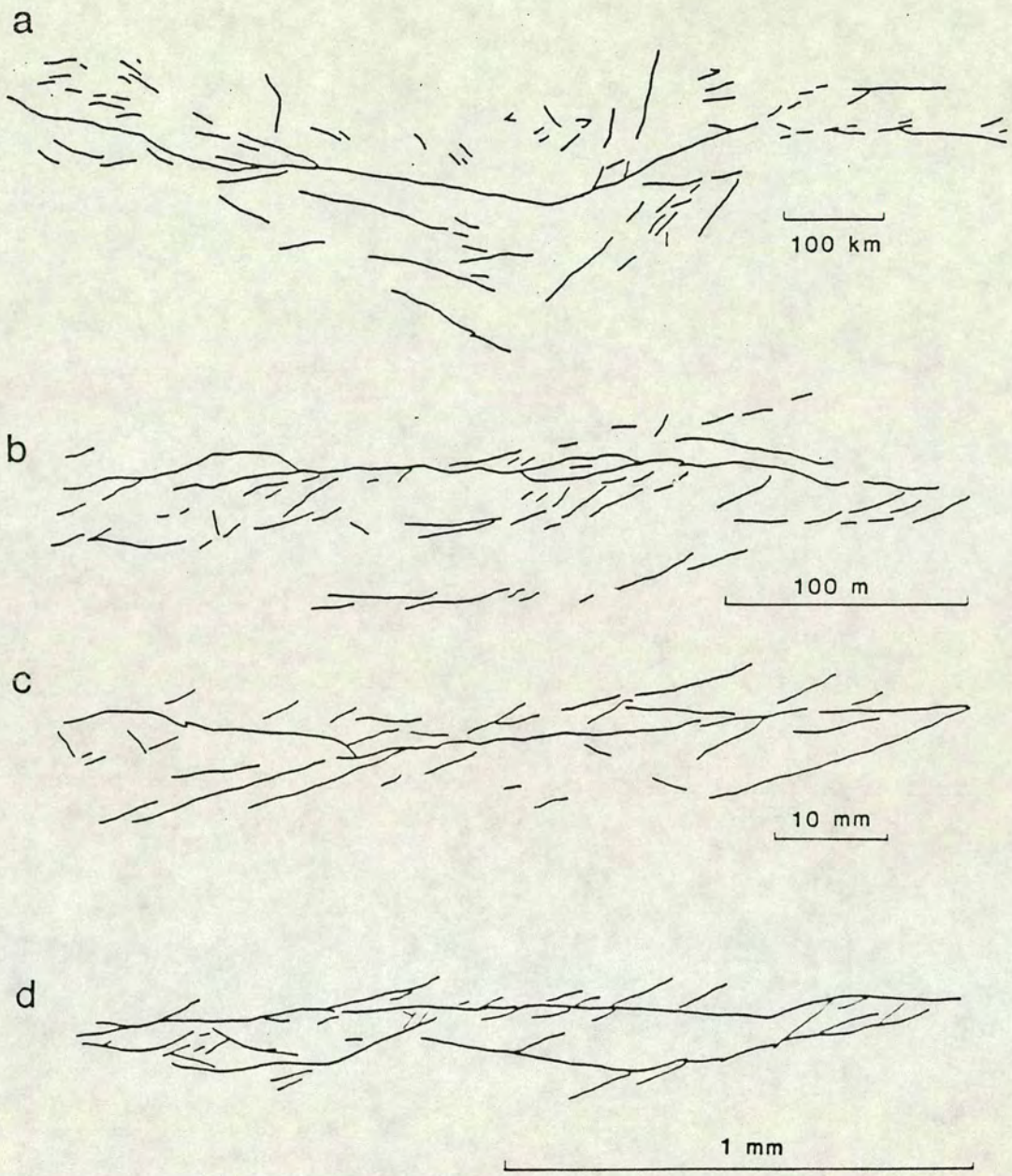

Figure 1.1 Scale invariance illustrated by the geometry of shear fault systems over a range of scales, from less than one millimeter to hundreds of kilometers (after Shaw and Gartner, 1986).

a. Faults active in California in the last 15 My. (Howard et al., 1978).

b. Dasht-e Bayez earthquake fault, Iran (Tchalenko, 1970).

c. Clay deformation in a Reidel shear experiment (Tchalenko, 1970).

d. Fractures produced in a shear box experiment (Tchalenko, 1970).

The concept of fractals

Mandelbrot (1982) first coined the term fractal to describe the geometric irregularities of self-similar objects, and described various methods of measuring different fractal dimensions, each of which measures a different aspect of the self-similarity. This definition of the fractal dimension of natural objects was first cast in terms of a Hausdorff-Besicovitch dimension, D_H, which must exceed the Euclidean or topological dimension, D_T, but need not be an integer. This narrow definition of a fractal set has now largely been replaced as a working concept by one which includes any set which has in some sense a scale-invariant geometry, and need not be strictly self-similar (Feder, 1988). For example, Feder (1988) quotes Mandelbrot as proposing a more general definition of a fractal as a shape made of parts similar to the whole in some way. Another extension of the concept considers that any natural geometrical set which exhibits a power-law relationship may be termed a fractal (Turcotte, 1989). This follows because the only distribution which is scale-invariant is a power-law. Consequently, many geological features, including fracture systems, that display scale invariance or a power-law size distribution may be analysed in this way. However, the use of fractal analysis in geology and geophysics is still relatively new, and so some confusion exists in the literature concerning the definition of the different fractal dimensions, and the methods of their measurement. It therefore seems necessary here to outline the various methods and types of fractal dimension available.

The classic example of a fractal system is that of the length of a coastline, which exhibits irregularities and increasing complexity at smaller and smaller scales, (Mandelbrot, 1982; Feder, 1988). For example the length of a coastline may be measured using a yardstick of length, r. As the length of the yardstick is decreased, it might be expected that the measured total length of the coastline would systematically

approach its 'true' length. In fact, the length L(r) of the coastline tends to increase without limit as the length of the yardstick, r, is decreased, so that:

$$L(r) \sim r^{1-D_H} \qquad (1.1)$$

where D_H is a Hausdorff-Besicovitch fractal dimension which must exceed the topological dimension D_T, (for reference, figure 1.2(a)i shows a line of $D_T = 1$). This in effect measures the roughness of a single coastline or feature, but may also incorporate spatial information from the distribution, for example a series of islands around the coast. This is the most widely accepted, and indeed the original, definition of a fractal dimension. The 'coastline' method has also been applied to several natural fracture systems, using the construction shown in figure 1.2(a)ii, which measures the total length of the fault in terms of small yardsticks of length r, or circles of radius r, containing the fault. For example, the trace of the San Andreas fault system in central and southern California, (Okubo and Aki, 1987), yields D_H in the range 1.2 to 1.43; whereas fault systems in Japan give $D_H = 1.05$ to 1.42 and in the Philippines $D_H =$ 0.85 to 0.95, (Matsumoto et al., 1992). The fractal dimensions quoted for faults in the Philippines are rather low, since D_H should exceed D_T, hence D_H should be greater than 1.0 for a linear trace of faults on a map. D_H may be less than 1.0 if the system consists of a series of points, suggesting that the fault system of the Philippines example may be more 'point-like' than linear.

The 'yardstick' method applies to rough one-dimensional features. However, if the geometry is essentially two-dimensional, the fractal dimension may be estimated using a box-counting method. For example, a map of a fracture system may be covered by a grid of boxes with side length r, and the number of boxes that contain a part or whole fracture are counted (Mandelbrot, 1982; Hirata, 1989). This method is illustrated in figure 1.2(b), where a map of joints is covered with a grid of initial side

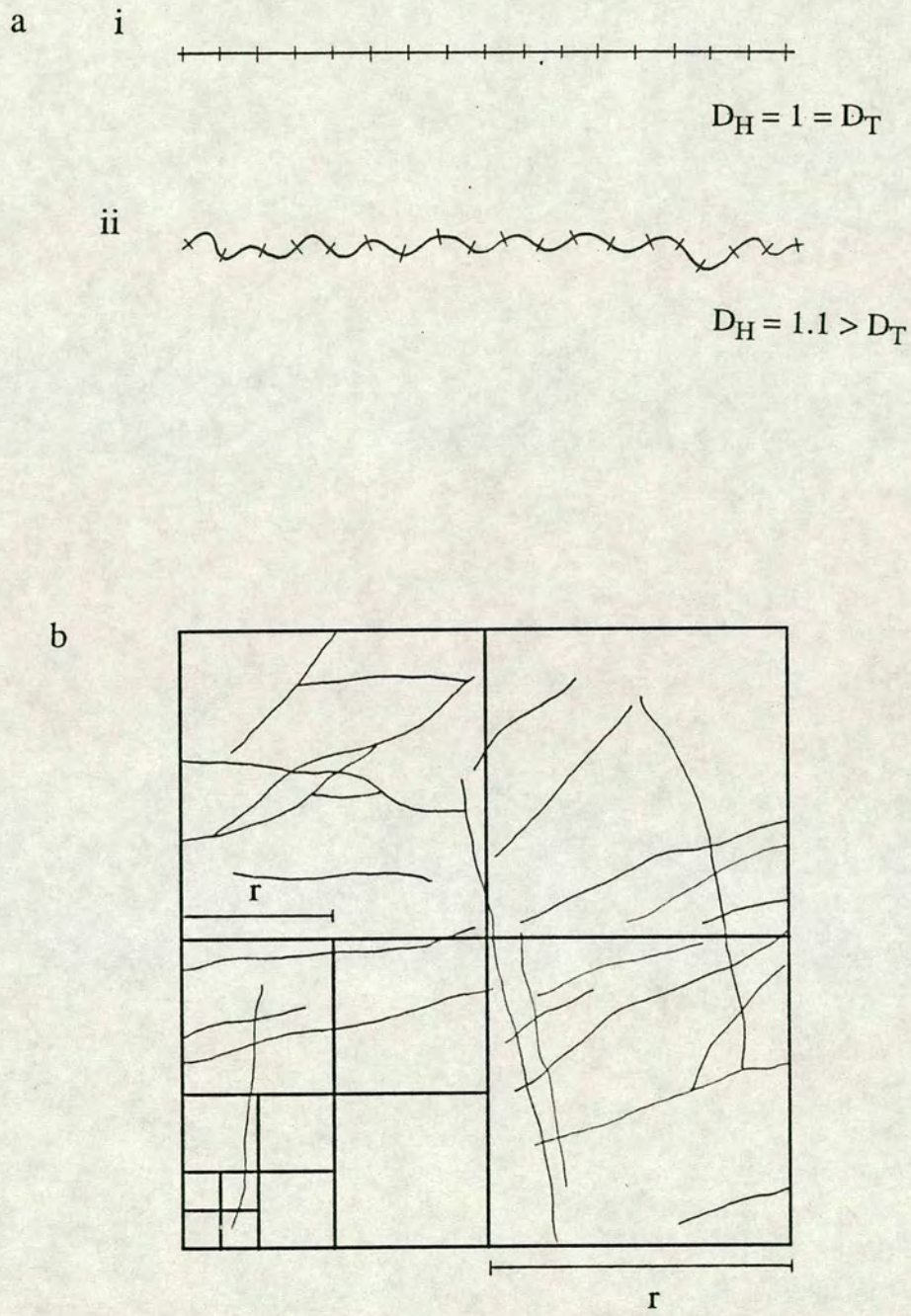

Figure 1.2 Illustration of the fractal concept.

a. A non-fractal one-dimensional line, with $D_H = D_T = 1$.

b. A rough (fractal) one-dimensional line, showing $D_H > D_T$.

c. Illustration of the box-counting technique.

length, r of 2.5 cm. A box counting (also known as capacity) dimension, D_{BC}, is then found from the power-law relation:

$$N(r) \sim r^{-D_{BC}} \qquad (1.2)$$

This is a more complete measure of the spatial aspect of a two-dimensional fracture system; in effect it measures how the system fills space. In a one-dimensional system, such as a straight single fault trace, $D_{BC} = 1$; in a two-dimensional system where the area is filled, $D_{BC} = 2$. For a single rough fault trace, D_{BC} is equivalent to the 'roughness' dimension D_H, and more generally D_{BC} represents the extension of a Hausdorff dimension to an array of elements. Box-counting has also been applied to natural fracture systems; for example, fault patterns in Japan which give values of D_{BC} from 0.71 to 1.6 (Hirata, 1989), and regional fracture networks in Africa where D_{BC} was found to range from 1.36 to 1.55 (Vignes-Alder et al., 1991). Again, a fractal dimension of less than 1.0 measured for a fault system in Japan (Hirata, 1989) appears to be too low, unless the fractures are 'point-like'. Artificial fracture systems produced by experimental simulation of crustal conditions have also been analysed by the box-counting or similar methods (Sornette et al., 1990; Davy et al., 1992), and reproduce the distributions found in nature reasonably well.

The next extension of the concept was to consider that any geometrical set which is scale-invariant and exhibits a power-law relationship may be termed a fractal (Turcotte, 1989). A quantitative definition of a fractal distribution as a working concept in geology and geophysics was given by Turcotte (1989) as follows: if the number of objects N with a characteristic dimension greater than L satisfies the relation:

$$N \sim L^{-D} \qquad (1.3)$$

then a fractal distribution is defined, where D is a generalised fractal dimension. It must be noted that this dimension measures the size distribution, and does not consider any spatial aspect of the system. Therefore, the fractal dimension D from this method is strictly a power law length distribution exponent, and is in general different from the Hausdorff-Besicovitch dimension D_H, including the box counting dimension D_{BC} for a two-dimensional fault array. Nevertheless, this method is very useful in examining natural systems of both fault structure and earthquake seismicity, as illustrated in the following geological examples. Figure 1.3(a) shows the length-frequency distribution of surface faults which have been active in the Holocene in the United States (after Shaw and Gartner, 1986). This discrete structural data plots as a straight line on the log-log axes, indicating a power-law relation similar to equation (1.3) with a fractal dimension D equal to the negative slope of the straight line (D = 1.76 for this example). Note that this value is greater than the Euclidean dimension of the one-dimensional fault traces on the map, as required in the definition of a fractal set. For linear faults on a map $D_T = 1$ and $1 < D_A < 2$, and for areal faults in a volume $D_T = 2$ and $2 < D_V < 3$, (Aki, 1981), where the subscripts A and V denote area and volume respectively. A consistant problem exists of relating two-dimensional fracture patterns to a three-dimensional volume, and must be considered especially if relating structural data from a two-dimensional outcrop to the seismicity emitted from a volume. This problem is further addressed in Chapters 3 and 4.

The fractal concept may also be applied to seismicity, as illustrated in figure 1.3(b). This shows the magnitude-frequency distribution of earthquakes in Southern California (after Main and Burton, 1986). In section 1.4, it is shown that earthquake magnitudes are measured on a logarithmic scale, and so this is also effectively a log-log plot, and hence the discrete seismological data also fits a straight line (power law) distribution on this plot. Thus earthquake seismicity is also fractal (Turcotte, 1989). The negative slope in this case is referred to as the seismic b-value. Aki (1981) was

Figure 1.3 Two naturally occuring examples of fractal systems, illustrating the scale invariance of the power-law distribution applied to structure and seismicity.
(a) Discrete length-frequency distribution of active surface faults in the United States (after Shaw and Gartner, 1986). This data gives a power-law distribution of fault lengths, with a fractal dimension of D = 1.76 from the negative slope of the best fit straight line.
(b) Discrete magnitude-frequency distribution of earthquakes in Southern California (after Main and Burton, 1986). This data also fits a straight line power law distribution, where the negative slope gives the seismic b-value.
The similarity of the plots from these two examples indicates that there may be a direct relationship between structure and seismicity.

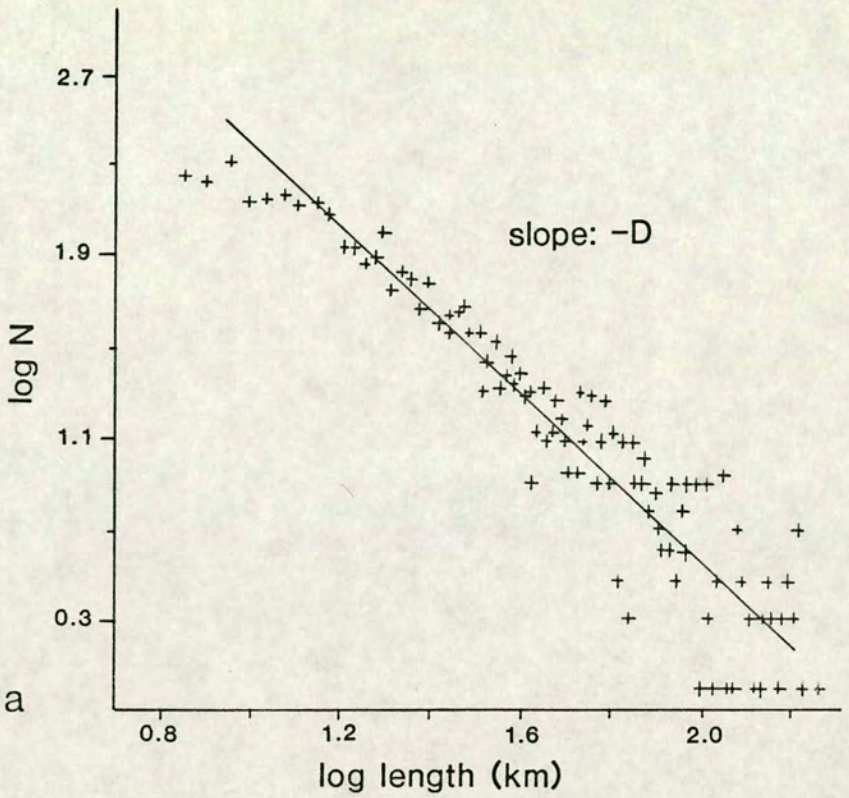
2.7
1.9
1.1
0.3
log N
slope: −D
a
0.8
1.2
1.6
2.0
log length (km)

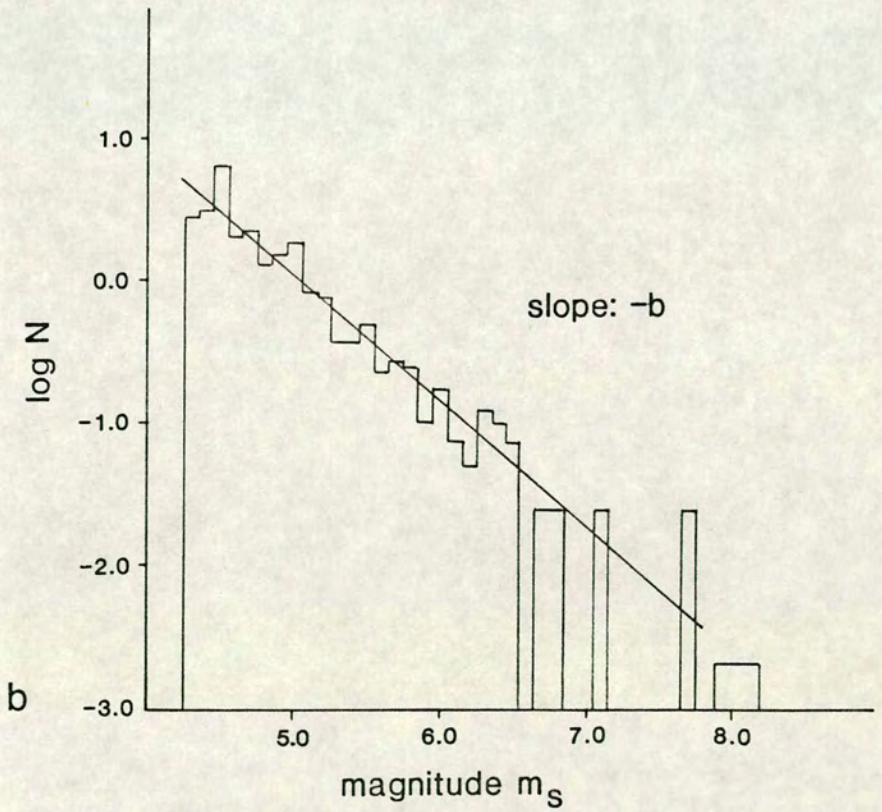
1.0
0.0
−1.0
−2.0
−3.0
log N
slope: −b
b
5.0
6.0
7.0
8.0
magnitude m_S

the first to show that the seismic b-value is proportional to the slope D on figure 1.3(a). This quantitative relationship is discussed in section 1.5, after a description of the dislocation model on which it is based.

In summary, this general definition of the fractal concept provides a direct means of quantifying both the structure of fracture systems and the related seismicity, and is the method used for the experimental and field data of this program. [In order to avoid confusion, in this thesis the power-law exponent of the length distribution will be referred to as D, and the Hausdorff-Besicovitch dimensions as D_H and D_{BC}. The two are equal only under special circumstances, for example if all the cracks radiate from a single point.]

Discussion

As discussed above, the concepts of scale invariance and fractals have proved extremely useful in recent attempts to quantify the nature of faulting and earthquakes. However, as well as the confusion over the many different fractal dimensions that may be measured, a controversy also exists over the nature of the scaling relationships in both fault structure and earthquake seismicity. Although it is generally accepted that earthquake distributions are scale invariant, and therefore fractal, it is not yet certain how much deformation may be attributed relatively to large and small earthquakes when summed over several earthquake cycles, (King and Cisternas, 1991). Similarly, recent fault population studies (Marret and Allmendinger, 1990, 1991; Scholz and Cowie, 1990; Walsh et al., 1991; Cowie and Scholz, 1992a, b) do not agree on the relationship between fault length and the slip or displacement on the fault, and consequently the scaling relation of the fault population. The relation between fault length and slip is a useful test of the scale invariance of the system. Two opposing models have been proposed. Both assume scale invariant single

increments of fault growth, but then differ in the way that the fault populations evolve. The fault growth model of Scholz and Cowie (1990) proposes scale invariant growth leading to a linear relation between length L and accumulated slip, u_a: $u_a \sim L$. Walsh and Watterson (1988), however, use a constant increment of growth in their model leading to: $u_a \sim L^2$, suggesting a non-fractal disribution. This has since been modified to $u_a \sim L^{1.5}$ (Marret and Allmendinger, 1990; Walsh et al., 1991). All of these models have been supported by observations of natural fault population data. However it is possible that this combined data set may simply be incomplete (King and Cisternas, 1991). Also, at least part of the problem is that the eventual observed fault pattern is the result of an integrated sequence of individual fault growth events and seismic or aseismic increments over a period of time. It seems necessary, therefore, to examine the scaling properties of fault or fracture systems and the associated seismicity for a single time increment. This is the main aim of this study. Unfortunately, the tensile microfractures produced in the laboratory specimens in this program were too small to show any significant measurable width distribution and so a comparable study of the length-width relation (using the inference that the width of a tension fracture is equivalent to the slip on a shear fault) was not possible. As mentioned in the above sub-section, a general definition of a fractal set and the microfracture length distributions alone were used to quantify the experimental structural data. However, the field data collected from natural tensile fracture populations in Iceland did include width measurements. These field results are discussed in Chapter 5.

1.3 Structure and mechanics of tensile fracture

When a stress is applied to a material, it may deform elastically at first up to a certain limit, and then either by plastic flow or brittle fracture. The mode of deformation after the elastic limit has been exceeded depends on the temperatures and pressures to which the material is subjected. Brittle fracture is mainly confined to the upper 10 - 15 km of the crust, with relatively low temperatures and pressures (0 - 40°C, 0 - 400 MPa). At higher temperatures and pressures, thermally activated plastic deformation gradually becomes the dominant mechanism. In this section, a basic background in both fracture mechanics and the structural geology of fracture is presented after a brief definition of elasticity and types of fracture. This will facilitate the integration of the mechanical, structural and seismological aspects of the project in the following chapters.

1.3.1 Elastic and non-elastic deformation

If a stress system (σ_1, σ_2, σ_3, where $\sigma_1 > \sigma_2 > \sigma_3$) is applied to a material, it will deform in one of several possible ways. If the material is truly linear-elastic, the resulting principal strains produced are by definition linearly related to the principal stress values, as in figure 1.4(a). If the stress is then released, the strains will return to their initial values. Most materials are quasi-linearly elastic for small strains, in the case of rocks less than 1% (Ramsay and Huber, 1987).

As the stress is increased, the elastic limit of the material is reached at a particular critical stress level, and the material then deforms in an irreversible way, by plastic flow if the temperatures and pressures are high enough, or by brittle failure and fracture. This study is concerned with the brittle field. If the stress regime is compressional, where $\sigma_1 > \sigma_2 > \sigma_3 > 0$, as illustrated in figure 1.4(b)i, then shear

Figure 1.4 Schematic diagram illustrating types of deformation.

(a) Linear elastic deformation by small strains (after Ramsay and Huber, 1987).

(b) i. Compressional stress system where $\sigma_1 > \sigma_2 > \sigma_3 > 0$, and σ_2 is normal to the plane of the diagram (after Anderson, 1951).

ii. Non-linear elastic deformation under compressional stress, illustrating the development of a Coulomb-Mohr shear fracture at an angle of 30° with the maximum principal stress σ_1 (after Paterson, 1978).

iii. Schematic diagram of a natural dip-slip normal fault, illustrating shear movement.

(c) i. Schematic diagram of a closed natural tensile fracture, illustrating pure dilational tensile movement due to the effects of a high pore fluid pressure, p.

ii. Schematic diagram of a natural tensile fracture, where the effective stress is tensile due to updoming.

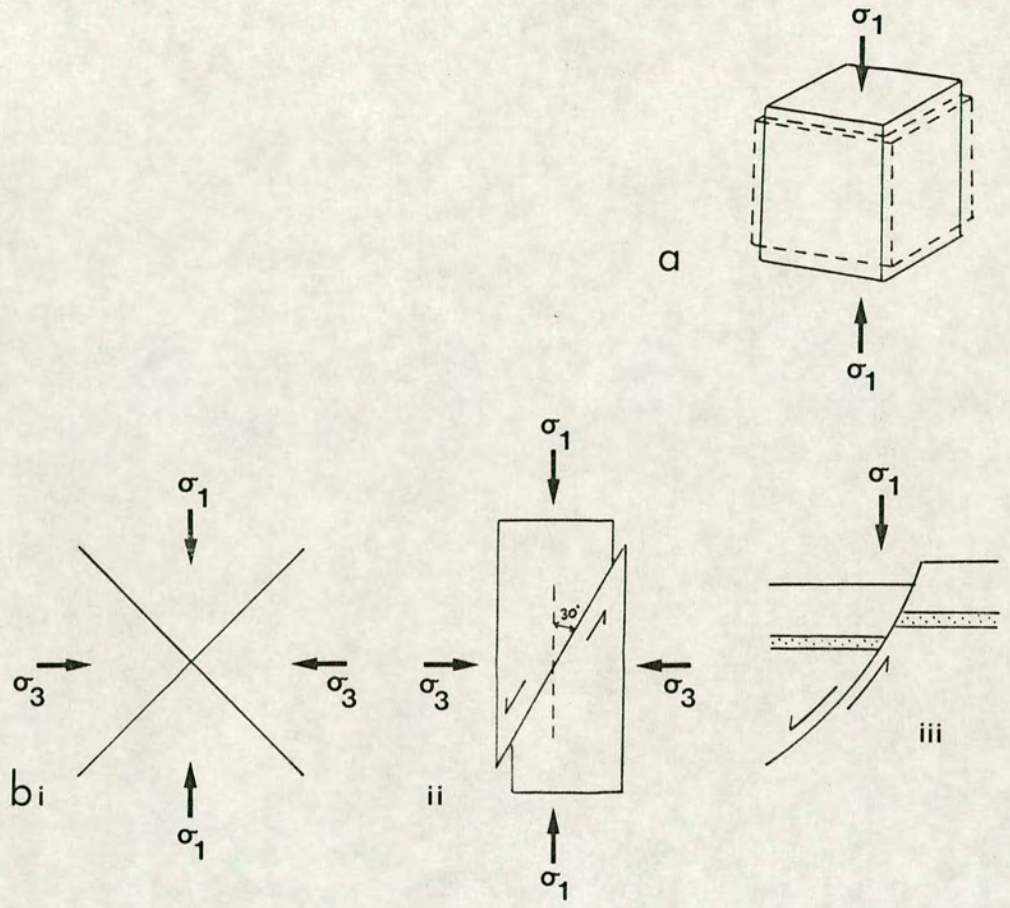
a
σ1
σ1
bi
σ1
σ3
σ3
σ1
ii
σ1
30°
σ3
σ3
σ1
iii
σ1

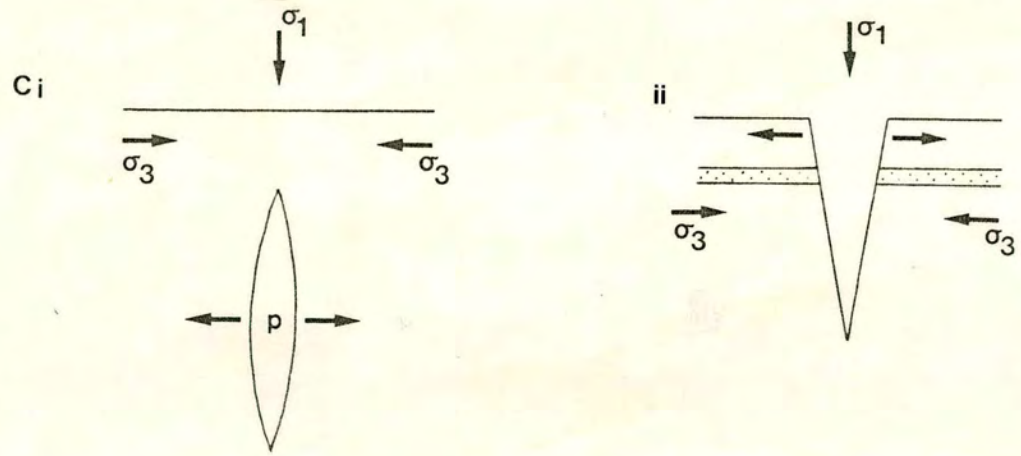
ci
σ1
σ3
σ3
p
ii
σ1
σ3
σ3

fractures will develop. In the laboratory, compressional tests on cylindrical specimens produce shear fractures typically at an angle of 30° to the maximum principal stress σ_1, figure 1.4(b)ii (Paterson, 1978). In the earth, if σ_1 is vertical, dip-slip normal faults are formed, figure 1.4(b)iii. By definition, a fault must involve some shear displacement of strata. In order to produce a tensile fracture that is purely dilational the effective minimum stress must be tensile. For this to occur, the principal stresses σ_1 and σ_2 must be small or near to zero, and σ_3 must be small compared to the tensile stress, in turn produced either from a high pore fluid pressure (p) or tensile bending stresses due to updoming, figure 1.4(c)i and ii. In the case of fluid injection the effective stress is $\sigma_e = \sigma_3 - p$. If $\sigma_e < 0$ the stress field is tensile. In the laboratory this is achieved by test and specimen design (see section 2.1). In the earth, pure tensile fractures occur due to such processes as upwelling of magma, followed by magma injection along tensile fractures, updoming and subsequent cooling. In this study, we are concerned with pure tensile fracture at low ambient surface temperature and pressure in the laboratory, and natural pure tensile fracture in the upper crust, (figure 1.4(c)).

1.3.2 Fracture mechanics and crack propagation in the laboratory

Fracture mechanics is primarily concerned with the criteria involved in fracture initiation and propagation within brittle materials. Several approaches to this discipline have been used since the initial studies by Griffith (1920) and Irwin (1958). Comprehensive texts exist that cover fracture mechanics in general, for example, Lawn and Wilshaw (1975); Jaeger and Cook (1979); and several that deal specifically with the fracture mechanics of rock, for example, Atkinson (1987), Meredith (1990). Here, a general background to fracture is given, followed by the concepts of fracture mechanics that are specifically relevant to this thesis.

Griffith was the first to recognise that all materials contain small cracks or flaws from which larger cracks may nucleate. His original consideration was for the energies involved in the propagation or closure of an ideal isolated elliptical crack in a stressed solid. In brief, for a static crack in an elastic-brittle solid, the total free energy U can be expressed as:

$$U = (-U_p + U_\varepsilon) + U_s = U_m + U_s \qquad (1.4)$$

where U_m is the total mechanical energy of the system ($-U_p$ is the potential energy of the applied load, and U_ε is the elastic strain energy stored in the solid), and U_s is the surface energy associated with the crack. For the system to be in equilibrium, the terms in equation (1.4) must be balanced with respect to any incremental change in the crack surface area A:

$$\frac{dU}{dA} = \frac{dU_m}{dA} + \frac{dU_s}{dA} = -G_M + G_R = 0 \qquad (1.5)$$

where G_M is the mechanical energy release rate and G_R is the energy rate resistance (Irwin, 1958). In an ideally brittle solid, $G_R = 2\gamma$ (where γ is the surface free energy), since two new surfaces must be created for the crack to propagate.

As an alternative approach, Lawn and Wilshaw (1975) defined a crack extension force or strain energy release rate (G) for a two-dimensional system as:

$$G = -\left(\frac{dU_\varepsilon}{da}\right) \qquad (1.6)$$

where a is half the crack length in a two-dimensional system. This definition ignores the mechanical energy held in the loading system. Failure occurs when G reaches a critical value, $G_C = 2\gamma$, when the energy supply equals or exceeds the energy demand.

An equivalent approach in producing a fracture mechanics parameter is to examine the stress concentration at the crack tip resulting from the crack extension force. This is directly applicable to this study, and so is examined in some detail in the following sub-sections, after a brief description of the modes of fracture encountered in fracture mechanics. Examples from field studies are presented separately in the next section.

Crack tip displacement modes

There are three basic modes of crack tip displacement (Lawn and Wilshaw, 1975), as illustrated in figure 1.5; mode I (tensile or opening mode), where the crack walls open due to tensile stresses; mode II (in-plane shear or sliding mode), where the crack walls shear in a direction normal to the crack front; and mode III (anti-plane shear or tearing mode), where the crack walls shear parallel to the crack front. In this study, we are concerned with mode I tensile displacement.

Stress concentration and stress intensity

The importance of stress concentration due to pre-existing flaws in a material under stress was first introduced by Inglis in the early 20th century. It was recognised that an elliptical hole or sharp re-entrant in a material could cause the local stress to increase to a level much greater than that of the applied stress. Figure 1.6 illustrates this in two contour maps of the stresses around a sharp crack, (Gordon, 1976).

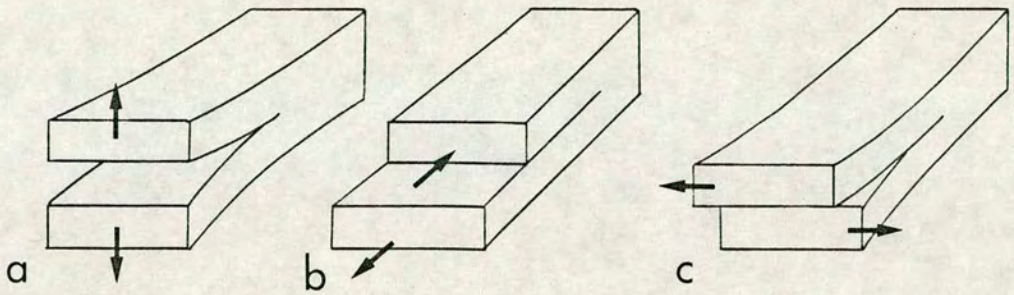

Figure 1.5 The three basic modes of crack tip displacement (after Lawn and Wilshaw, 1975).

(a) Mode I (tensile or opening mode).

(b) Mode II (in-plane shear or sliding mode).

(c) Mode III (anti-plane shear or tearing mode).

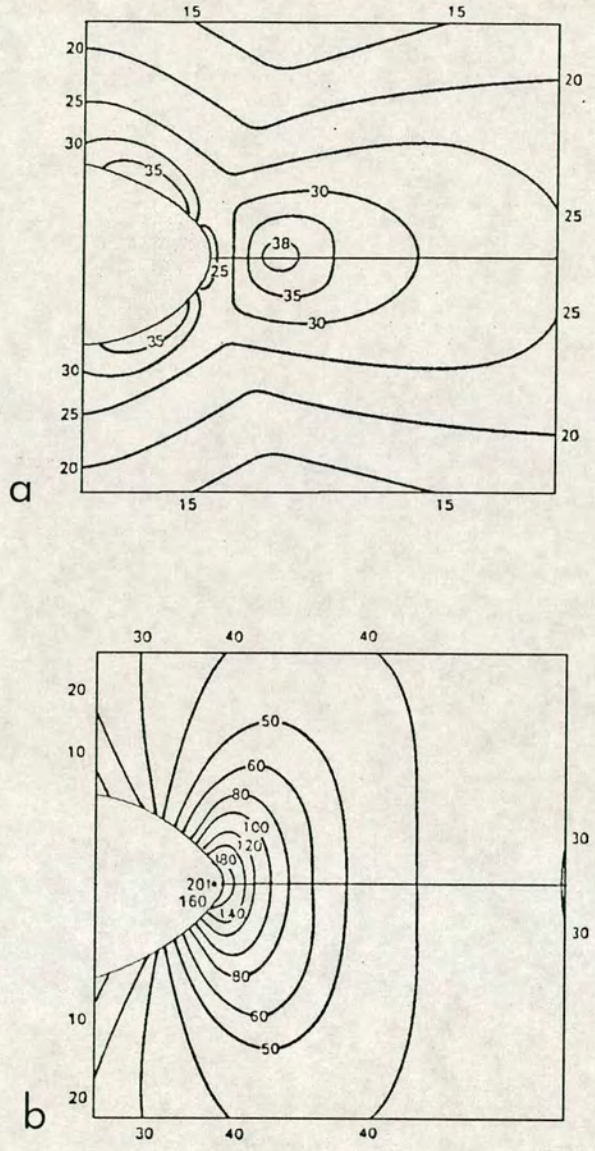

Figure 1.6(a) Contoured stress system at the tip of an elliptical crack. The contours are lines of equal stress, and are shown normal to the applied load. This illustrates the increased local stresses due to stress concentration at the crack tip (Gordon, 1976). (b) Contoured stress system parallel to the applied load, at the tip of an elliptical crack (Gordon, 1976).

Therefore, the degree of stress concentration at the crack tip is of greater importance in determining whether the crack will propagate or remain stable, than the overall applied stress. The stress intensity factor K is a measure of the magnitude of the stress concentration at the crack tip, and is the fracture mechanics parameter of most use in this study. In general, the stress intensity of the local tensile (mode I) stress field for an infinitely sharp elastic crack may be given as:

$$K_I = \sigma (\alpha \pi a)^{1/2} \qquad (1.7)$$

where σ is the remotely applied stress, α is a dimensionless parameter depending on the specimen and crack geometry, and a is half the crack length (Irwin, 1958; Lawn and Wilshaw, 1975; Anderson and Grew, 1977). This formulation has been applied to specific experimental specimen and loading geometries, such as the double torsion specimen used in the present work (Williams and Evans, 1973). A description of the specific stress intensity analysis and the formula for calculation of K_I for the experimental specimen used in this study is given in Chapter 2.

The Griffith energy balance concept can be related to the idea of a stress concentration directly, since the stress intensity factor is proportional to the strain energy release rate:

$$G_I = \frac{K_I^2(1-\nu^2)}{E} \qquad (1.8)$$

where ν is Poisson's ratio, and E is Young's modulus (Atkinson, 1987).

Subcritical crack growth and stress corrosion

An important concept in linear elastic fracture mechanics is that a crack will propagate dynamically and unstably once a critical stress intensity factor K_C, or energy release rate G_C, has been reached or exceeded. The velocity of propagation under these critical conditions is limited by inertia to that of sound in the material, of the order 10^3 ms^{-1}, and so this is known as dynamic (or catastrophic) fracture. However, it is also found in many materials that significant fracture may occur at values of K far below the critical value, at velocities of less than 10^{-1} ms^{-1}. This phenomenon was not predicted by Griffith, and is known as subcritical or quasi-static crack growth. Such subcritical crack growth has been shown to be highly sensitive to environmental conditions such as temperature and chemistry (Anderson and Grew, 1977). Slow stable subcritical crack growth may eventually become unstable as the crack length (and hence K_I or G_I) increases whereupon the material may fail dynamically.

Several mechanisms have been suggested for the process of subcritical crack growth, including stress corrosion, mineral dissolution, ion exchange and microplasticity. Extensive reviews of these mechanisms are given by Atkinson (1982, 1984) and Atkinson and Meredith (1987a) who concluded that stress corrosion is the most likely mechanism of subcritical crack growth in the upper 20 km of the crust.

Stress corrosion occurs by the weakening of the strained bonds at the crack tip by an active environmental agent, thought to be dominantly H_2O in the case of silicates (Scholz, 1968a). Originally, stress corrosion was studied in metals, glasses and ceramics due to the frequent observations that these materials failed under lower stresses than those predicted from strength measurements, especially in the presence of water (Anderson and Grew, 1977). This time-dependent phenomenon is often

known in the materials science literature as static fatigue. In silicate glasses and quartz, it is the strained Si-O bonds at the crack tip that react more readily with the environmental agent than the bonds elsewhere in the material due to a strain produced reduction in the overlap of atomic orbitals (Michalske and Frieman, 1982; Atkinson and Meredith, 1987a). Chemical expressions for such weakening in silicate glasses and quartz in water have been proposed, usually involving the hydrolysis of strong Si-O bonds to weaker Si-OH·HO-Si bonds (Atkinson and Meredith, 1987a). However, silicate rocks that contain more complex silicate minerals, such as feldspar, mica, pyroxene and amphibole represent a more complicated system, which has not been studied fully as yet. The microstructure of polycrystalline rock also influences subcritical crack growth (Atkinson, 1982; Scholz, 1968a, 1968b), since inhomogeneity affects the local stress fields and the local fracture toughness (resistance to cracking), varying the nature of the material the crack encounters as it propagates.

The most usual equation used to describe subcritical crack growth by stress corrosion is Charles' equation (1958) which relates the rupture velocity, V to the stress intensity factor, K:

$$V = V_o K^n \exp\left(\frac{-H}{RT}\right) \qquad (1.9)$$

where V_o is a constant, H is the activation energy of the process, R is the gas constant, T is absolute temperature and n is the subcritical crack growth index (also known as the stress corrosion index when this mechanism is appropriate). There is some question whether this relationship is of exponential or power law form. However, this ambiguity is only significant at velocities and stress intensities well below the present experimental capabilities. The exponent may also be absorbed into

a constant for a given rock type and active fluid to produce a simpler formula as follows:

$$V = V_0 \left(\frac{K}{K_0} \right)^n \qquad (1.10)$$

where V_0 and K_0 are scaling constants which include the effect of temperature and activation energy. Figure 1.7(a) shows a schematic diagram of velocity as a function of stress intensity for mode I crack propagation, from tensile experiments on oxides, glass, ceramics, and silicates (Evans, 1972; Anderson and Grew, 1977; Atkinson, 1982, 1984). There are three distinct regions between the threshold stress intensity K_0 and the critical stress intensity K_{IC}. K_0 is the minimum stress intensity below which there is no discernable crack growth; K_{IC} may also be referred to as the fracture toughness. A minimum stress intensity has not been observed in experiments so far, due to difficulties in reducing the strain rate to a minimum. In region 1, the velocity is thought to be controlled by stress corrosion reactions; in region 2, at higher K_I, the rate of transport of reactive species to the crack tip is thought to be the rate limiting step; in region 3, the velocity is thought to be controlled by almost purely mechanic rupture, a process that is much less sensitive to the chemical environment. Figure 1.7(a) also illustrates the effect of an increase in stress corrosion crack velocity due to temperature or an increase in partial pressure of H_2O and the resulting concentration of water presence in the environment. Experimental data illustrating all three regions have been produced, for example in polycrystalline alumina (Evans, 1972). However, in tests on rock, the data usually do not show region 2 behaviour (Atkinson, 1984). Figure 1.7(b) shows a synoptic diagram illustrating the range of variation in tensile subcritical crack growth results from different rock types (Atkinson, 1984).

Figure 1.7(a) Schematic diagram of crack rupture velocity versus stress intensity factor (log-log) for subcritical mode I tensile crack growth due to stress corrosion. K_o is the stress corrosion limit, K_{IC} is the critical stress intensity factor or fracture toughness. The influence of increasing temperature, partial pressure, water concentration is to increase the velocity at a given K_I (Meredith, 1990).
(b) Schematic diagram illustrating the range of variation in tensile subcritical crack growth results from different rock types. The slope of the solid line is the subcritical crack growth index, n (Atkinson, 1984).

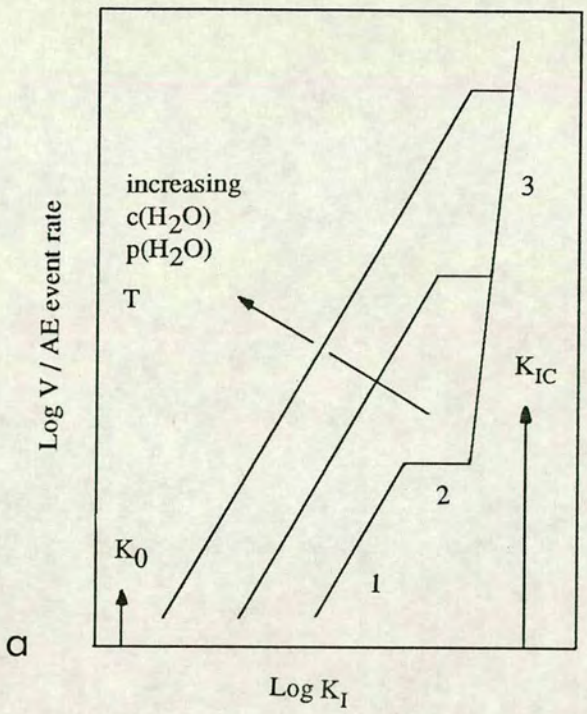
Log V / AE event rate
increasing
c(H2O)
p(H2O)
T
3
KIC
2
K0
1
a
Log KI

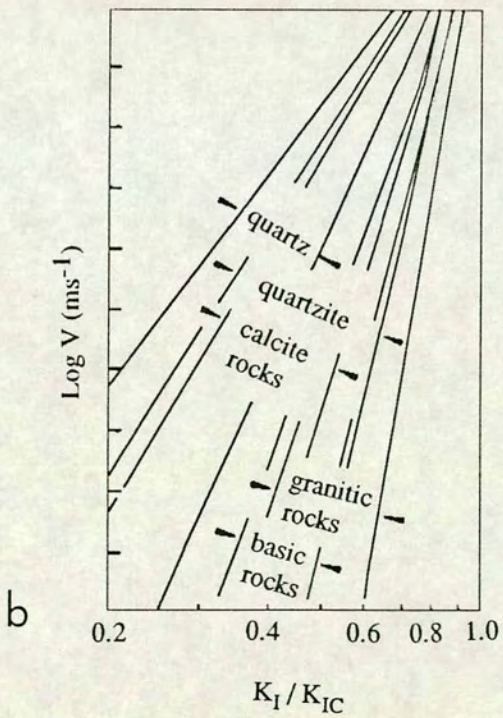
Log V (ms-1)
quartz
quartzite
calcite
rocks
granitic
rocks
basic
rocks
b
0.2
0.4
0.6
0.8
1.0
KI / KIC

Variations in the mineralogical composition of the rocks result in differences in the subcritical crack growth index.

Subcritical crack growth by the mechanism of stress corrosion can also be investigated as a structural process by direct observation of the crack surfaces produced in experimental specimens. In previous experimental work (for example, Meredith and Atkinson, 1983), fractures produced by dynamic crack growth at high velocities and low environmental fluid content tend to be relatively straight and transgranular, figure 1.8(a), whereas slower fracture with an active fluid present tends to produce rougher grain boundary microcracking, figure 1.8(b), on the scale of conventional Scanning Electron Microscope imaging. Thus, subcritical or quasi-static crack growth exploits pre-existing weaknesses such as grain boundaries, whereas dynamic crack growth produces straighter fractures because of the effects of inertia and stress concentrations.

In summary, the importance of stress corrosion and the presence of an active environmental agent has previously been demonstrated experimentally (Meredith and Atkinson, 1983; Main et al., 1990). One of the objectives of the present work is to confirm these results by experiment, where tensile tests were run both in air of ambient humidity (hereafter referred to as 'dry' tests), and by totally immersing the specimens in a water bath (to be referred to as 'wet' tests). The differences are, therefore, primarily due to the activation of the stress corrosion mechanism, and these differences will be quantified by seismic and structural analysis of the specimen.

Natural subcritical crack growth due to stress corrosion is also thought to be significant in time-dependant failure in the earth, and has been applied to the prediction of earthquake recurrence times and the statistics of foreshock sequences (Scholz, 1968b; Anderson and Grew, 1977; Das and Scholz, 1981; Main, 1988).

Figure 1.8 Electron micrographs of the fracture surfaces of two Whin Sill dolerite specimens (after Meredith and Atkinson, 1983).

(a) Dynamic fracture at high crack velocity (>10ms^{-1}) carried out in dry air at ambient pressure and 20°C tends to be smooth and transgranular.

(b) Subcritical crack growth at low velocity (c. 10^{-7}ms^{-1}) in water at ambient pressure and 20°C produces rougher grain boundary microcracking.

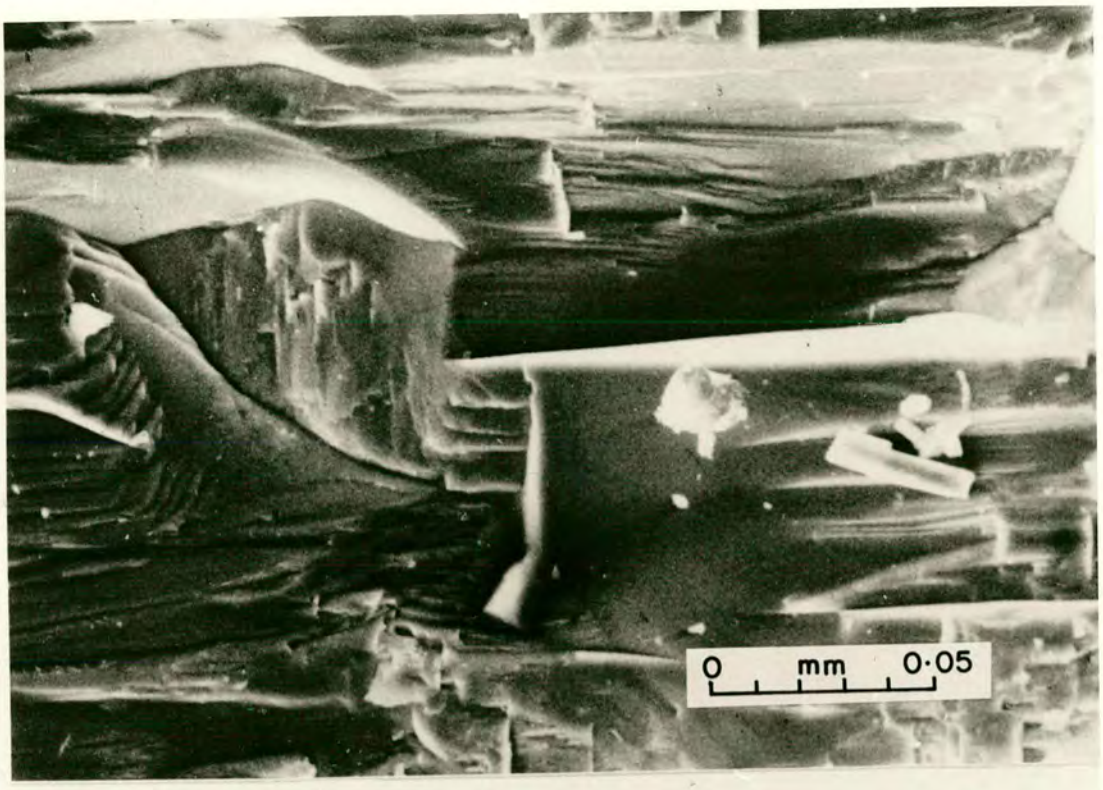

a

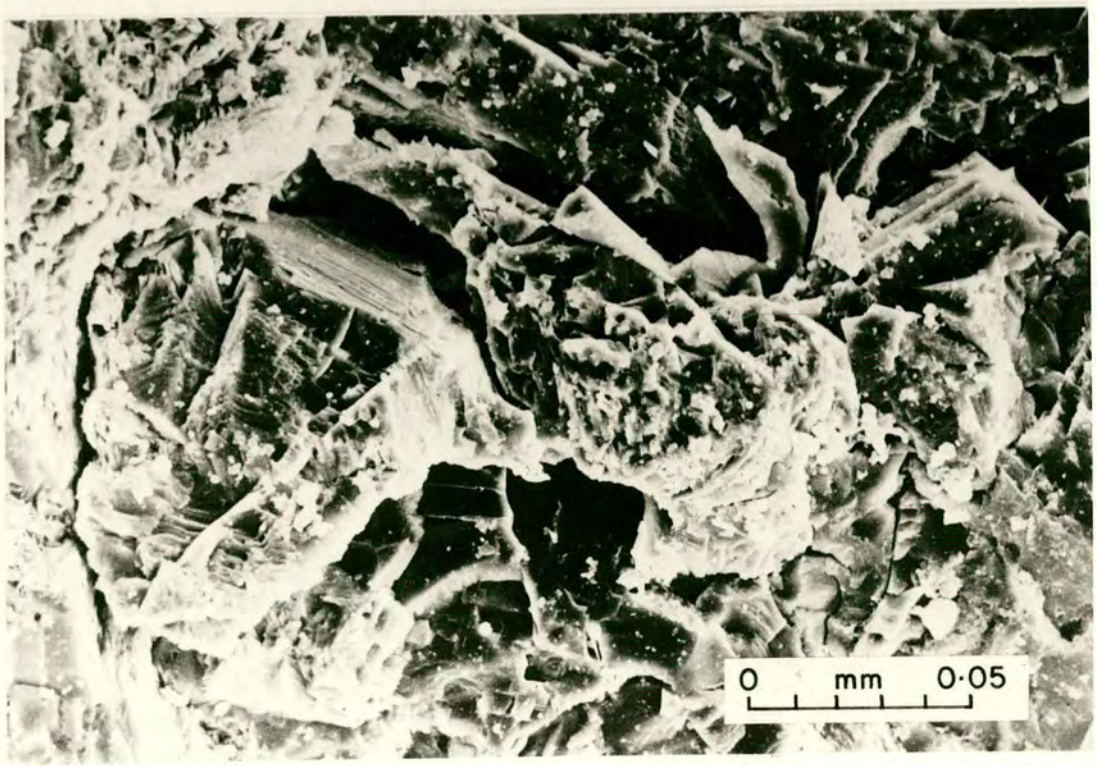

b

Several structural investigations of natural fracture systems have recently referred to stress corrosion in rock as a significant mechanism. For example, evidence of stress corrosion in silicate rocks has been found by examination of mineral reactions (Kerrich et al., 1981). Subcritical crack growth has also been suggested as the mechanism of joint formation in granitic rocks of the Sierra Nevada (Segall and Pollard, 1983).

Non linear elastic fracture: the process zone

The fracture of composite heterogeneous rock is thought to be more complex than the simple idea of an ideal single, sharp flaw assumed in linear elastic fracture mechanics. For example, it has been suggested (Atkinson, 1987) that a zone of inelastic microcracking develops in an aureole ahead of the main macrocrack due to the stress concentration there. As the stress increases, these microcracks first become more intense and aligned, and eventually the macrocrack propagates by coalescence of the convenient microcracks in its path ahead of the previous crack tip. The zone of advance microcracking is termed the 'process zone', and migrates ahead of the propagating macrocrack. Direct evidence of such a simple process zone has not been observed. Swanson (1987) proposed a lobe-shaped process zone. However, he could not find direct evidence of such a process zone in his tensile experiments on granite. These models have since been replaced by a more complex thin-zone model of a fracture process zone, (for example, Ingraffea, 1987; Meredith, 1990), as illustrated in figure 1.9. Here, the 'effective' crack length consists of a true traction free crack and a process zone of interface tractions behind the macrocrack tip and microcracking ahead the crack tip. Strain-softening behaviour localises the inelastic tractions and microcracking to a thin zone. This model takes into account the rough nature of actual fractures. Indirect experimental evidence for such a 'process zone' includes strain-softening behaviour in tensile tests (Labuz et al., 1985), observations of narrow zones

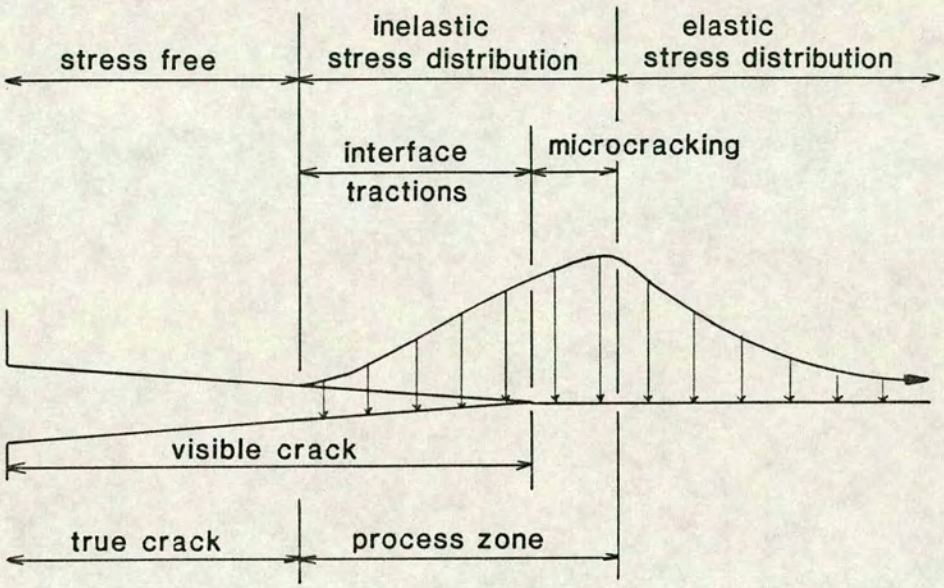

Figure 1.9 Schematic diagram of the stress distribution at the tip of a hypothesised crack comprising a true crack and a process zone (Ingraffea, 1987; Meredith 1990).

of short subsidiary microcracking associated with macrocracks at all scales (Main et al., 1990), and in-situ observation of interface traction mechanisms accompanying a propagating macrocrack (Freiman and Swanson, 1990). Cox and Scholz (1988) have argued that the 'process zone' may be significant in shear fracture, and is found to be much larger for rocks than other materials. The term 'zone of damage' may be more appropriate. Damage zones may also be seen at a larger scale, in the field, for example areas of intense jointing ahead of a propagating dyke intrusion (Delaney et al., 1986; Mastin and Pollard, 1988).

These mechanisms must be considered when designing test specimens and analysing experimental data. The approach of linear elastic fracture mechanics assumes that such a zone of inelastic behaviour is small relative to the length of the crack and the size of the test specimen.

Crack stopping

Finally, a process that significantly affects the choice of material in experimental testing is that of crack stopping, specifically by an interface that is approximately at right angles to the direction of crack propagation. If the adhesive strength of the interface is less than the general cohesive strength of the material, then the oblique interface will effectively act as a crack stopper (Gordon, 1976). In effect, the crack is diverted along the newly encountered weakness. This is important in determining appropriate experimental specimens in the present work as we require a crack to propagate under uniform conditions roughly along the centre of the specimen, and so inherent weaknesses at high angles to the specimen length are undesirable. For this reason, strongly anisotropic metamorphic materials were not investigated in the present study, though the solution of this problem might form an interesting technical challenge in future work.

1.3.3 Natural tensile fracture in the earth

Brittle tensile fracture is evident at many scales in the earth, from microcracks of micron scale to plate boundary tension fractures at mid-ocean ridges. In this study, we are mainly concerned with the generation of artificial microfractures produced in the laboratory as an analogy to pure tensile fracture in the field. In this section, I will define and describe the types of microfractures found naturally in rock, briefly describe veins and joints as an intermediate scale of tensile fracture, and finally describe some situations where large scale extension can occur. Throughout this study, the terms crack and fracture are used synonymously, since there is no significant shear displacement in any of the features under study.

Microfracture

Microcracks occur naturally in most rock types as a result of natural stresses or changes in temperature. Two comprehensive reviews of microcracks in rocks are given by Simmons and Richter (1976) and Kranz (1983) and so I shall present here only a summary of the most relevant points. Several microcrack types may be distinguished.

1. Grain boundary cracks are associated with a grain boundary and may be either non-coincident with the crystal boundary and extend for short distances into the grain, or coincident as indicated by a separation between the crystal boundary and the adjacent material. Microcracks often exploit the weakness between crystals in their growth, and may extend continuously along the boundaries of several grains.

2. Intragranular cracks occur within a single grain without reaching the grain boundary, and are usually small and mode I extensional, involving no shear deformation.

3. Intergranular cracks run across a single grain from grain boundary to grain boundary, and may extend into the adjacent grains.

4. Transgranular cracks cross several grains and may be deflected by grain boundaries, usually taking the path of most convenient weakness.

It is often difficult in practice to classify an observed crack into one of these categories. A crack may appear to be several intragranular cracks, due to the orientation of the thin section viewed, when in fact it is a single intergranular crack. Transgranular cracks often run along the grain boundary for at least part of their length.

Several differences in crack morphology are also evident between naturally formed microcracks and those produced artificially in the laboratory. Natural cracks will often form in a changing stress regime and may be closed relatively quickly after formation. Fluids in natural rocks will also have time to deposit material to infill the cracks, and the cracks will become sealed. In the laboratory, the stress field is usually constant, and so the microcracks become sharp with defined walls and an orientation related to a single minimum stress direction. Also, even in the presence of fluids, at the low temperatures and pressures used in this study, the laboratory time scales are not sufficient to allow significant healing or infill of the fractures.

Veins and joints

The term mesoscale may be used to describe intermediate scale structures that range from less than a centimeter to a few meters in size (Turner and Weiss, 1963; Hancock, 1985). Tensile mesofractures in the form of veins and joints are often abundant in field exposure.

Veins are mesofractures that have been infilled with mineral material (by definition, at least 1 mm in width). Veins can be important kinematic indicators, for example where the growth of the fibres within the vein records the directional history of the active strain at the time of formation (Hancock, 1985). Pure extensional veins show undeformed fibres perpendicular to the vein margin. If a shear movement is also involved, the fibres will reflect this by growth oblique to the vein margin. Mineral veins are also important evidence of the subsurface movement of hydrothermal fluids, and so outline the importance of examining tensile fracture and fluid-rock interactions.

Joints may be defined as barren, closed fractures along which no appreciable displacement has occurred (Hancock, 1985; Ramsey and Huber, 1987). Joints may also be classified as either extension or shear, or a hybrid of both. Although there are several criteria that may be used as evidence, such as surface markers and kinematic indicators (Hancock, 1985), it is often difficult to distinguish between the types. Joints generally occur in parallel or sub-parallel sets, and often several sets at different orientations will form a joint system. However, although joints can be successfully used for regional tectonic stress analyses (Wise, 1984; Segall and Pollard, 1983; Hancock, 1985; Delaney et al., 1986; Engelder, 1987; Mastin and Pollard, 1988), joints are not a suitable analogy to the pure tensile microfractures produced in the laboratory specimens to be decribed in this work, since jointing is

often a multiphase process, and the common variations in orientation in joint systems present complications in comparison with the controlled laboratory experiments.

Large scale tensile fracture and extension

There are two general types of large scale extension in the earth's crust. The first type is pure tensile fracture, resulting from tensile tectonic plate movements, producing large scale lineaments (Nur, 1982) or tensile rifting zones primarily at divergent spreading margins, for example Iceland. Extension may also occur in intra-plate regions where the overall principle stresses are primarily compressive, and where most of the deformation is taken up by normal faults.

In an extensional province the maximum principal stress, σ_1, is vertical and displacement on the fault plane produces a downthrown hangingwall. However, these shear displacements at depth rule out any classification of normal faults as 'tensile' fractures (see figure 1.4(b)), though it is common for the surface expression of normal faults to involve a component of tensile fracture, both in the footwall and the hanging wall (Ramsey and Huber, 1987).

In contrast, igneous dykes may also be considered a type of large scale extension involving tensile failure. There are two possible methods of dyke formation; (1) a pre-existing fracture in the earth's crust is utilised as a weakness and infilled by rising magma, or (2) the pressure, p, of the uprising magma exceeds the minimum principal stress σ_3, thereby exerting a negative horizontal effective stress, $\sigma_e = \sigma_3 - p < 0$, on the rocks above, thus creating hydraulic tensile fractures for the magma to infill. Natural dyke formation probably involves both these processes. A shear, as well as opening, movement may also occur as the dyke is infilled in the case where σ_1 and σ_2 are not zero.

The most useful direct analogy to the experimental tensile fracture patterns in the laboratory specimens is natural pure tensile fracture, where the principal stress is tensile (σ_1, σ_2 , σ_3) = (0, 0, -T). Tension fractures involve a direct opening, often vertical to subvertical, with no shear displacement, (figure 1.4(c)ii). A natural pure tension fracture usually has a limited critical length (depth of penetration) before further extension will induce downthrow of one side of the fault. This occurs since σ_1, σ_2 and σ_3 all increase with depth. The fracture then becomes a normal fault (Opheim and Gudmundsson, 1989). Previous work in the extensional fissure zones of Iceland, representing the onland divergent plate boundary (Mid-Atlantic Ridge), has shown that the length distributions of tectonic tension fractures may be approximated by a power law, figure 1.10 (Gudmundsson, 1987). Since the majority of fractures in these regions are pure tension fractures, Iceland was chosen as the most suitable area in which to conduct the field work element of this study.

1.4 Seismology

Earthquakes are perhaps the most dramatic way of releasing the build up of tectonic stresses in the earth. The surfaces of natural flaws are observed to show irregularities, termed asperities, that impede slip between the surfaces. High stresses build up at these asperities, leading at first to quasi-static slip at these points, until slip at the asperity reaches a critical value d_C. Once slip reaches d_C the asperity is fractured, resulting in a sudden reduction in the stress and nucleation of an earthquake due to the stress concentration at the fracture tip. Rupture governed by the friction of the surfaces then proceeds along new or pre-existing flaws in the crust. Figure 1.11 illustrates this mechanism, described as a slip-weakening model since stress decreases with increasing slip (Scholz, 1990). The shaded area in figure 1.11 may be shown to be equal to the critical strain energy release rate, G_C.

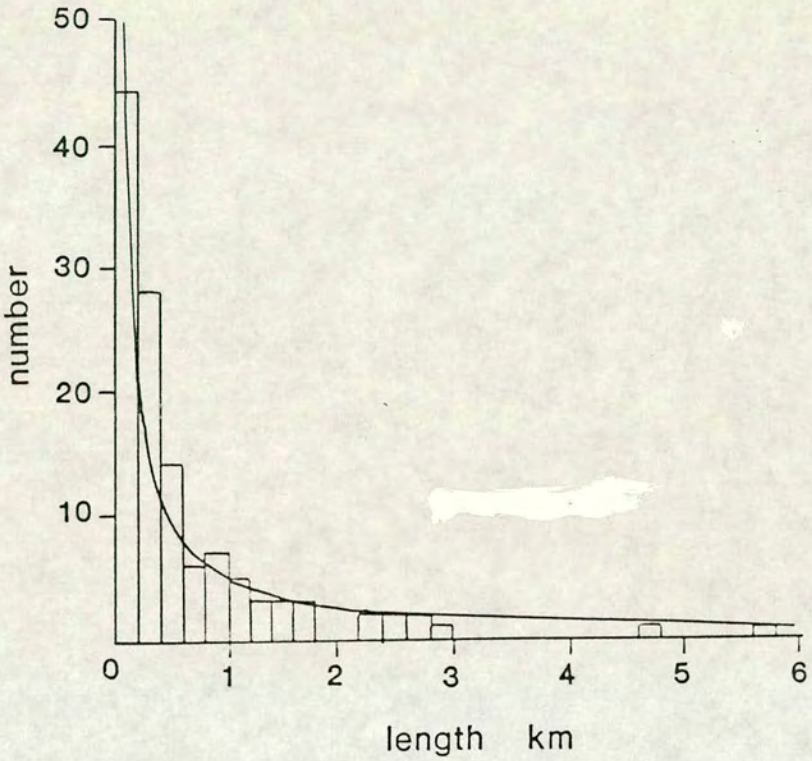

Figure 1.10 Length distribution of tectonic fractures within the Vogar fissure swarm of south east Iceland, illustrating the power-law distribution (Gudmundsson, 1987).

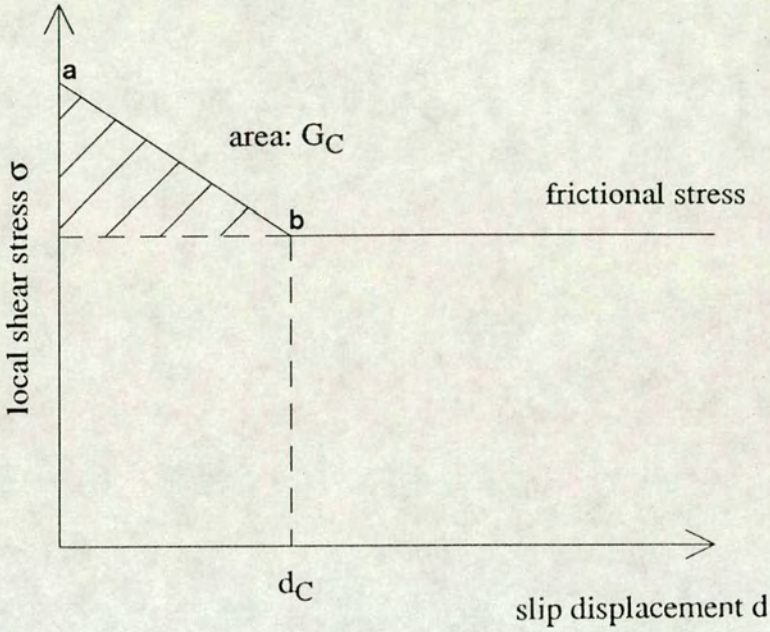

Figure 1.11 Slip-weakening model. At (a) an asperity resists slip producing a high stress build up. At (b) the asperity has been broken, and the stress is reduced to a frictional constant. G_C is the critical strain energy release rate, d_C is the critical slip distance at the point of the asperity.

Many studies into earthquake mechanisms or earthquake prediction use natural earthquake data from presently active regions. However, rock mechanics studies in the laboratory have also previously been used to examine seismicity and rock deformation in a controlled environment. For example, Scholz et al. (1973) used laboratory data to support the dilatancy-diffusion model of earthquake prediction. Meredith et al. (1990) produced a model of earthquake precursors based on temporal fluctuations in seismic b-values, from both natural and laboratory data. In both of these studies, precursors to dynamic failure were determined by monitoring the acoustic emissions during crack growth in laboratory experiments as a small scale analogy to earthquake waves, and seismological techniques were used to quantify this laboratory data and scale the results to the field case.

In this study we are primarily concerned with a seismic source quantified by the acoustic energy radiated during dynamic increments of crack growth. (Even in subcritical crack growth, where the large scale rheology is quasi-static, individual elements of growth occur by small dynamic increments which produce acoustic waves). In the following sections, I will describe the standard techniques available to quantify earthquake size, a dislocation model that is used to interpret the scaling properties of earthquakes of different magnitude, some general concepts related to earthquake 'size', and finally an introduction to acoustic emission.

1.4.1 Earthquake magnitude

The earthquake magnitude (m) is the most commonly used measure of the size of an earthquake. The magnitude of a local earthquake, m_L, was defined by Richter (1958) as the logarithm (to base ten) of the maximum seismic wave amplitude (in thousandths of a millimeter) recorded on a standard Wood-Anderson seismograph at a

distance of 100km from the earthquake epicenter. It is important even at this stage to note that the definition of the magnitude depends on the recording instrument.

This definition has since been extended to include recordings at regional and teleseismic distances. These magnitudes also depend on the typical period (τ) of the seismic wave after it has been filtered by the instrument response. The body wave magnitude, m_b, is usually determined from the peak P-wave amplitude which has a period of $\tau = 1$ second; the surface wave magnitude, m_s, is determined from the peak surface wave amplitude which has a typical period of $\tau = 20$ seconds. These peak amplitudes are recorded respectively on Short Period (SP) and Long Period (LP) instruments of the World-Wide Standardised Seismic Network, whose peak responses are at 1 second (SP) and 20 seconds (LP).

The magnitude-frequency distribution of earthquakes usually satisfies a very important empirical relation, as follows:

$$\text{Log } N_m = a - bm \qquad (1.11)$$

where N_m is the total number of events of magnitude m or greater, a is a constant and b is usually known as the seismic b-value (Gutenberg and Richter, 1954). This distribution, an example of which is illustrated in figure 1.3(b) (section 1.2), plots as a straight line of negative slope on the log-linear axes (or effectively log-log, since magnitude is a measure of amplitude on a logarithmic scale). An average global value of the seismic b-value is widely observed to be close to 1.0, with a range of 0.5 to 1.5. Temporal changes in the b-value prior to an earthquake are often cited as earthquake precursors and have also been observed in the compressional failure of intact rock specimens (Main et al., 1989).

Figure 1.12 shows an idealized magnitude-frequency distribution for b = 1.0 with a lower magnitude cut-off of 1.5 and finite maximum magnitude of 4.0. The discrete frequency data which plot the actual log of the number of events at each magnitude interval are shown as a staircase, and the cumulative frequency data which plot the log of the number of events equal to or greater than m are shown as crosses. This idealised example shows that the slope of the discrete frequency data is equal to that of the cumulative frequency data at low magnitudes, but that the cumulative slope increases artificially at the higher magnitudes due to the finite maximum. As a result all b-value calculations in this study were screened for such possible 'edge effects' caused by the finite maximum.

1.4.2 Seismic moment

Another more recently introduced concept which describes the size of an earthquake is the seismic moment. This parameter avoids the complications of wave type and instrument response involved in the magnitude measurement, and so is more reliable as a measure of source size. It is also more easily related to geological fault parameters, allowing a direct comparison between seismic and tectonic estimates of the moment.

The seismic moment is defined as:

$$M_o = \mu A u \quad (1.12)$$

where μ is the rigidity modulus of the medium, A is the area of the dislocation surface (at that part of the fault) and u is the average slip or dislocation.

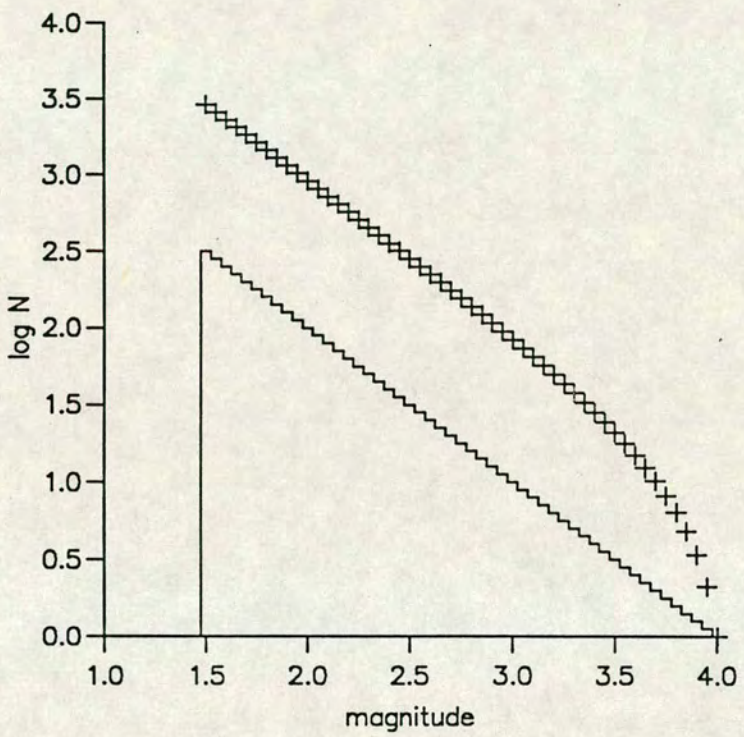

Figure 1.12 Idealized magnitude-frequency distribution. The staircase represents discrete data. The crosses represent the cumulative data, Log N ($m \geq m$) = a - bm. This synthetic example illustrates that the slope of the discrete data is equal to that of the cumulative data until the cumulative slope decreases at the higher magnitudes. The negative slope, 1.0 in this case, is the seismic b-value.

There are several assumptions that may be made to simplify the determination of M_o from seismic records. For example, if the rupture is assumed to be circular, then:

$$M_o = \mu \pi L^2 u \qquad (1.13)$$

where L is a characteristic dimension (radius) of the rupture. If the medium is then assumed to be elastic, the stress drop $\Delta\sigma$ is proportional to the strain drop $\Delta\varepsilon$ (= u/L). For a circular shear rupture, $\Delta\sigma = (7/16)\, \mu \pi \Delta\varepsilon$, and so:

$$M_o = (16/7)\Delta\sigma\ L^3 \qquad (1.14)$$

The stress drop during earthquakes is usually a constant at around 3 MPa (Scholz, 1982), implying self-similarity in earthquake source scaling. Equation (1.14) then reduces to (Kanamori and Anderson, 1975):

$$Mo = \text{constant}\ L^3 \qquad (1.15)$$

The seismic moment is also related empirically to the earthquake magnitude (m) by:

$$\text{Log}\ M_o = cm + d \qquad (1.16)$$

where c and d are constants; d depends on the stress drop and c on the relative rupture duration and the instrument time constant. Since the moment and magnitude measurements are related through this logarithmic relation, the number of earthquakes of moment M_o also shows a power-law frequency distribution, similar to that in equation (1.11) and figure 1.12. This has also been used to illustrate the self-

similarity of earthquakes (Scholz, 1990), and is more significant since there is no instrumental filter on the data. Figure 1.13 shows the relation of M_o and m_s for natural earthquake data, giving an average slope of c = 3/2, which appears to curve off at $m_s \sim 8$. This scaling will be discussed further in the next section, with reference to a dislocation model for the seismic source.

1.4.3 The dislocation model

The dislocation model of the seismic source was first proposed by Kanamori and Anderson (1975) to examine the physical basis for empirical relations between seismic parameters, including seismic moment, magnitude, energy and fault dimension L.

A fault, or circular crack, is assumed to be scale invariant and to nucleate at a point by shear displacement at constant slip velocity V_S. At the same time the crack length grows from zero at a constant rupture velocity V_R, with slip at V_S proceding behind this point. When the slip has reached a maximum value u_C in time τ_R ($u_C = \tau_R / V_S$), the crack then begins to heal (close up) from the point of nucleation. The healing front then travels at a constant velocity V_R equal to the rupture front, so that after τ_R the crack is propagating at a uniform length. Once the crack tip ceases to propagate at τ_D, the radiating crack length reduces due to healing until the crack is completely closed. τ_R is known as the rise time (the time for slip to start and stop at a point) and τ_D is the duration time of crack tip propagation. The resulting shape for a one-dimensional linear fault is a trapezium, as shown in figure 1.14.

For observations in the far field, the radiated ground displacement in the time domain is proportional to dM_o/dt (or $\dot{M}_o$), (the rate of release of moment (Aki and

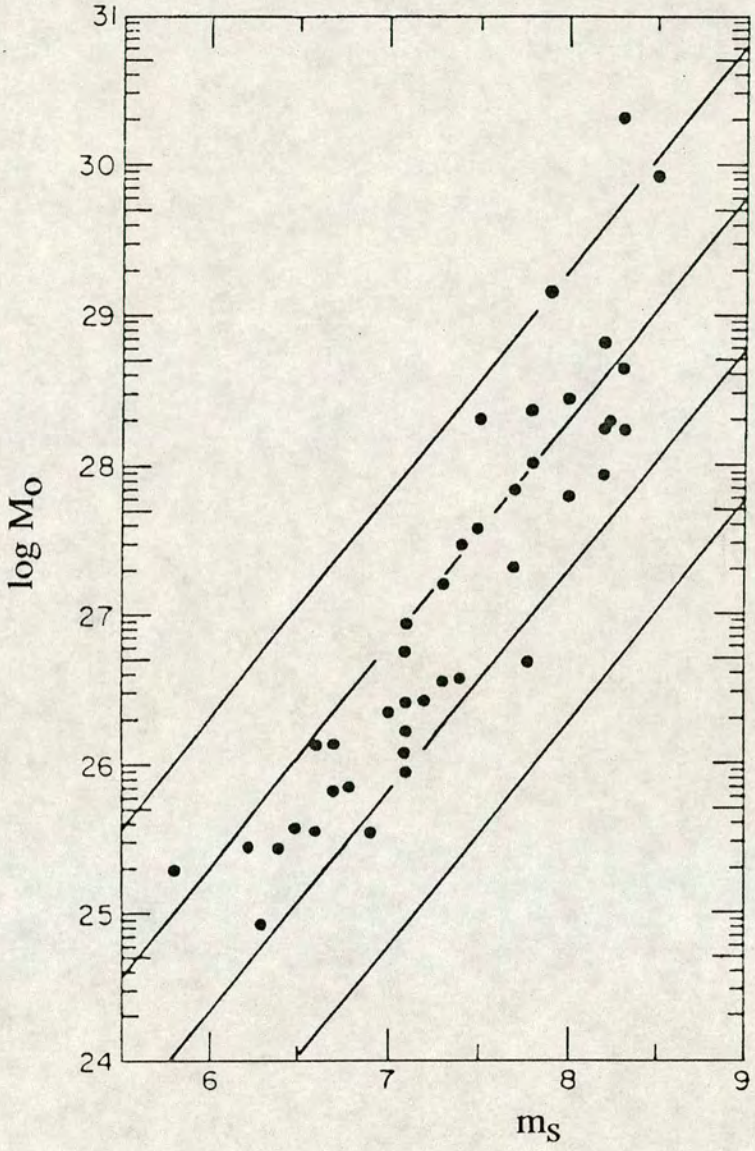

Figure 1.13 The relation between surface wave magnitude m_s and seismic moment M_o (after Kanamori and Anderson, 1975). The data are from natural earthquakes. The solid lines represent slopes of 3/2 for different values of constant stress.

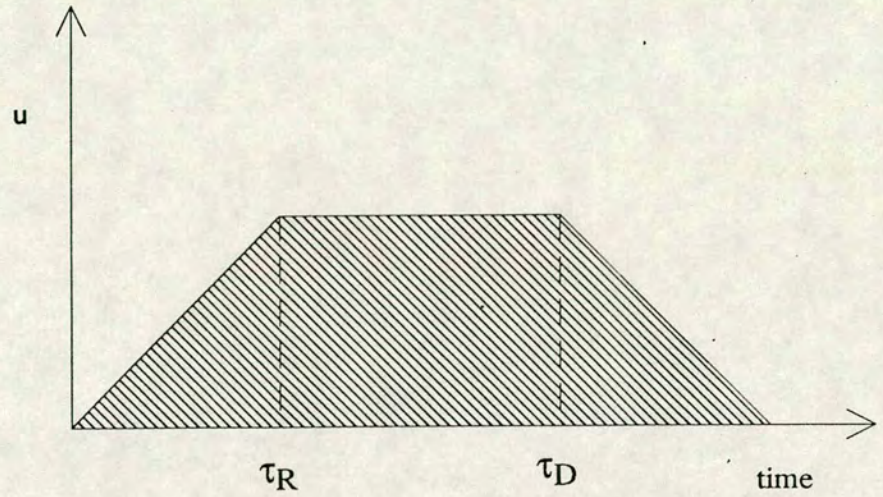

Figure 1.14 The dislocation model; u here is the radiated ground displacement in the far field.

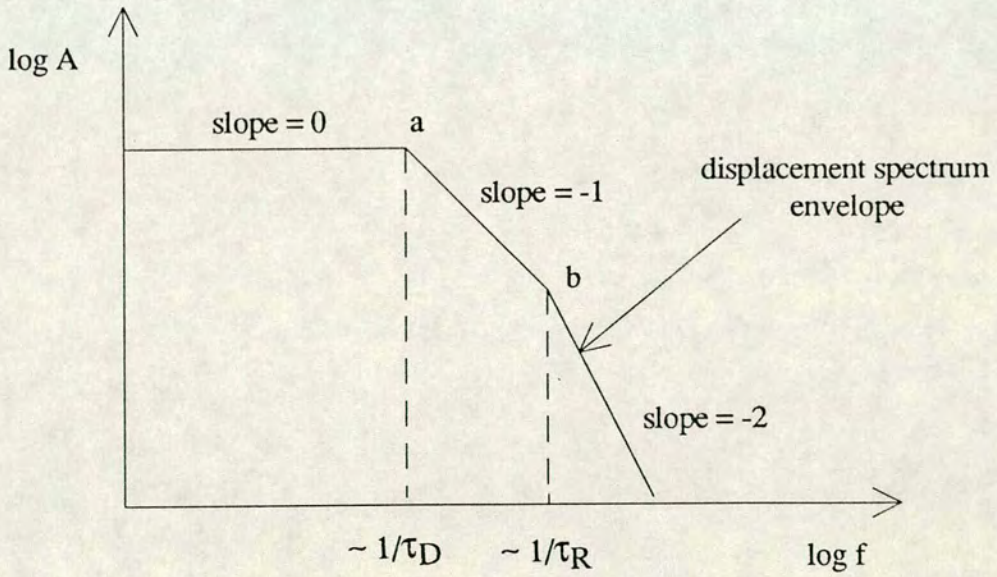

Figure 1.15 The displacement spectrum envelope produced by a fourier transform of the dislocation model.

Richards, 1980)), and so the total moment is proportional to the area under the displacement curve of figure 1.14.

This signal a(t) may then be passed through a Fourier transform (FT) to produce a displacement spectrum:

$$A(f) = \int_{-\infty}^{\infty} a(t) e^{-i2\pi ft} dt \qquad (1.17)$$

where A is the spectral amplitude, f is the frequency ($\omega = 2\pi f$), t is time. Figure 1.15 shows the envelope of the displacement spectrum produced by this transform. Three distinct slopes are evident, with gradients equal to 0, -1 and -2. The corner frequencies at the slope breaks (a and b) correspond roughly to $1/\tau_D$ and $1/\tau_R$ respectively. This spectrum may then be used to examine the moment - magnitude relationship of earthquakes of different sizes. The seismic moment is proportional to the amplitude at $f = 0$ and hence may be determined from any measurement on the flat part of the spectrum. It is independent of instrument period τ_o, or of τ_R and τ_D. However, the magnitude is obtained from the amplitude at a specific frequency f_0, where $f_0 = 1/\tau_0$ may be off the flat part, and hence grossly underestimates the low-frequency energy.

Figure 1.16 illustrates the effect of changes in the spectrum envelope with an increase in earthquake moment. A_o represents a small earthquake where the instrument period is below the first corner frequency, and hence $\log M_o \propto m$. As earthquake size is increased to A_1, where $\tau_o = \tau_R$, the instrument just picks up the flat part of the spectrum and this scaling is preserved. However, when the earthquake size is increased to A_2, the amplitude at f_0 does not reflect the seismic moment

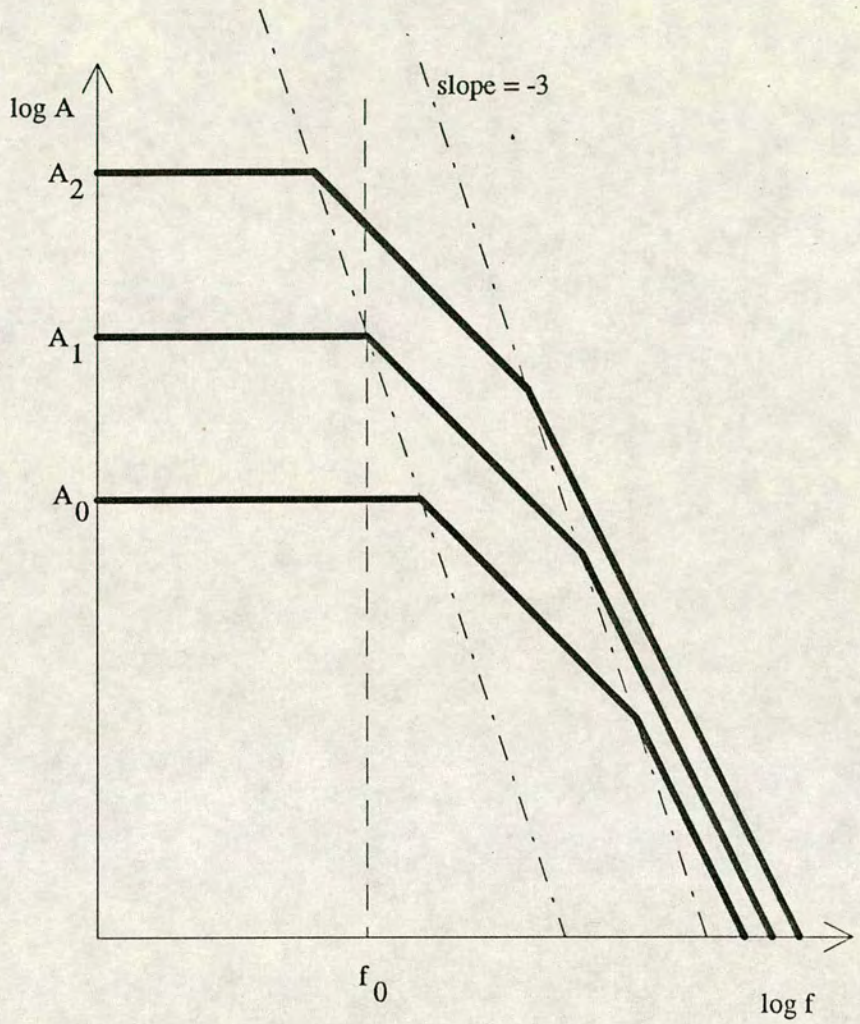

Figure 1.16 Schematic diagram of the changes in the displacement spectrum envelope with an increase in earthquake moment.

directly. Therefore, the period of the recording instrument is an important factor in determining the effectiveness of a magnitude scale. Ideally a broad band instrument which records the whole frequency band would be preferable.

The moment - magnitude relation predicted from this spectrum is plotted in figure 1.17 (Kanamori and Anderson, 1975). From this figure it can be seen that; (1) there are three regions corresponding to values of c (from equation (1.12)) of c = 1, c = 3/2, c = 3; and (2) for large seismic moments, the magnitude scale becomes saturated due to the corner frequency moving to lower and lower frequencies, as in figure 1.13. This saturation occurs at limits of $m_s < 8$ and $m_b < 7$ on the different magnitude scales, due to the higher frequency of the body wave scale.

Electronic seismographs usually record the wave velocity, which may be found by differentiating the displacement spectrum. The resultant velocity source pulse is illustrated in figure 1.18. Since it is preferable that the instrument records with the frequency band giving the highest signal to noise ratio, the instrument response is usually chosen to peak in the region of peak velocity for the earthquake of interest, where $1/\tau_D < f_0 < 1/\tau_R$. This corresponds to the slope = -1 region of the displacement spectrum (figure 1.15) and so corresponds to c = 3/2 (figure 1.17). Therefore, in earthquake studies, a value of c = 3/2 is most usual (Kanamori and Anderson, 1975).

1.4.4 Seismogenic depth and seismic scaling

The seismogenic depth of the crust is the finite depth to which seismic waves may be generated by dynamic slip in the brittle crust, before encountering the transition to more ductile rheology at depth due to increased temperature and pressure. This part of the crust has also been termed the schizosphere (Scholz, 1990)

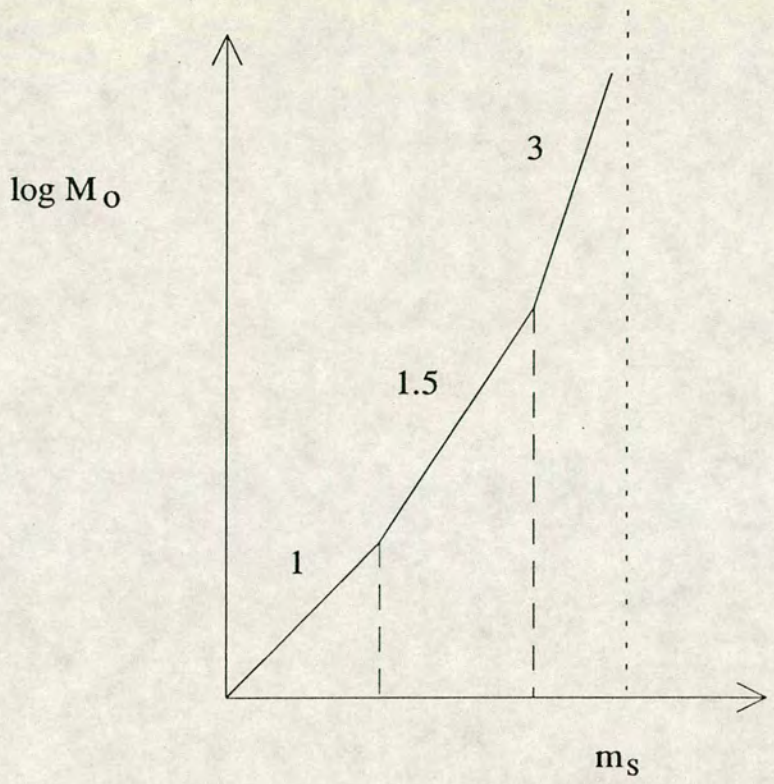

Figure 1.17 Schematic diagram of the relation between moment and magnitude, illustrating the three possible values of the constant c. (Kanamori and Anderson, 1975).

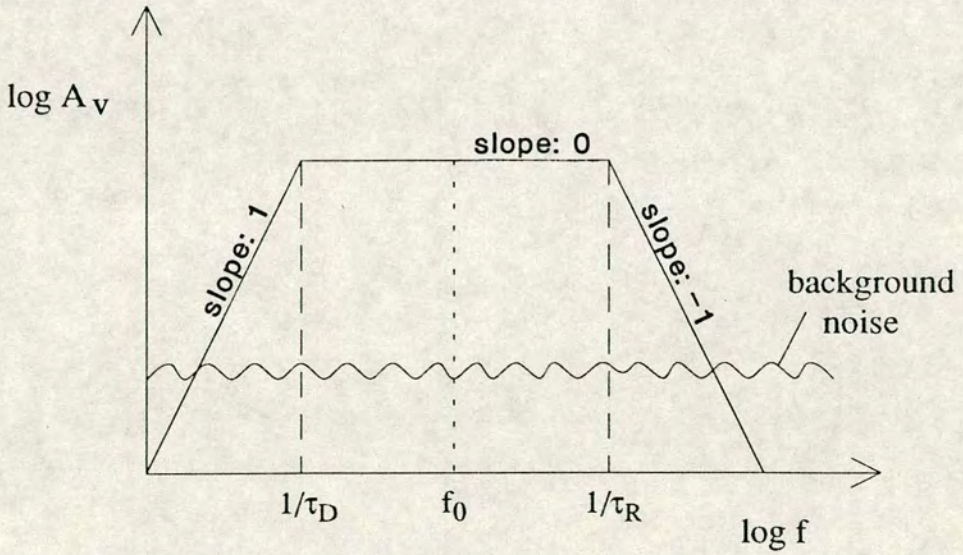

Figure 1.18 Velocity spectrum of a seismic source. The peak signal to noise ratio is obtained in the flat part of the velocity spectrum between $1/\tau_D$ and $1/\tau_R$.

and is illustrated in figure 1.19. 'Small' earthquakes can grow unlimited by dimension in both length and depth. However, although large earthquakes similarly have no geometric bound to their length, the depth (down-dip) to which they can expand is limited by the thickness of the seismogenic layer in that region. Therefore, the size of the earthquake affects its dimensionality and in turn affects the scaling of its seismic moment (from equation 1.9). Small earthquakes scale as $M_0 \propto L^3$, whereas large earthquakes limited by the seismogenic depth scale as $M_0 \propto L^2$.

Globally, the seismogenic depth varies depending on the tectonic regime, since this affects heat flow and the subsequent depth at which the transition to ductile flow occurs. For example, for the San Andreas fault, where the seismogenic depth is about 15 km, a break in scaling occurs at a magnitude of about 6 - 6.5 (Scholz, 1990). However, in volcanic provinces high geothermal temperatures from rising magma reduces the size of the seismogenic layer, and in subduction zones friction from the cool descending slab causes a variable brittle-ductile transition. In these regions, the magnitude-frequency distribution of earthquakes may not show the typical self-similarity over the whole range. For example Pacheco et al. (1992) show a change in frequency-magnitude scaling due to the L^3 to L^2 transition in global catalogues. Figure 1.20 shows a further example of this effect in the discrete magnitude-frequency plot from the seismicity preceding the 1980 Mount St Helens eruptions (Main, 1992). Here, the break in fractal scaling occurs at a magnitude of about 4.5, due to the shallower seismogenic depth in a zone of elevated geotherms. A break in scaling at magnitude 7.5 may be observed at subduction zones (Scholz, 1990) where the depth of the seismogenic layer (schizosphere) is much greater. Therefore, this effect should be considered as an important secondary factor in earthquake scaling, particularly at higher magnitudes.

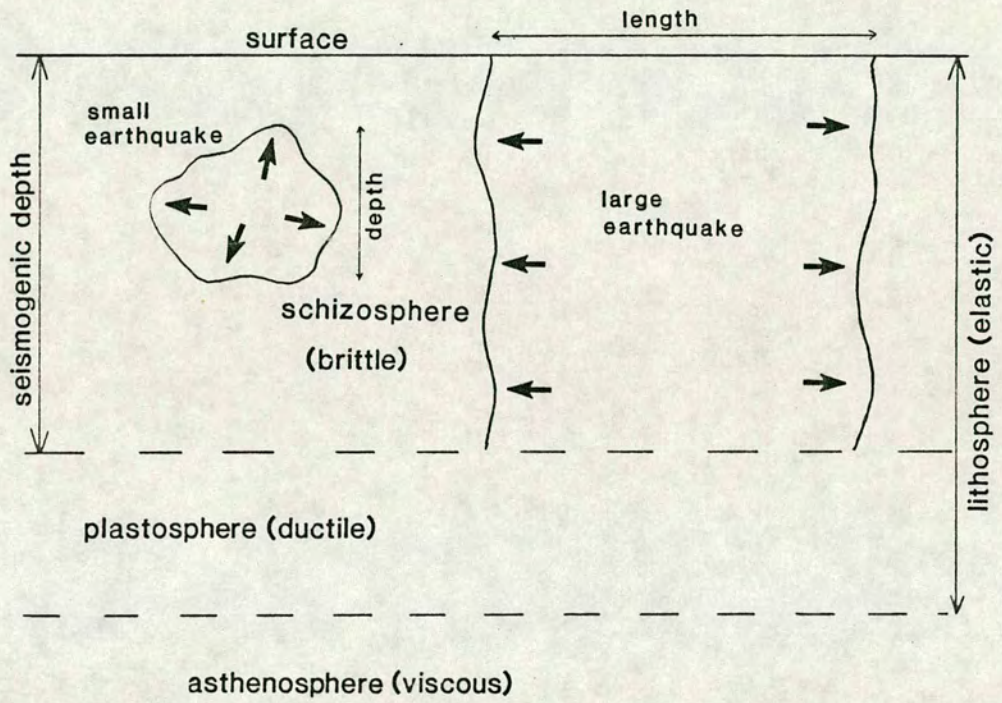

Figure 1.19 Schematic representation of the crust, showing the seismogenic depth of the schizosphere within which seismic waves may be generated, and its influence on earthquakes of varying size (adapted from Scholz, 1990).

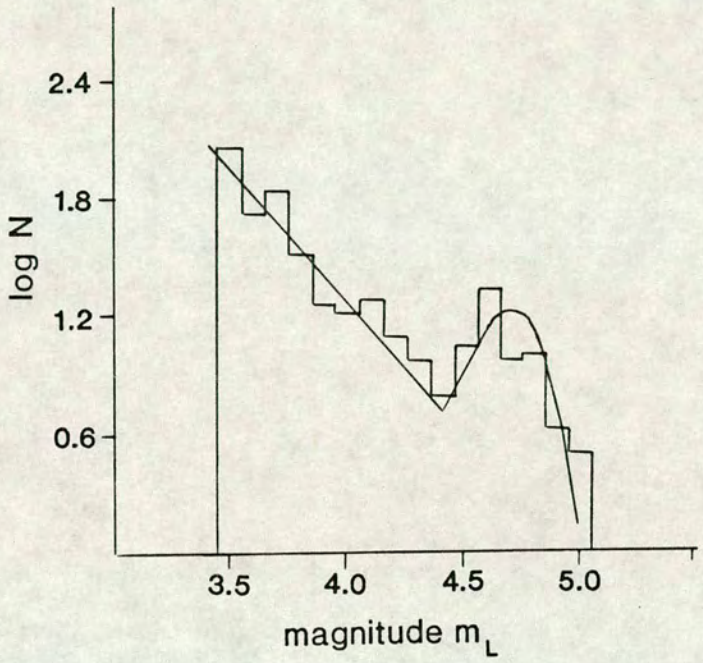

Figure 1.20 Discrete magnitude-frequency plot of the seismicity preceding the 1980 Mount St Helens eruptions, illustrating a break in fractal scaling at a magnitude of 4.5 (Main, 1992).

1.4.5 Acoustic emission

Acoustic emissions (AE) are the transient elastic waves generated in a solid by rapid, usually localized, changes in stress or strain accompanying deformation mechanisms such as the nucleation or growth of fractures. Figure 1.21 shows a typical 'burst type' emission signal (Pollock, 1988) associated with microcracking. This implies that even though the average macrocrack growth may be slow and subcritical, the macrocrack and its aureole of microcrack damage actually grows by repeated small increments which are dynamic enough to produce detectable AE. When an elastic AE wave hits a piezoelectric transducer, the transducer is stimulated to give a varying voltage output that appears as a wave packet, and is termed an AE event. A threshold voltage needs to be set in order to cut out extraneous background noise. The amplitude of each event is defined as the peak voltage attained by the waveform. It is expressed in decibels (dB) relative to an arbitrary value of 1 microvolt at the sensor (Pollock, 1988). Events with amplitudes < 35 dB are considered small, amplitudes of 35 - 55 dB medium, amplitudes of 55 - 75 dB large and events with amplitudes > 75 dB very large. The number of threshold crossing counts (sometimes called ringdown counts) is the the number of times the AE signal crosses the threshold voltage in a particular wave packet. For example on figure 1.21 the ringdown count is nine. A minimum of 1 count for the smallest acceptable event was taken in the analysis of the acoustic emission data to allow use of the maximum possible data set. The duration is defined as the time from the first to the last threshold crossing. The energy of the wave packet may be determined from the area under the rectified signal envelope. However, this is only a relative measurement with no units, and so was not considered useful for the present quantitative study.

The frequency band of the recording transducer has a similar limitation to that of the seismograph, as described in section 1.4.3. To allow the transducer to be small

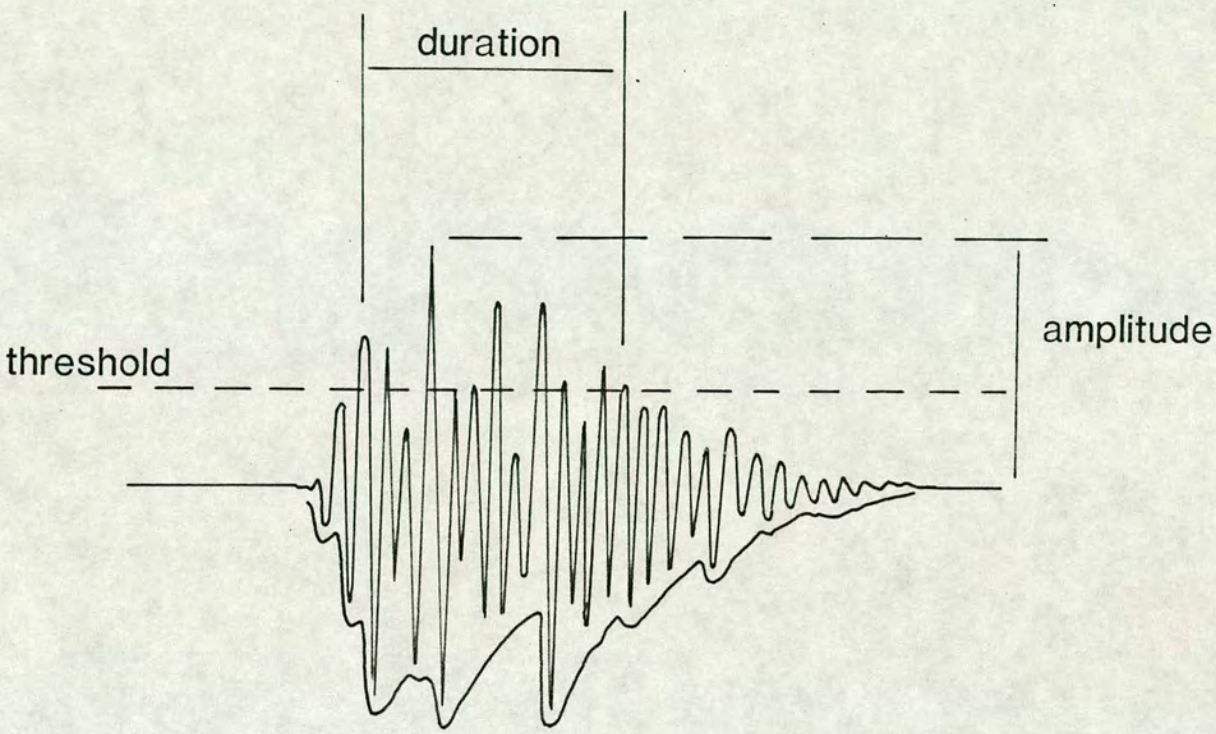

Figure 1.21 Schematic diagram of a typical 'burst type' emission signal (Pollock, 1988) associated with microcracking, illustrating the acoustic emission parameters monitored for each event during fracture.

enough to detect the AE from the test specimen, the recorded frequency band may be higher than $1/\tau_R$ for the acoustic source, implying a value of c = 3 from the dislocation model. This has been inferred in previous experimental results on tensile tests of the kind examined in this thesis (Main et al., 1989, 1990).

Since it is not possible routinely to measure a seismic moment from acoustic emission in the laboratory at present, this study uses the AE magnitude data, combined with the seismic moment scaling relations described in section 1.4.2. Figure 1.22 shows a typical acoustic emission amplitude-frequency plot monitored during a tensile crack propagation experiment. Amplitudes are plotted on the logarithmic decibel scale, so this plot is similar to the magnitude-frequency distributions of natural earthquakes (for example, figure 1.3(b)). It is therefore reasonable to use the seismological techniques described above to quantify the AE monitored during crack growth experiments in the laboratory.

As described in section 1.4.1, the negative slope of figure 1.3(b) gives the seismic b-value. It follows that the slope of the AE amplitude-frequency plot (figure 1.22) is an equivalent b-value. However, a correction factor of 20 must be introduced into figure 1.22 to allow for the fact that AE amplitudes are measures in decibels whereas the Richter magnitude is defined in terms of the logarithm of a peak amplitude (section 1.4.1). Since the amplitude in dB = 20 log A / A_0 and the amplitude in magnitude units = log A / A_0, it follows that the amplitude in magnitude units = the amplitude in dB / 20. After this correction, the earthquake magnitude-frequency relation given in (1.11) may be rewritten as an AE amplitude-frequency relation:

$$\text{Log } N = a - b \ \text{Log} \frac{A}{A_o} \qquad (1.18)$$

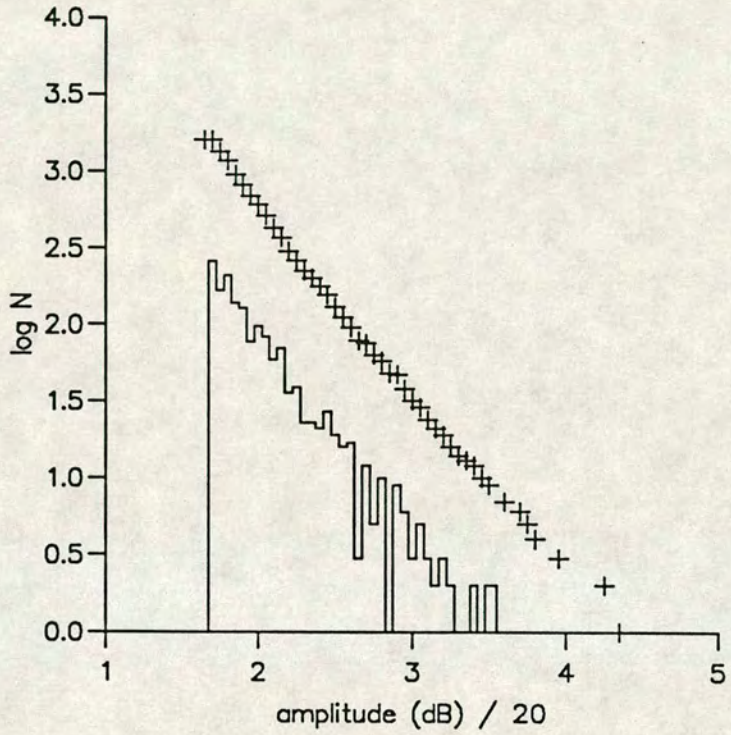

Figure 1.22 Typical acoustic emission amplitude-frequency plot from a 'dry' test run in air of ambient humidity at a loading ram displacement rate of 0.16×10^{-6} ms^{-1}. The amplitude axis incorporates a correction factor of 20 so that the slope is equal to the AE b-value.

Since the AE amplitudes monitored are already logged (within the measuring instrument) and relative to an arbitrary value A_0, the slope of the relation in figure 1.22 may be expressed as the AE b-value.

1.5 Scaling of structure and seismicity

In order to quantify any possible relationship between the structure and seismicity produced during tensile fracture, a method is required to combine the separate quantitative measurements of structure and seismicity described in the preceding sections. In previous work this has simply been inferred from the dislocation model of a seismic source (section 1.4.3) and a fractal interpretation of the seismic b-value (section 1.2). Several authors (for example, Aki, 1981; King, 1983; Main et al., 1989; Turcotte, 1989; Main et al., 1990) have shown that by combining equations (1.3), (1.11), (1.14) and (1.16), the length distribution exponent is proportional to the seismic b-value, as follows:

$$D = \frac{3\,b}{c} \qquad (1.19)$$

Implicit in this formula is the assumption that moment scales with fault or fracture length cubed, for faults smaller than the seismogenic depth of the crust, and hence the stress drop is constant (Scholz, 1982). Therefore, the exponent D is related to the seismic, or AE, b-value and a scaling constant c which depends on the recording instrument. As described in section 1.4.3, the value of c may be taken as 1, 1.5 or 3. The common value for intermediate earthquake studies is c = 3/2 (Kanamori and Anderson, 1975), and so the usual scaling takes the form:

$$D = 2\,b \qquad (1.20)$$

giving $1 < D < 3$ for seismic b-values in the observed range $0.5 < b < 1.5$. In previous experimental work on tensile fracture tests, (Main et al., 1990), data in the range $1 < b < 3$ has suggested a value of $c = 3$ and $D = b$, and $1 < D < 3$ also. This range is consistant with the fractal interpretation of D first proposed by Aki (1981).

Although some previous work has attempted to relate structure and seismicity (eg. King, 1983; Shaw and Gartner, 1986; Hirata, 1989; Scholz, 1990; Sornette et al., 1991, as well as the theoretical papers listed above), a direct relationship between b and D had not actually been observed before the present work was completed. This study combines quantitative data from AE seismicity (the AE b-value) and structure of the microfracture system (the length distribution exponent D) from single laboratory specimens representing a controlled single increment of fracture growth. This allows an objective assessment of the scaling properties of seismicity and structure, and provides an independent check on this large body of previous work. Fieldwork data involving the measurement of natural tensile fracture length distributions in north east Iceland were also examined to provide a natural example for comparison with the artificial results. Natural length-width distributions were also obtained from Iceland, and provide results to compare with previously proposed fault growth models (section 1.2, discussion).

Chapter 2 Experimental Method

As described in the previous chapter, this study is concerned with tensile fracture of rock and its associated seismicity and structure. To examine this on a laboratory scale, the design of a suitable experiment was required. This chapter describes the particular method chosen, and presents some preliminary fracture mechanics results determined by the present experimental series. These results lay the foundation for the interpretation of the new results from this study to be described in the following chapters, but are important both in themselves in confirming previous work and in proving the experimental method.

2.1 Introduction to method of testing

Several tensile tests originally used to fracture relatively homogeneous materials such as glass and ceramics have recently been adapted to study relatively more heterogeneous rock samples. These include notched beam tests, the double cantilever beam test, double torsion, chevron notched techniques and internally pressured thick walled cylinder tests. A comprehensive review of these testing methods is given by Meredith (1983), and more recently a summary of tensile testing techniques available has been given by Atkinson and Meredith (1987b) and hence is not repeated here. The test chosen as most suitable for this study was the double torsion test in its constant displacement rate mode. This has several important advantages for the present combined structural and seismic study, as outlined in the following sections.

2.1.1 The double torsion method

This method was first introduced by Outwater and Gerry (1966) to measure the fracture energy of glass, and later used by Kies and Clark (1969) to study subcritical crack growth and failure times in glass. The specimen is basically a thin, rectangular plate which is loaded in four-point bending at one end, and is shown in figure 2.1(a).

A compressive load, P, is applied at one end of the specimen by two loading points positioned symmetrically astride the pre-cut central axial crack guiding groove. Although the applied load is compressive, the crack propagates in tension from the underside of the specimen, since the specimen rests on two support rollers (Fuller, 1979). Previous observations have shown that the crack front is curved and extends further along the lower surface than the upper surface (Evans, 1972) as shown in figure 2.1(b). This loading configuration and direction of crack growth may suggest that a component of the failure is in mode III due to shear stresses. However, tensile stresses due to the applied bending moment are evident, and stress intensity results from previous double torsion tests show a good correlation with established K_I values, indicating that failure is in fact mode I (tensile) (Evans, 1972; Williams and Evans, 1973).

The double torsion technique has a number of advantages over other tensile fracture mechanics testing methods:

1. The simple geometry allows easy specimen preparation.
2. The load applied is compressive, and does not require a stiff (low compliance) loading machine.
3. The stress intensity factor K_I is independent of crack length over much of the specimen length.

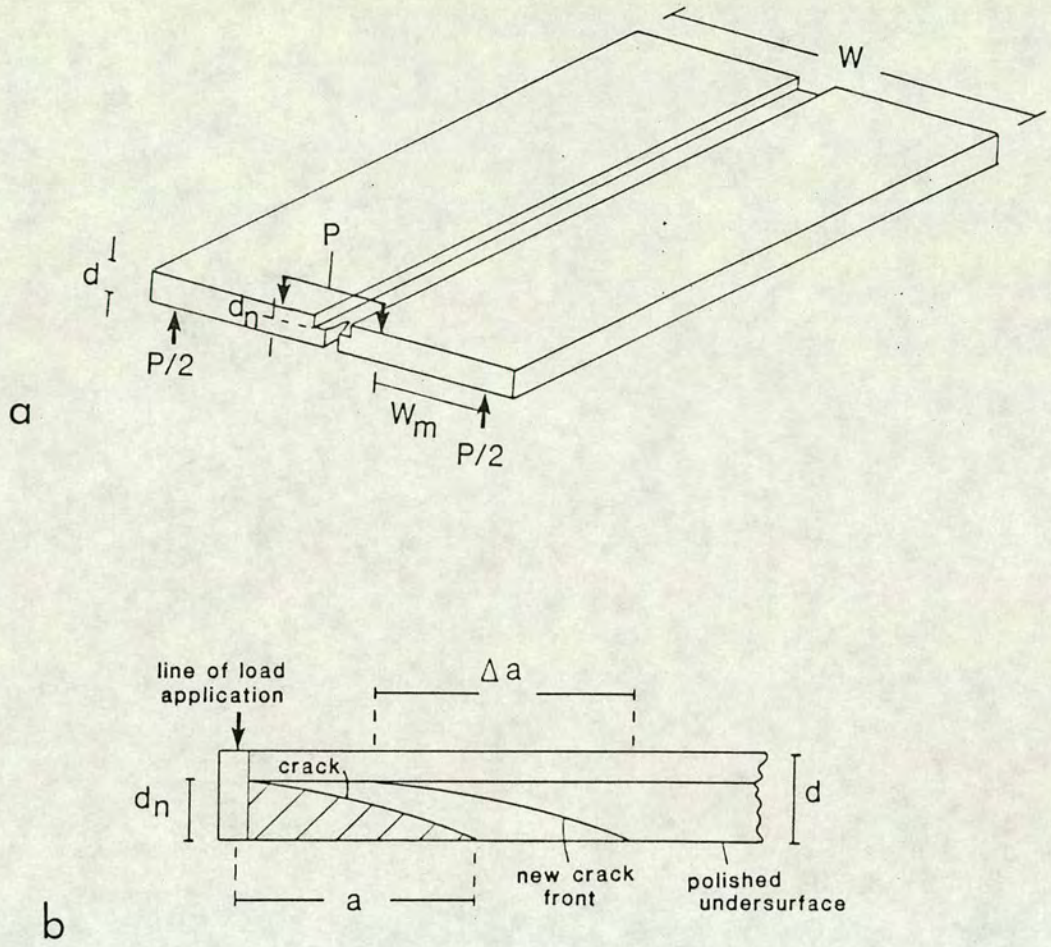

Figure 2.1 Schematic drawing of a double torsion test specimen.

(a) The guide groove for the main crack is set upwards to ensure that the polished undersurface experiences maximum tension as the load P is applied. Thickness d is equal to 3-4 times the typical grain size of the rock sample. W is the width, d_n is the thickness of the specimen within the guide groove ($d_n = 2/3d$), W_m is known as the semi-moment arm, and is the distance between adjacent support point and point of load application. The following ratios of dimension were used in the present study: W = 12 d; Length = 3 W.

(b) Axial cross section view, illustrating the curved nature of the crack front (after Evans, 1972).

4. The stress intensity factor is directly proportional to the applied load, and hence is relatively easy to measure after a simple calibration.
5. The specimen is virtually a two-dimensional plate that may be polished, thereby allowing direct inspection of the microfracture system produced around the main macrocrack on the undersurface that experiences maximum tension. This is specifically useful for this study.

There are three methods of conducting a double torsion test. These depend mainly on the loading criteria, and so it is also necessary to describe the reasons why the constant displacement rate technique was chosen. A brief outline of each is given below.

Constant load method

In the original double torsion tests, a constant load method was used (Kies and Clark, 1969) where the load is kept constant and the deflection of the plate is monitored as the crack grows. In this method, a constant 'dead', i.e. fixed, load provides a constant K.

Load relaxation method

Much previous work involving the double torsion specimen has used a load relaxation technique (Evans, 1972), where a precracked specimen is loaded rapidly up to a load just below the critical load for dynamic failure. The loading point is then fixed, and the load is allowed to decay as a result of stable subcritical crack growth. This method has the advantage of producing a wide range of stress intensity and crack velocity determinations for a single test, since K is independent of crack length and decreases as the load relaxes, and the crack velocity, V, is related to the

instantaneous load and rate of relaxation. If the prime variable of interest is the velocity of crack propagation, then this technique is most useful (e.g. Atkinson, 1982; Meredith and Atkinson, 1983; Atkinson, 1984; Swanson, 1984; Meredith and Atkinson, 1985). For example, each of the curves on figure 2.2 may be obtained from only one relaxation test. This figure shows the relationship between stress intensity and crack velocity at different temperatures and pressures for subcritical crack growth (a schematic figure illustrating this relation is given in figure 1.7(a)). The two axes are plotted on logarithmic scales, and the slope of each of the resulting straight lines is known as the subcritical crack growth index, n. One of the problems reported with this method, however, involves a poor ability to repeat the positions of the K-V curves on the K axis, although n is reasonably repeatable (for example, see Atkinson and Meredith, 1987a, b; Sano, 1988).

Constant displacement rate method

In the present work, the constant displacement rate method was chosen, since much work has already established the K-V relationship for a variety of rock types, and our aim now is to relate crack growth and the associated seismicity to the resulting structure of the cracks produced. It is therefore more important to apply uniform conditions of load and stress intensity over as much of the specimen volume as possible. In this method, the load, P, is applied to the specimen at a constant displacement rate. The load is seen to increase approximately linearly until a critical load is reached and subcritical crack growth begins. The increasing displacement is then exactly compensated for in this loading geometry by the change in specimen compliance due to cracking, and the load in theory remains constant as the crack grows quasi-statically along the specimen. Once inertial effects dominate, the material fails dynamically and the load drops drastically. Since we are only concerned with the

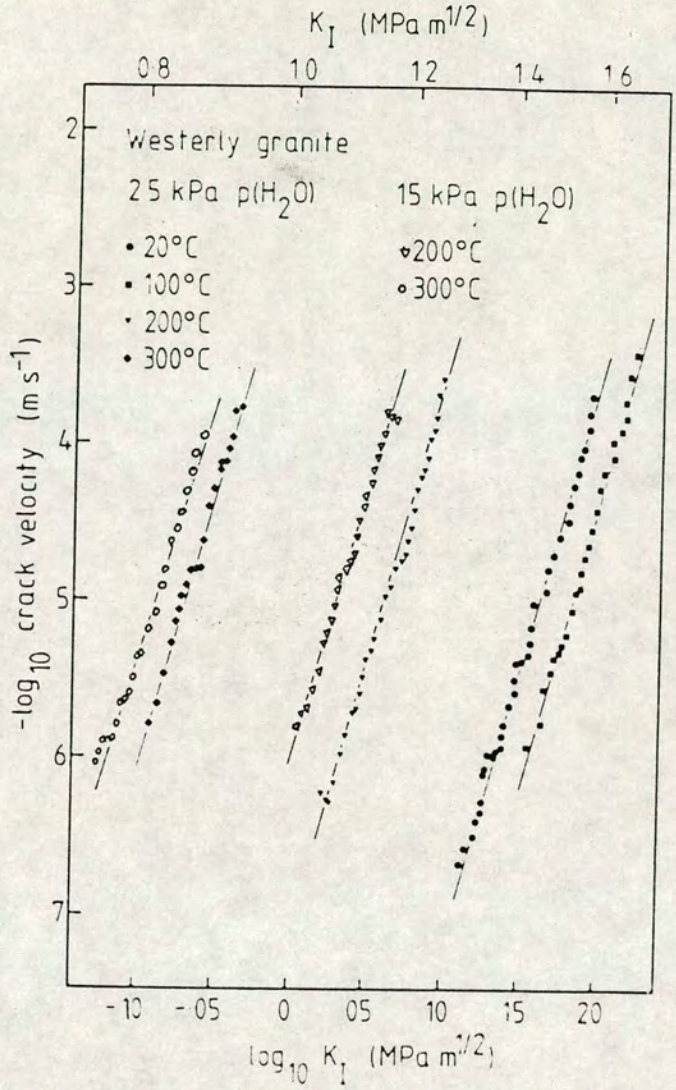

Figure 2.2 **Crack velocity as a function of stress intensity from relaxation tests on Westerly granite at different temperatures and pressures (Meredith and Atkinson, 1985).**

data produced after the onset of microcracking, during the period of constant load, it was considered unnecessary to precrack the specimens as is often necessary in load relaxation experiments. It is the constant loading criterion during crack growth that produces the uniform conditions over much of the specimen that is important to the structural study of the fracture system, at the inevitable expense of fewer results per test. To summarise, the main advantage of the constant displacement rate double torsion test is that the stress intensity is directly proportional to the load. This produces a constant stress intensity over approximately the middle third of the specimen when the specimen dimensions are considered to reduce edge effects for reasons discussed in the next section. This proved to be a sufficient surface for the structural investigation of the fracture pattern.

2.1.2 Specimen constraints

The geometry and dimensions of the double torsion specimen have previously been shown to be a relatively important factor in the double torsion test method.

The specimen thickness, d, is largely dependent on the grain size of the rock chosen, so that the propagating crack front must cross at least ten grains. However, as the crack propagates at an acute angle to the polished surface, figure 2.1(b), the specimen thickness can be much less than ten times the grain size (Meredith and Atkinson, 1983). In this series of tests, a specimen thickness of 3-4 times the typical grain size was chosen as sufficient.

The width/thickness ratio is also important and may be a factor in the unrepeatability of K_I data in specimens with a width/thickness ratio of less than 12 (Evans, 1972; Atkinson, 1979; Meredith, 1983). It is possible that compressive contact stresses between the upper parts of the torsion arms are more than negligible

in relatively thick specimens (Fuller, 1979). Therefore, a width/thickness ratio of approximately 12 is a necessary minimum to alleviate this problem. A correction factor for the finite specimen width can also be included in the K_I calculation (see section 2.3.2).

The ratio of specimen length to the length of the propagating crack is also of primary importance. Where the crack is either a very small or a very large proportion of the specimen length, the calibration of load P to stress intensity K_I is affected due to edge effects. It has previously been found that the length/width ratio must be greater than 2 (Pletka et al., 1979) in order to produce a reasonably large region of constant stress intensity within the middle third of the specimen. In the present work, a length/width ratio of 3 was adopted, so that the middle third of the specimen length at least is under constant K conditions.

The specimen has an axial groove to guide the main crack. This is essential when testing heterogeneous materials such as rock, in order to ensure that the main crack propagates along the central axis of the specimen. However, the geometry of the groove is also an important factor in the design of the specimen, as it influences the stress field in which the crack is propagating and affects the interaction of subsidiary crack growth at the crack tip. Previous investigations have shown that the guide groove/specimen thickness ratio should not exceed 0.5 (Pletka et al., 1979), or 0.3 (Raju, 1981) as adopted for this study. Also in much previous work, the guide groove was located on the undersurface of the specimen. However, as we are interested in the structure of the tensile cracks produced on the undersurface that experiences maximum tension during the test, in this study the guide groove was set upwards. In order to enhance the appearance of the subsidiary microcracking, the undersurface was polished prior to testing. The specimen also has a sharp notch at the loading end to provide an initial stress concentration to initiate crack propagation.

The choice of a suitable rock type to be tested is also subject to conditions. As the thickness of the specimen is dependent on the grain size, in turn this affects the width/thickness and length/width ratios, and so a relatively fine grained rock is required to maintain a reasonable overall specimen size. In much previous work on crystalline material, well characterised 'standard' rock types, for example, Westerly granite or Oshima granite have been used. However, it was decided, for the present work to find an equivalent British rock type, oriented samples of which could be collected from areas of relatively well documented tectonic history. In order to reduce the number of controlled variables to a minimum, the test samples were obtained from field exposures of relatively unaltered, fine-grained igneous rock with no evident tectonic fabric and no obvious pre-existing small scale fractures or joints, to ensure that any fractures evident after the test were produced during the test. An important area of future work will be to quantify the effects of material anisotropy such as metamorphic fabrics in various different rock types.

Two crystalline rock types, fine grained Loch Uisg microgranodiorite and slightly coarser grained Ballachulish granite, both from North West Scotland, were used in this programme in order to allow any possible effects of specimen size on the test results to be determined. Petrological and field descriptions are given in Appendix A. A sample of basalt, as a representative basic rock, was also collected, but time was not sufficient to allow preparation and a thorough series of tests. Therefore, the study is concentrated on granitic rocks.

2.2 Experimental set up and procedure (mechanical)

The series of double torsion experiments that is central to this study was carried out in two sessions, during April-July 1991 and August-September 1992, in

the Fracture Mechanics Laboratory, Department of Geological Science, University College London. There were two main aspects to the tests; (1) mechanical loading, and (2) acoustic emission monitoring. In this section I describe the mechanical set up and conditions of the test runs. The next section will deal with the experimental fracture mechanics results from the tests. The monitoring of acoustic emission will be described in section 2.4.

The loading configuration, illustrated in figure 2.3 (and the photograph of figure D.1), consists of a stiff reaction frame onto which is attached a hydraulic load actuator with 10 kN load cell, constructed by Servotechnique Ltd. The actuator is controlled by a hydraulic servo-valve under displacement control from the extensometer. This servo-controlled hydraulic loading system provides the relatively accurate slow constant displacement rates, necessary for the tests, using feedback from the extensometer signal relative to a pre-selected displacement rate set on the ramp generator. For the tests described here, the extensometer was calibrated to output a voltage of ± 10 v DC for a displacement of ± 1 mm. The machine may be operated in either coarse or fine displacement control, allowing either large movements for specimen location purposes or very fast displacement rates; or smaller, more accurate movement for tests purposes. Under extension control, with the extensometer calibration of ± 1 m^m = ± 10 v, a displacement rate of 100% min^{-1} gives 1 mm (= 10 volts) of movement per minute, therefore for example 1% min^{-1} = 0.01 mm min^{-1} (or 0.16 x 10^{-6} ms^{-1}).

The specimen must be accurately located in the jig assembly so that the two ball bearings on the loading ram settle exactly symmetrically over the central axial groove of the jig (and over the central groove of the specimen when it is in place) to apply the load evenly to the specimen, and within a reasonable short distance from the end of the specimen with the starting notch. The specimen rests on two metal

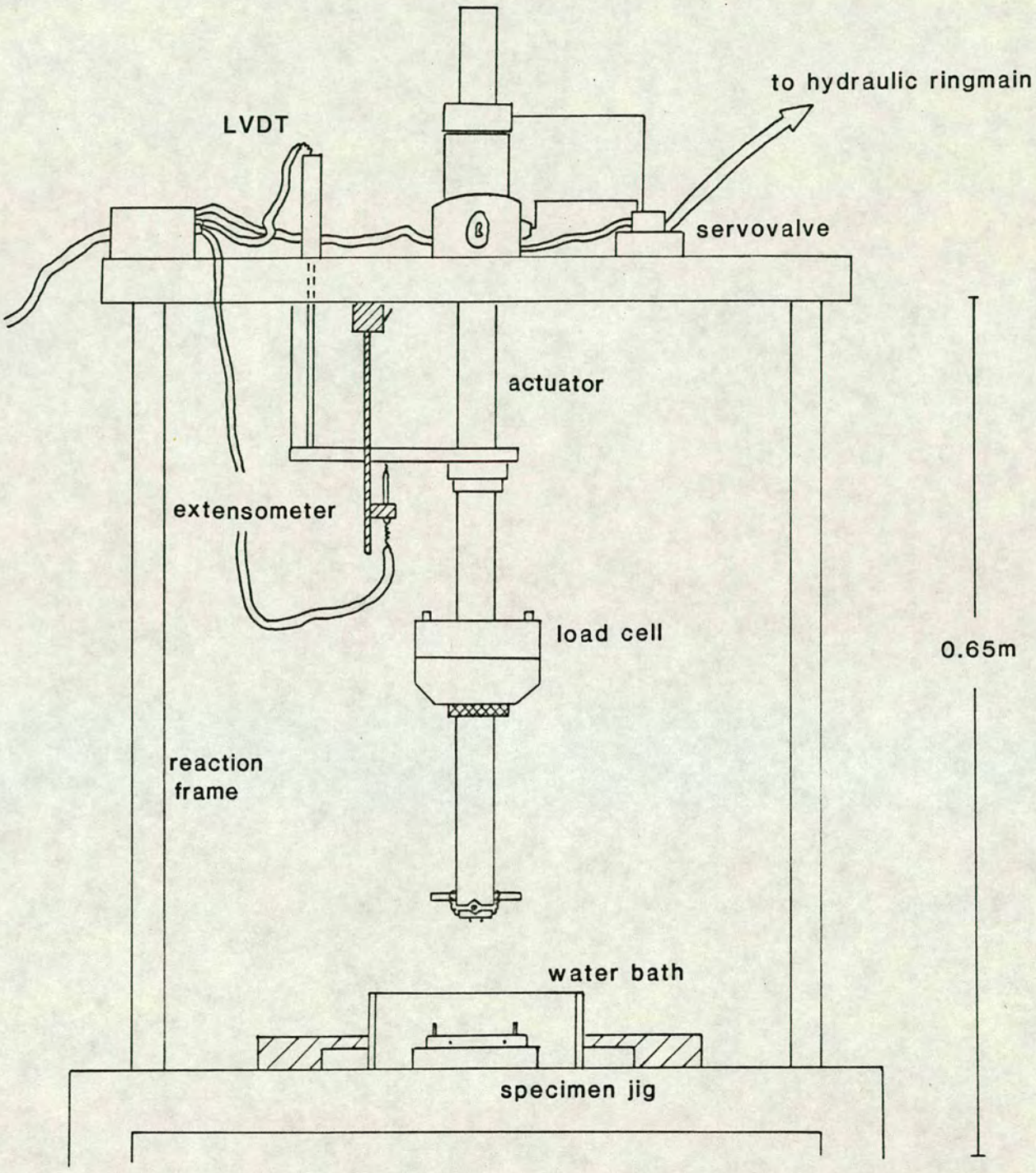

Figure 2.3 Double torsion loading configuration and set up, (Fracture Mechanics Laboratory, University College London). The 10 kN actuator is controlled by a hydraulic servovalve. Displacement is monitored by the linear variable differential transformer (LVDT) and extensometer.

rods, and must be positioned exactly central and parallel (a photograph of the specimen jig is given in figure D.2). Adjustment screws are provided so that this specimen positioning can be accurately accomplished. A summary diagram of the experimental set up is shown in figure 2.4. During each test the controlling variables were displacement rate, fluid presence and specimen size. The displacement rates varied between 0.016×10^{-6} ms^{-1} and 5.0×10^{-6} ms^{-1}. Experimental running times varied from 30 seconds to 6 hours. 'Air-dry' tests with no fluid present at the crack tip were run in air at ambient humidity. 'Wet' tests were carried out by totally immersing the specimens in the water bath filled with de-ionized H_2O. One 'damp' test was carried out by presoaking the specimen in water and carefully sponging water onto the specimen during the test to examine an intermediate case. The tests were carried out under ambient conditions of pressure and temperature. Several tests were stopped before failure to allow examination of the structure ahead of the propagating crack tip. Summary details of the tests carried out in both sessions are given in Appendix B.

2.3 Experimental fracture mechanics results

2.3.1 Compliance calibration

The compliance calibration is a useful method to obtain the fracture parameters for the specific specimen type in use. Compliance, k, is defined as the displacement of the load application points (y) per unit of applied load or force (P), i.e. $k = y/P$ (the reciprocal of stiffness). A compliance calibration of the double torsion specimen (Evans, 1972) shows that the displacement, y, is linearly related to the crack length, a, and applied load, P, as follows:

$$y = P (B a + C) \qquad (2.1)$$

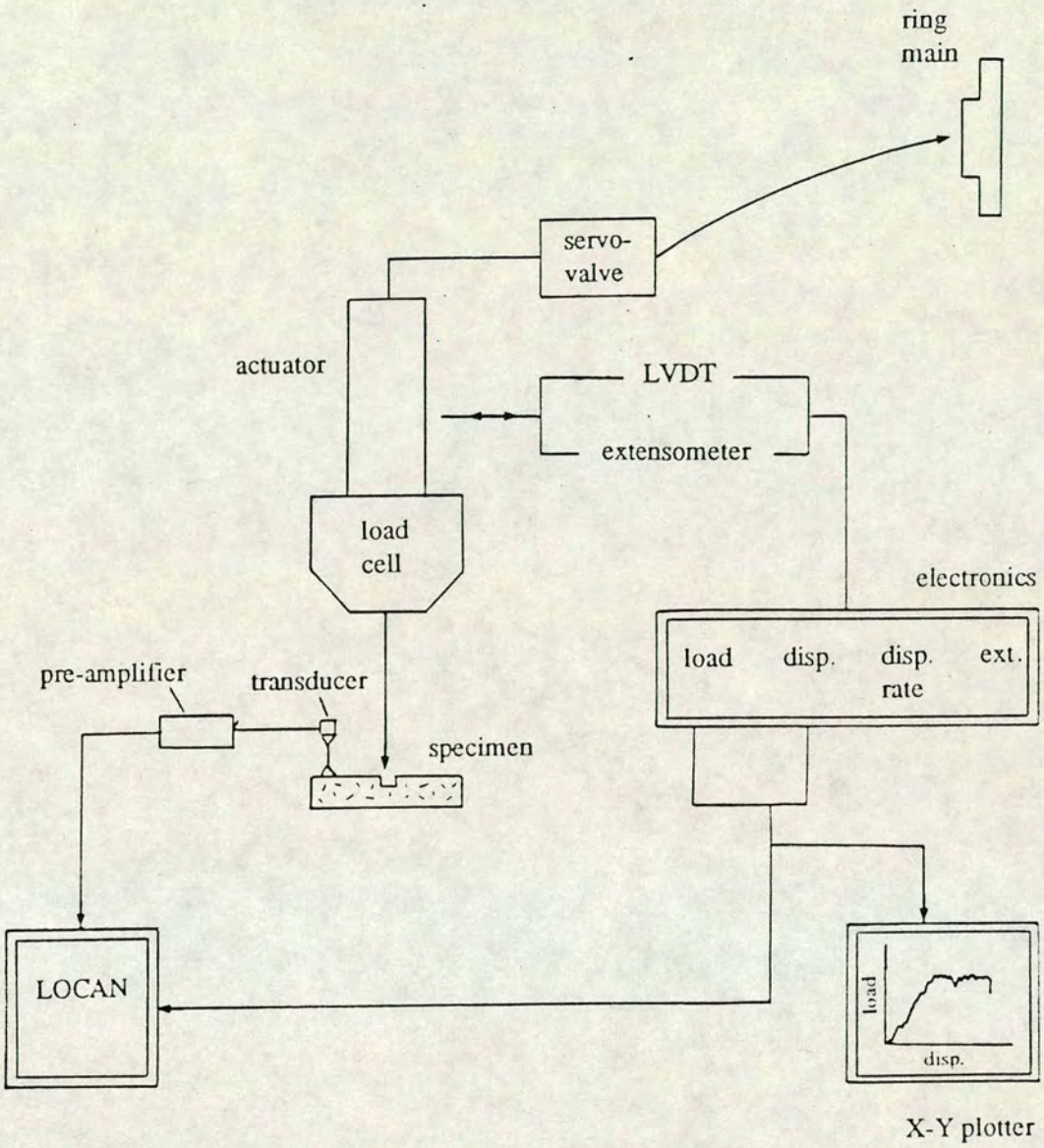

Figure 2.4 Summary diagram of the experimental set up (not to scale). Information of load, displacement, displacement rate and extension from the LVDT and extensometer is sent to and from an electronic control panel. From this, load and displacement data are sent to an X-Y plotter to produce a plot during the test, and also to the LOCAN-AT data aquisition equipment. Acoustic emissions picked up by the transducer are also sent, via a pre-amplifier, to the LOCAN-AT.

where B and C are constants that depend on the loading configuration, specimen dimensions and material properties. Figure 2.5 shows the displacement/load vs crack length results for a compliance calibration test on a double torsion specimen of microgranodiorite, as used in this experimental series. This test involves the loading of a single specimen containing a sharp starting notch of known length,a_1. Loading is stopped before microcracking begins, and the notch machined to a new length, a_2 before the specimen is loaded again. This is repeated at least four times to obtain displacement versus load data for four increasing crack lengths. The slope of this graph (figure 2.5) gives an experimentally derived value of B for the microgranodiorite of 1.1×10^{-5}.

It is useful to compare this experimentally derived value with the theoretically derived compliance (Williams and Evans, 1973):

$$k = \frac{3W_m{}^2 a}{Wd^3\mu} \qquad (2.2)$$

where μ is the shear modulus, a is the crack length and the other parameters depend on the specimen dimensions (see figure 2.1(a)). Using this formula, and an average value for the shear modulus μ of 19.5 GPa (the range of μ for granitic rocks from reference tables is 11.3 - 27.7 GPa, Lama and Vutukuri, 1978), values of B are found to be as follows; $B = 1.25 \times 10^{-5}$ for microgranodiorite; $B = 0.9 \times 10^{-5}$ for granite, within 20% of that derived by experiment.

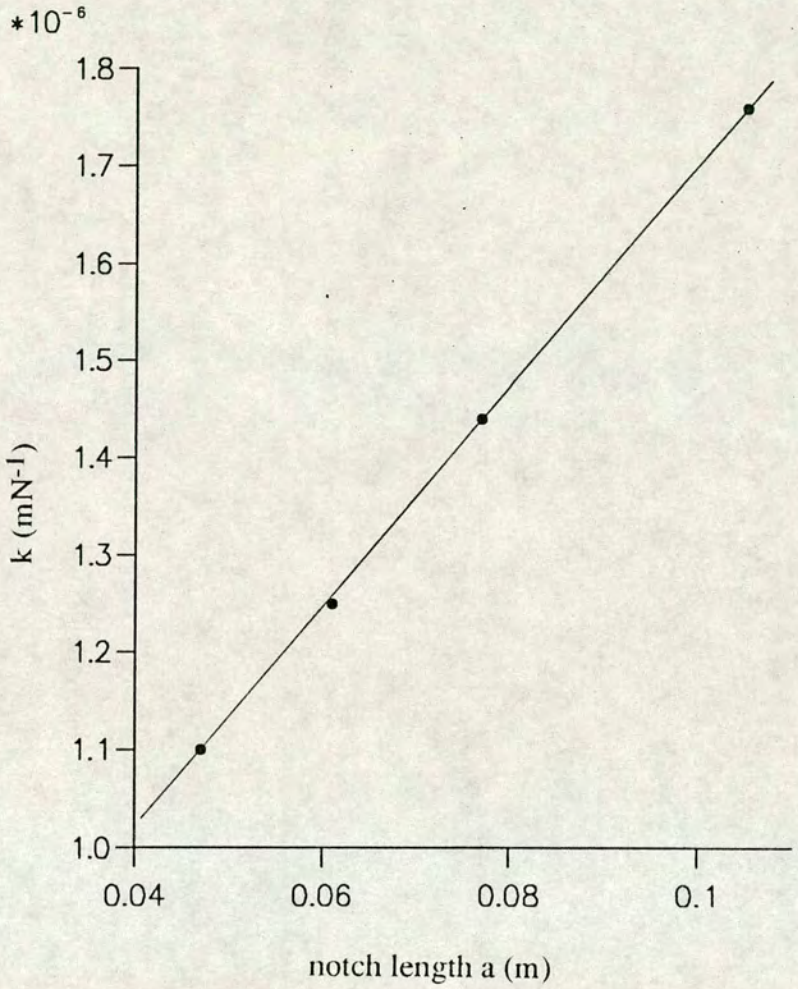

Figure 2.5 Compliance calibration diagram of compliance k (y/P) (mN^{-1}) plotted against notch (crack) length a (m). The compliance increases linearly as crack length is increased. The slope is the constant B in equation (2.1) (used in the crack velocity equation (2.5)).

2.3.2 Stress intensity factor

Constant load determination

As already mentioned, the double torsion technique chosen was the constant displacement rate method, which produces a period of constant load from the onset of macrocrack growth until failure. Figure 2.6 shows an example of a typical load vs time plot (from the 'dry' test #0101). The load is seen to increase as the specimen shows linear-elastic behaviour , until microcracking begins at (a), (this also coincides with the main onset of acoustic emission). The increasing displacement is then exactly compensated by the change in specimen compliance due to microcracking, and the load remains approximately constant during a period of stable, subcritical crack growth, until the specimen fails dynamically at (b). Some fluctuation is evident. During the period between the origin and (a), the material is showing linear-elastic behaviour , indicating that no cracking is occuring, and so the fluctuations here are due to the digital nature of the loading and load monitoring systems. A calculation of the 'standard error of goodness of fit' (see appendix C) to a regression line of the data gives a value of 35 Newtons, (note, this is not a standard error of the load). Between (a) and (b), there is additional fluctuation, indicated by a higher 'standard error of goodness of fit' value of 54 Newtons. This results from the 'start-stop-start' nature of crack growth due to material heterogeneity. For each test, a 'constant load' time period was chosen by inspection of plots such as figure 2.6, and an average load operating during this time was calculated. For those tests that ran a relatively long time (more than 2-3 minutes) the load can be logged every ten seconds and an arithmetic mean may be taken. For fast tests that lasted only 1-2 minutes, more data can be obtained using the load recorded for each AE event. In this case it is necessary to calculate a time weighted average load by weighting each load value recorded by the time

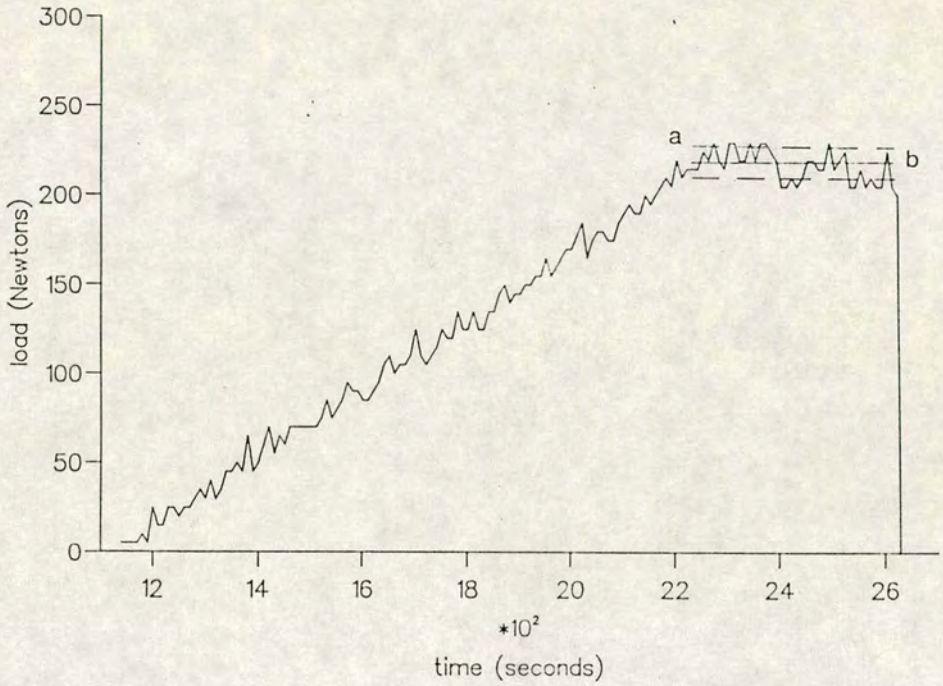

Figure 2.6 Example of a load vs time plot for a dry test run at a displacement rate of 0.16×10^{-6} ms^{-1}. The load increases as the specimen shows linear-elastic behavior, until microcracking begins at (a). This coincides with the main onset of acoustic emission. The increasing displacement is then exactly compensated by the change in specimen compliance due to cracking. The load then remains essentially constant (the straight line represents the arithmetic mean) until failure at (b). The dashed lines represent the standard deviations from the mean load, between a and b.

interval during which that load was effective (see appendix C). Typical standard deviations from the average load are of the order ±10 to 25 Newtons, with a range of constant loads of 170 - 250 Newtons.

Stress intensity calculation

One of the main advantages of the double torsion method is that the stress intensity factor K_I is directly proportional to the applied load, and so during the time period of constant load, the stress intensity is also approximately constant. Theoretically, for mode I tensile failure, the stress intensity for this loading geometry is:

$$K_I = PW_m\left[\frac{3(1+\nu)}{Wd_n d^3 b}\right]^{0.5} \qquad (2.3)$$

where P is the applied load, ν is Poisson's ratio, β is a dimensionless correction for the finite width of the specimen (Fuller, 1979) ($\beta = 1 - 0.6302t + 1.20te^{-\pi/t}$, where $t = 2d/W$) and the other parameters depend on the specimen dimensions (see figure 2.2(a)). The mathematical development to this formula is given by Williams and Evans (1973).

Fracture toughness

When comparing results from different rock types and specimen sizes, it is useful to normalize the stress intensity to a material parameter such as fracture toughness, K_{IC} (the critical K_I for dynamic failure). Fracture toughness tests were therefore carried out on specimens of Loch Uisg microgranodiorite and Ballachulish

granite using a very fast displacement rate of 1.6×10^{-4} ms^{-1} (under displacement control) to load the specimen rapidly and hence propagate a crack catastrophically to failure. The peak load was then used to calculate K_{IC}. For the microgranodiorite, K_{IC} = 2.9 MPa m$^{1/2}$; for the granite, K_{IC} = 2.0 MPa m$^{1/2}$. These results compare well with previously established mode I fracture toughness values from double torsion tests for various rock types as summarised in Atkinson and Meredith (1987b), for example, Carnmenellis granite, K_{IC} = 2.16 MPa m$^{1/2}$; Westerly granite, K_{IC} = 1.74 to 1.85 MPa m$^{1/2}$.

2.3.2 Crack velocity

As described in section 1.3, Charles' Law (1958) describes the direct relation between rupture velocity and stress intensity, which is found experimentally to be:

$$V \propto K_I^{\,n} \qquad (2.4)$$

where V is velocity and n is the subcritical crack growth index. However, the compliance calibration described earlier can also be used to calculate rupture velocity directly. Differentiating equation (2.1) with respect to time gives:

$$\frac{dy}{dt} = \dot{y} = (Ba + C)\frac{dP}{dt} + PB\left(\frac{da}{dt}\right) \qquad (2.5)$$

where $\dot{y}$ is the displacement rate, and da/dt is the rupture velocity. Using the constant displacement rate method, a region of constant load is reached and maintained for a finite period of time (see section 2.3.2), during which dP/dt = 0. Equation (2.5) then reduces to:

$$\frac{da}{dt} = V = \frac{\dot{y}}{PB} \qquad (2.6)$$

(Weiderhorn, 1973), and so the velocity may be determined directly from the load, P and displacement rate, $\dot{y}$, using the constant B already determined from the compliance calibration. Since a single constant displacement rate is used for each test, just one value of V is obtained since the crack grows at a constant velocity, corresponding to the constant K and constant load for that test. Figure 2.7 shows the rupture velocities obtained by this method plotted against the stress intensities from the present series of experiments. The dry and wet test results are plotted separately on the same log-log coordinates, each point representing a single test. Much more scatter is evident on this diagram compared to the results from load relaxation tests (figure 2.2). This may be due simply to the fact that each point is from a separate test using a different specimen, unlike the relaxation method which produces a complete K-V curve from one test. However, the constant displacement rate tests do show a similar linear trend, particularly the wet tests. From equation (2.4), it can be seen that:

$$\text{Log } V = \text{constant} + n \text{ Log } K_I \qquad (2.7)$$

and so the gradient of the log V vs log K_I graph gives the subcritical crack growth index, n. The slope of the dry tests, given by the reduced major axis on figure 2.7(a) gives $n = 16.9 \pm 4.1$ (the statistical method is given in Appendix C), whereas the slope from the wet tests, figure 2.7(b) gives n to be 29.9 ± 1.6. Note the smaller error in the curve fit of the wet data due to the smaller degree of scatter in the results. This compares well with previous experimentally derived values of n (mode I) (summarized in Atkinson and Meredith, 1987b), for example, Oshima granite in air, n = 30; Westerly granite in air, n = 36 to 39, in water, n = 34 to 53.

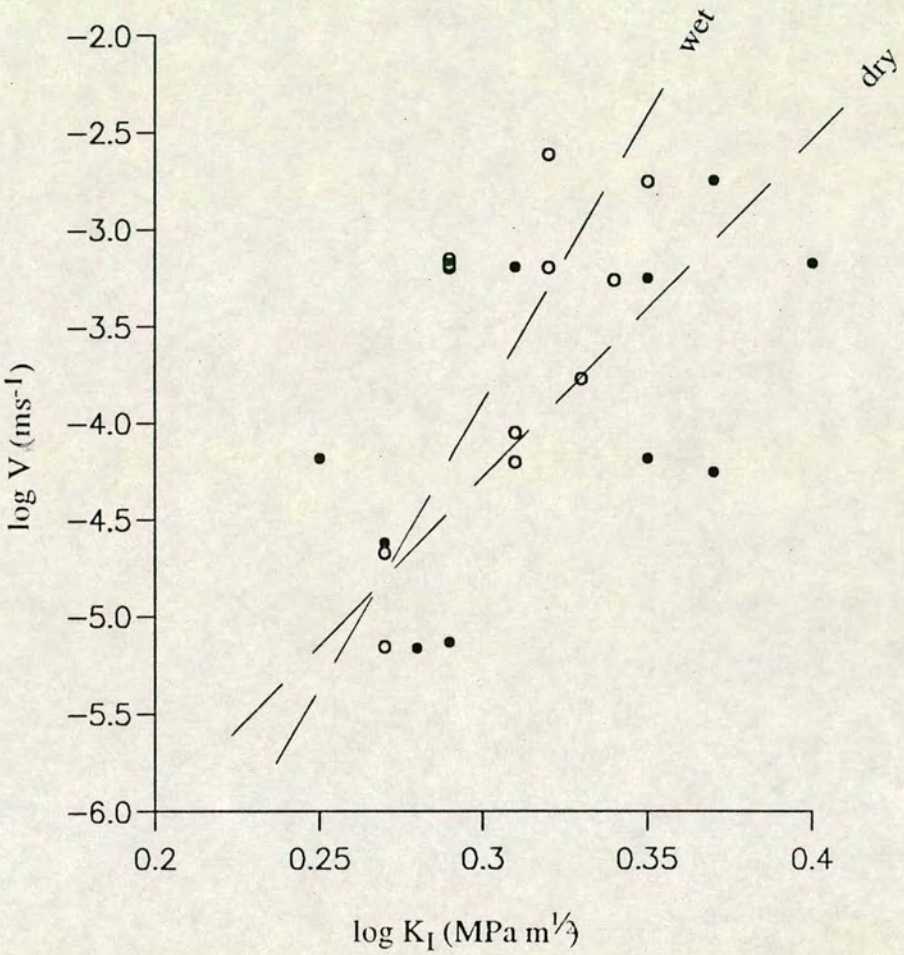

Figure 2.7 Rupture velocity as a function of stress intensity for 'dry' and 'wet' results from the present series of constant displacement rate tests on Loch Uisg microgranodiorite. Each of the points represent a single test. Solid circles - dry tests; open circles - wet tests. The curve fits (reduced major axis) to the data are discussed in the text.

2.4 Acoustic emission monitoring and procedure

During each test, the acoustic emissions from crack growth were monitored via the commercially available LOCAN-AT data aquisition equipment (Physical Acoustics Corporation). A single transducer was used, (the frequency response calibration certificate is shown in Appendix D). In future work, several transducers may be used to investigate AE source locations. A stainless steel waveguide with conical terminations was used to conduct the AE signals from the specimen to the transducer. Use of such a waveguide system has previously been shown not to affect the size distribution of AE events (Meredith and Atkinson, 1983). The conical terminations were attached to the specimen and transducer using cyano-acrelate cement (superglue) and during the 'wet' tests the attachment to the specimen was protected by waterproof grease. An artificial Neilsen Source was used to test the acoustic bonding. This gave AE signals of on average 90 dB, indicating that a good acoustic bond was obtained by this procedure. The transducer was connected, via a preamplifier set at a fixed gain of 40 dB, to channel 1 of the LOCAN-AT.

A fixed threshold was established for each test depending on the background noise level. This ranged from 29 dB to 50 dB and was largely determined by the presence or absence of water. The level of background noise increased considerably when the specimen and waveguide were immersed in water, due to waves on the water surface caused by vibrations from the servovalve that were transmitted down the loading ram to the water. Since the servo-valve is an essential component of the necessary experimental set up to obtain an accurate constant load, the only solution to this problem was to raise the threshold, thus unavoidably reducing the amount of data recorded during the wet tests. During several wet tests, the signal was passed through an active high pass filter (AHPF), cutting out all signals below 300 kHz frequency.

This was effective in reducing the background noise level slightly, thus allowing a lower threshold to be used.

The parameters recorded for each acoustic emission event were its duration, peak amplitude, threshold crossing counts and energy, as well as time of event and two parametrics - load and extension. The hit definition time, which determines the end of the hit, was set at 300 microseconds. It should be noted that although it is possible to record the waveform as well as the AE parameters with the present equipment, this slows up the recording process and much of the AE data is missed. Therefore, during this experimental series, the waveform was not recorded. The data aquisition mode of the LOCAN was started at the same time as a positive load is monitored on the ramp generator of the loading machine.

After each test, the AE seismicity produced during the time period of constant load and constant K may be quantified. All other detected AE data is discarded prior to the subsequent analysis described in the next chapter.

Chapter 3 Experimental Analysis

The experimental data collected from this series of double torsion laboratory tests may be divided into three distinct types; (1) the fracture mechanics results already discussed in Chapter 2, including the constant load determination, stress intensity factors and rupture velocities for each test; (2) the AE microseismicity data monitored during crack propagation; and (3) the structure of the macrocrack and microcrack systems produced in each specimen as a result of loading. This chapter, describing the main analysis of the experimental data, is divided into two parts, concentrating first on the analysis of the AE data, and then on the structural data. The ways in which the three types of quantitative data may be related, and an overall discussion of the experimental analysis, will then be given in Chapter 4.

3.1 Recorded seismicity during artificial microfracture

A definition of AE and details of the monitoring procedure for this experimental series have already been given in sections 1.4.5 and 2.4. This first half of the present chapter describes the nature of the AE data obtained, and the methods used to quantify this data and reduce it to a form which can be compared with the structural analysis to follow.

3.1.1 General AE analysis

For each test carried out during this study, the AE data may be analysed in three ways. First, a general idea of the AE activity during the test may be obtained by plotting a graph of event rate (the number of events recorded in a given time interval, e.g. 50 seconds) versus the applied load. More detail may then be found from analysis

of each individual event, specifically the amplitude plotted against time, showing the event size distribution in time. Once the constant load / constant K time interval has been determined (as described in section 2.3.2), the scaling properties of the AE monitored during this time period may then be quantified as an AE b-value. This will be discussed in the next subsection (3.1.2). The general nature of the microseismicity was determined by monitoring the AE during tests on both the granodiorite and granite specimens under different conditions, including 'dry' and 'wet' environments, and relatively fast and slow strain rates.

Figure 3.1 illustrates the AE data from a 'dry' test run at a loading ram displacement rate of 0.16×10^{-6} ms^{-1}, (test #0101). Figure 3.1(a) shows the relationship of applied load (solid line) with AE event rate (dashed line). The approximately constant load time interval is marked by T_1 and T_2. Within this period, the load is seen to drop slightly at around 2400 seconds (a), coincident with a significant peak in the AE event rate. This may be expected as the load responds to the specimen compliance; when the macrocrack extends by an isolated spurt of propagation, the compliance increases, AE is generated, and the load drops. This may be compared to figure 3.1(b) which shows the event rate in relation to the individual event amplitudes. As the event rate increases, the amplitudes increase until a peak amplitude of 97 dB occurs at 2434 seconds (b). This is followed by a quiet period, indicated by drop in the event rate at (c), until the AE rate increases again up to dynamic failure at (d).

In comparison, figure 3.2 illustrates the AE data from a 'wet' test run at the relatively fast displacement rate of 5.0×10^{-6} ms^{-1}, (test #0119). Figure 3.2(a) also shows a slight drop in the load corresponding to a peak in the AE event rate at 54 seconds (a). However, the peak amplitude recorded during this test occured at failure (figure 3.2(b), (b)), corresponding to a slightly smaller peak in the event rate. This

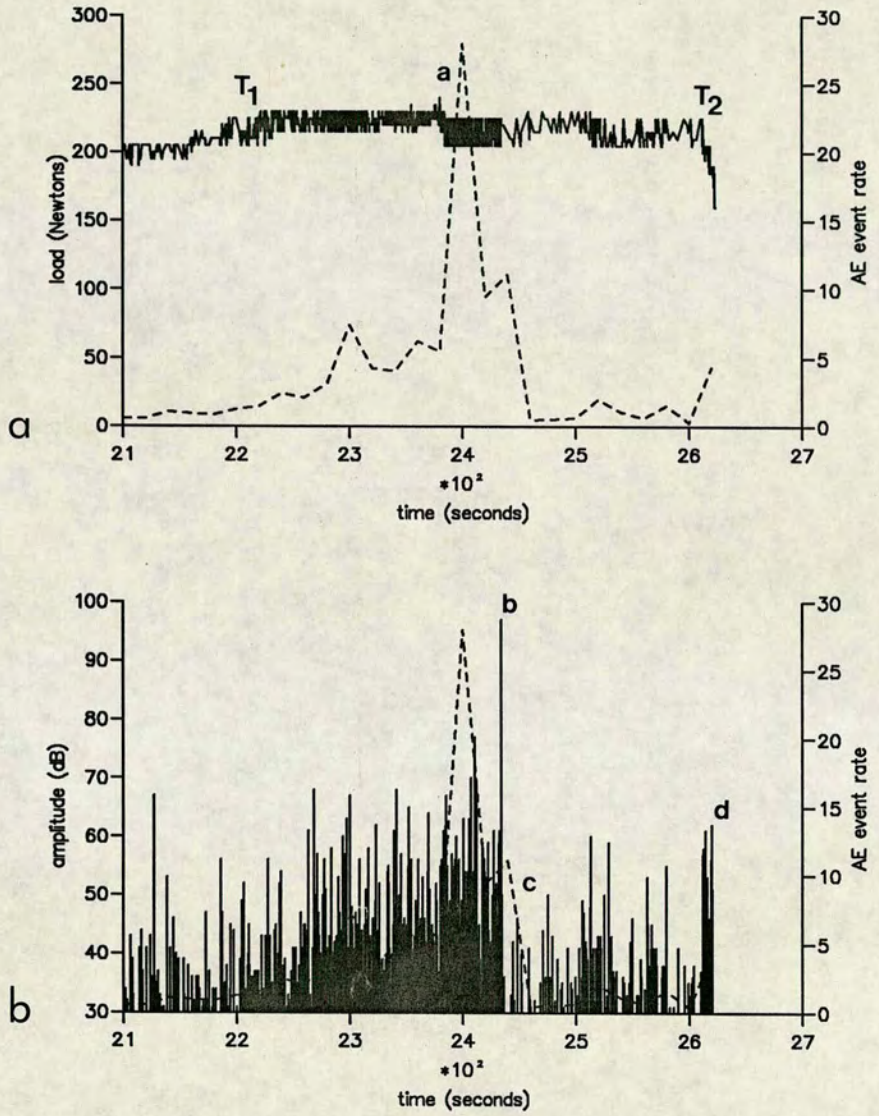

Figure 3.1 AE data monitored during 'dry' test (#0101) run at a loading ram displacement rate of 0.16 x 10^{-6} ms^{-1}. The experimental threshold set during the test was 29 dB. The AE event rates are given in events per 20 seconds.

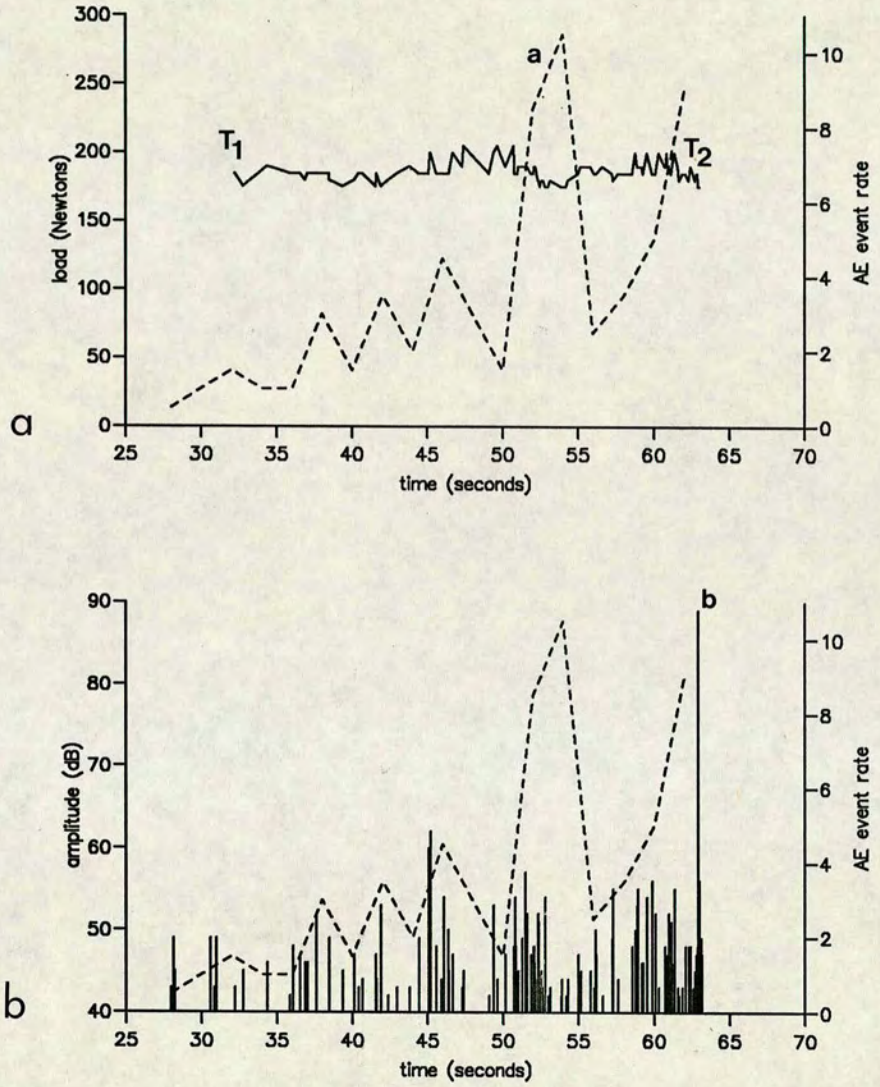

Figure 3.2 AE data monitored during 'wet' test (#0119) run at a loading ram displacement rate of 5.0×10^{-6} ms^{-1}. The experimental threshold set during the test was 41 dB. The AE event rates are given in events per 2 seconds.

suggests that the crack propagation was more uniform throughout the wet test, with a larger number of smaller crack growth increments, and less distinct 'stop-start' growth.

These trends are also illustrated in figures 3.3 and 3.4 in AE data from 'dry' and 'wet' tests (respectively) run at the slower displacement rate of 0.016×10^{-6} ms^{-1}. Figure 3.3(a) (from the 'dry' test #0022) shows a slight drop in load coincident with the peak event rate at 9850 seconds (a) well before failure, and a relatively high amplitude event of 70 dB. However, a peak amplitude of 71 dB also occured at 8447 seconds where the event rate was still very low (figure 3.3(b), (b)). Since the amplitude is a measure of the size of the event, this suggests that the crack experienced a single large increment of growth at this point.

Figure 3.4 (a and b) shows the AE data from a wet test (#0051) illustrating a relatively constant load, constant AE event rate and fairly constant low-medium amplitudes (up to 60 dB) until dynamic failure at 9920 seconds (a). It may be inferred from this that the subcritical crack growth is very stable in this example, with no significant large events before failure.

3.1.2 The AE b-value

Since the main advantage of the constant displacement rate mode of double torsion testing is the constant load / constant stress intensity conditions that the specimen is subjected to during much of the test, it would be useful to use a quantitative measurement of the AE that represents the total microseismicity monitored during this time period. The magnitude-frequency distribution of natural earthquakes and the empirical Gutenberg-Richter relation (equation 1.11), introducing the seismic b-value, may be adapted and applied to AE seismicity after a

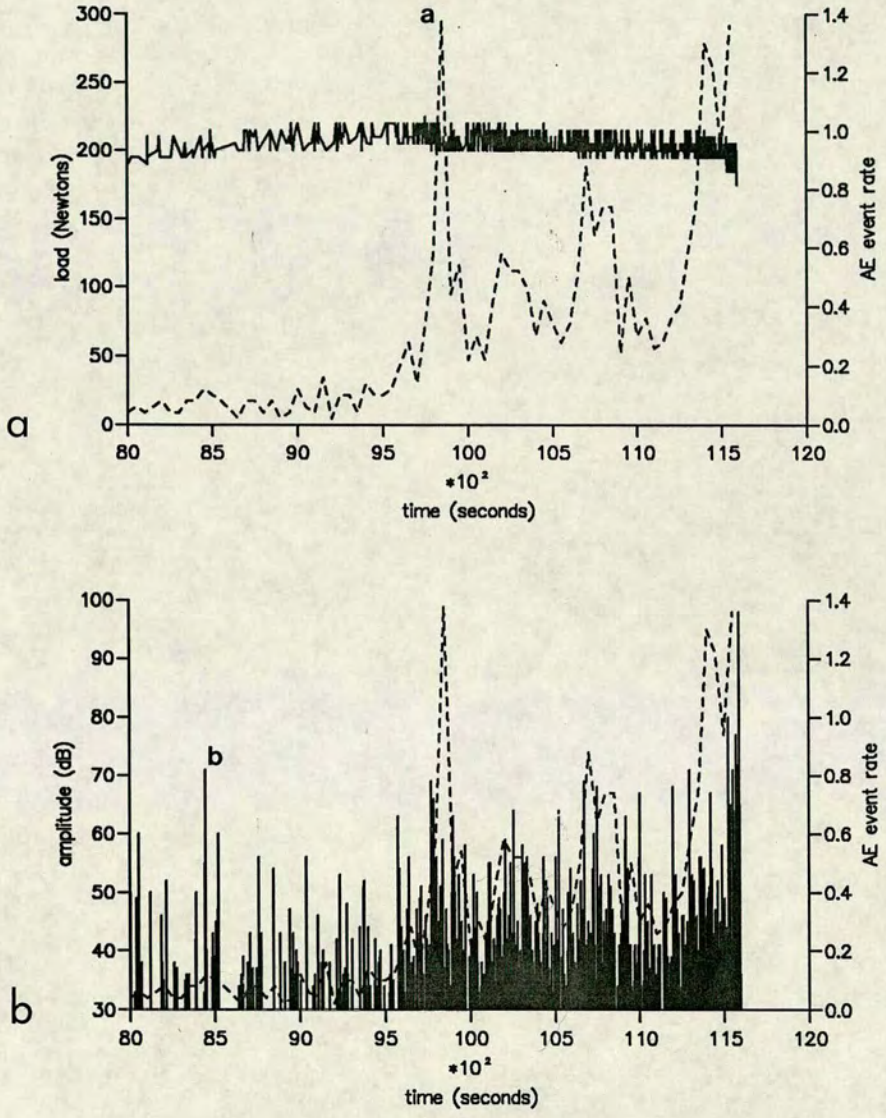

Figure 3.3 AE data monitored during 'dry' test (#0022) run at a loading ram displacement rate of 0.016 x 10^{-6} ms^{-1}. The experimental threshold set during the test was 31 dB. The AE event rates are given in events per 50 seconds.

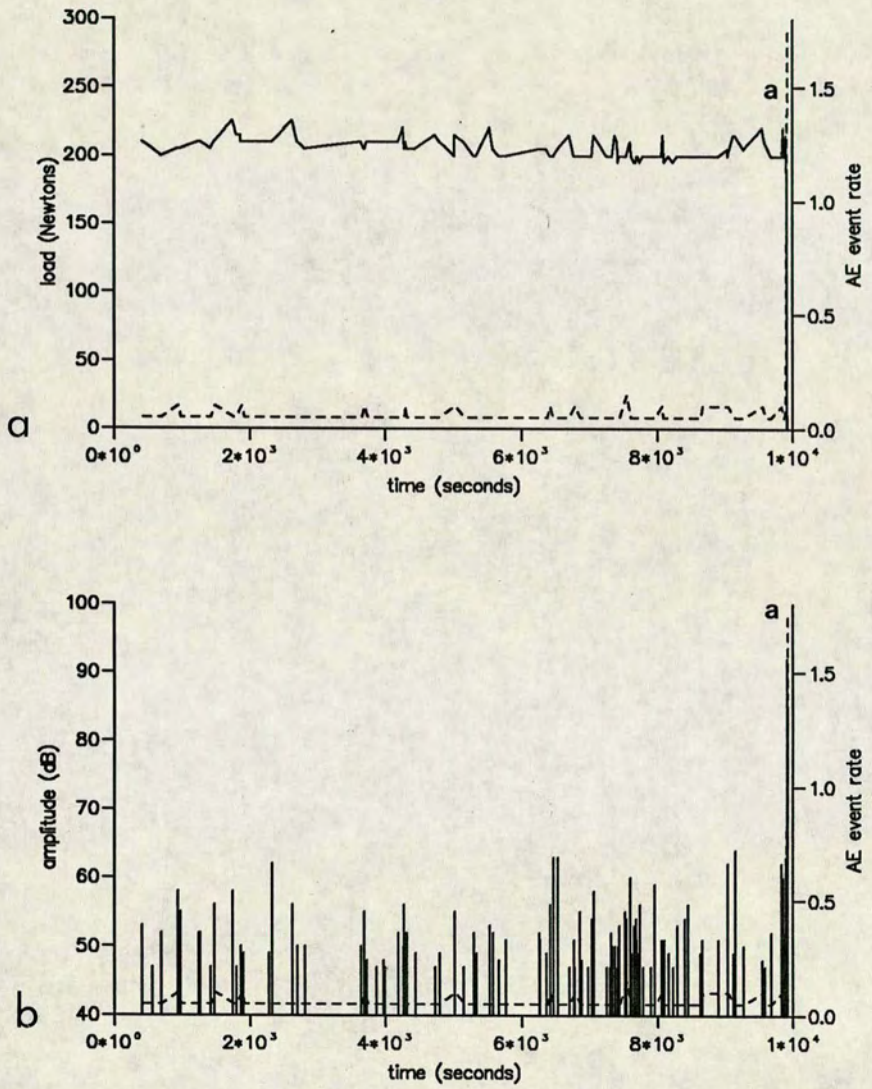

Figure 3.4 AE data monitored during 'wet' test (#0051) run at a loading ram displacement rate of 0.016 x 10^{-6} ms^{-1}. The experimental threshold set during the test was 45 dB. The AE event rates are given in events per 20 seconds.

correction factor of 20 is used to convert the dB amplitude scale to magnitude units (see section 1.4.5). Consequently, an AE b-value may be found from the amplitude-frequency relation (equation 1.18).

Figure 3.5 shows two amplitude-frequency distributions (including both discrete and cumulative) from one 'dry' and one 'wet' test that were both run at the same slow displacement rate of 0.016×10^{-6} ms^{-1}. Therefore, the controlling variable is the presence or absence of water. Both plots illustrate the log-linear relationship of this distribution. The discrete data of figure 3.5(a), from the dry test (#0022), has a negative slope of 1.08 ± 0.04 (calculated by the reduced major axis method, see Appendix C). In comparison, figure 3.5(b) is from the wet test (#0051) and has a higher slope of 1.49 ± 0.17 determined from the discrete data. (Note that in both cases the slope is higher for the cumulative data due to the 'roll-off' effect at high magnitudes described in section 1.4.1). Thus the effect of the fluid presence is to produce a greater relative proportion of smaller seismic sources. This figure also illustrates the difference in the amount of data recorded during the tests due to the different threshold settings required once the specimen and waveguide were immersed in water. During the 'dry' test (#0022, figure 3.5(a)), a fixed threshold of 31dB was used, and a total number of 626 AE events were recorded during the time interval of constant load. The 'wet' test (#0051, figure 3.5(b)), required a higher threshold of 45dB to cut out background noise, and hence only 111 AE events were recorded.

The maximum likelihood method

The reduced major axis technique described in Appendix C and applied for illustrative purposes to figure 3.5 is essentially a least squares method. This gives equal weight to each amplitude bin, even though the smaller amplitude bins contain

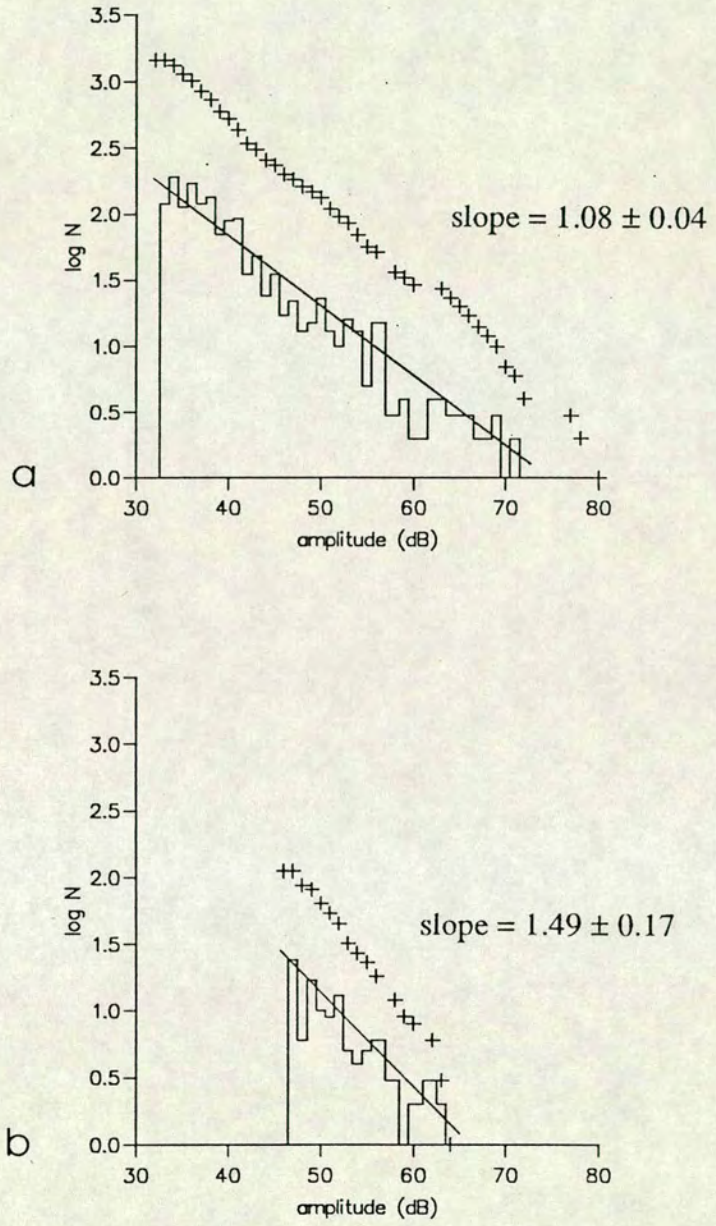

Figure 3.5 AE amplitude-frequency distributions. Staircase - discrete data; crosses - cumulative data.

a. 'dry' test (#0022). Slope = 1.08 ± 0.04 (reduced major axis).

b. 'wet' test (#0051). Slope = 1.49 ± 0.17 (reduced major axis).

more events and hence are statistically more accurate. In contrast, the maximum likelihood method (Aki 1965) assigns an equal weighting to each recorded event, and reduces to the formula:

$$b = \frac{20 \log_{10} e}{\bar{a} - a_c} \qquad (3.1)$$

where b is the AE b-value, $\bar{a}$ is the mean amplitude in dB and a_c is the lower amplitude cutoff used in the calculation. In practice, a_c must be slightly greater than the preset threshold amplitude set during the experiment, since this electronic threshold represents a gradual rather than a sudden cut-off in reality. The error for this method at the 90% confidence level is:

$$\sigma_b = \frac{1.96b}{\sqrt{N}} \qquad (3.2)$$

and so the errors involved depend directly on the number of events recorded and used in the b-value calculation. As the wet tests required a higher threshold and higher amplitude cut off due to increased background noise, the number of events recorded was much less (as illustrated in figure 3.5), and so the errors in b were correspondingly higher than for the dry tests. It should be noted that due to these difficulties, two different threshold values were used in calculating the b-values for the wet and dry tests (dry, a_c = 37.5 dB; wet, a_c = 48.5 dB) rather than using the higher value of a_c for all the tests, thus reducing the error on dry test b-values. This represents a sensible balance between remaining as systematic as possible for each test type, whilst making use of the maximum possible amount of data recorded.

Figure 3.6 shows a plot of AE b-value versus the logarithm of the number of events N used to calculate the b-value (by the maximum likelihood method). It is evident that the 'dry' tests with high N have low b-values, whereas the 'wet' tests with low N have high b-values. This is a secondary effect.

The AE b-values calculated for the data from the present experimental series ranged from 1.0 for the dry tests run at high stress intensity to 2.3 for the tests carried out at low stress intensity or higher fluid content. Full details of all the experimental conditions and results are given in Appendix B.

3.2 Structural analysis of artificial microfracture

The main advantage of the double torsion test is that the specimen geometry is ideal for inspection of the open tensile microfracture system produced. This section of the chapter describes the methods used to examine the structure and the various ways in which the geometry of the fracture patterns was quantified.

3.2.1 Method and qualitative structural analysis

After each experiment, a U-V sensitive dye penetrant (Zyglo) was applied to the polished undersurface of the specimen to enhance the visibility of the microfractures around the main macrocrack. The undersurface of the central third of the specimen, representing the part which fails in pure mode I fracture at constant stress intensity, was then photographed using a photomicroscope. It was not necessary to use a U-V light throughout the photography as the dye penetrant that had entered the cracks in the specimen showed up very well as a bright yellow substance even under ordinary light reflected at a low angle. The fracture patterns were then traced onto paper. Figure 3.7 shows two photographs and overlay tracings from different test

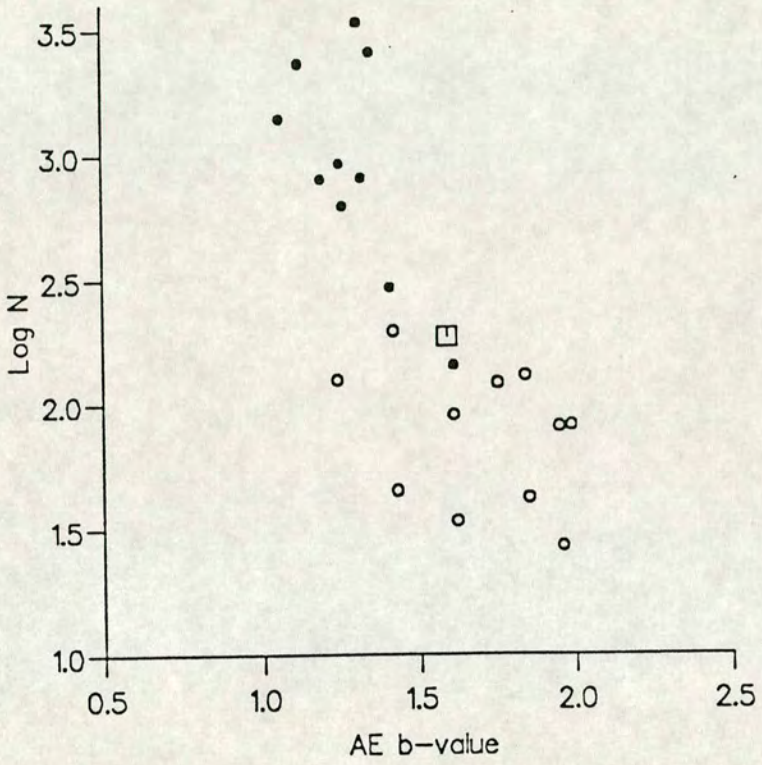

Figure 3.6 Plot of AE b-value (maximum likelihood) versus log N, the number of events used to calculate the b-value.

● 'dry' test results

□ 'damp' test result

○ 'wet' test results

Figure 3.7 Photomicrographs of parts of two granodiorite specimens. The main crack is marked in blue. The centre line of the specimen is marked by the dashed black line. The scale marked is 5 mm. The large arrows indicate the direction of tensile stress; the small arrows indicate the direction of fracture propagation. The squares mark the areas of enlargement shown in figures 3.8 and 3.9.

a. 'dry' test #0022.

b. 'wet' test #0051.

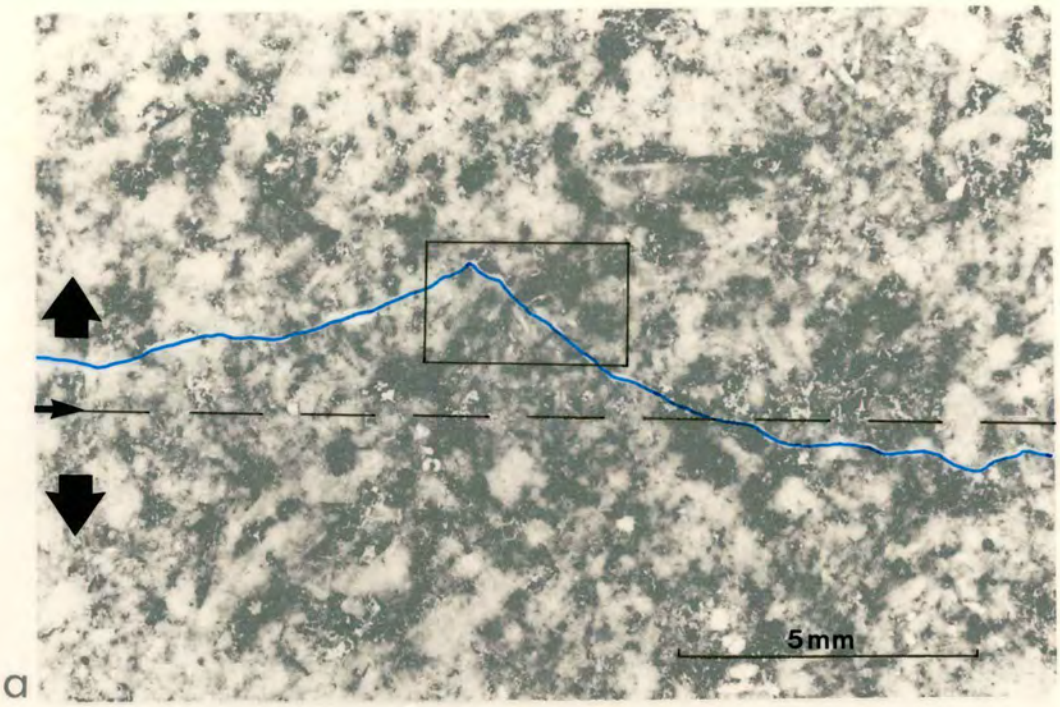

a

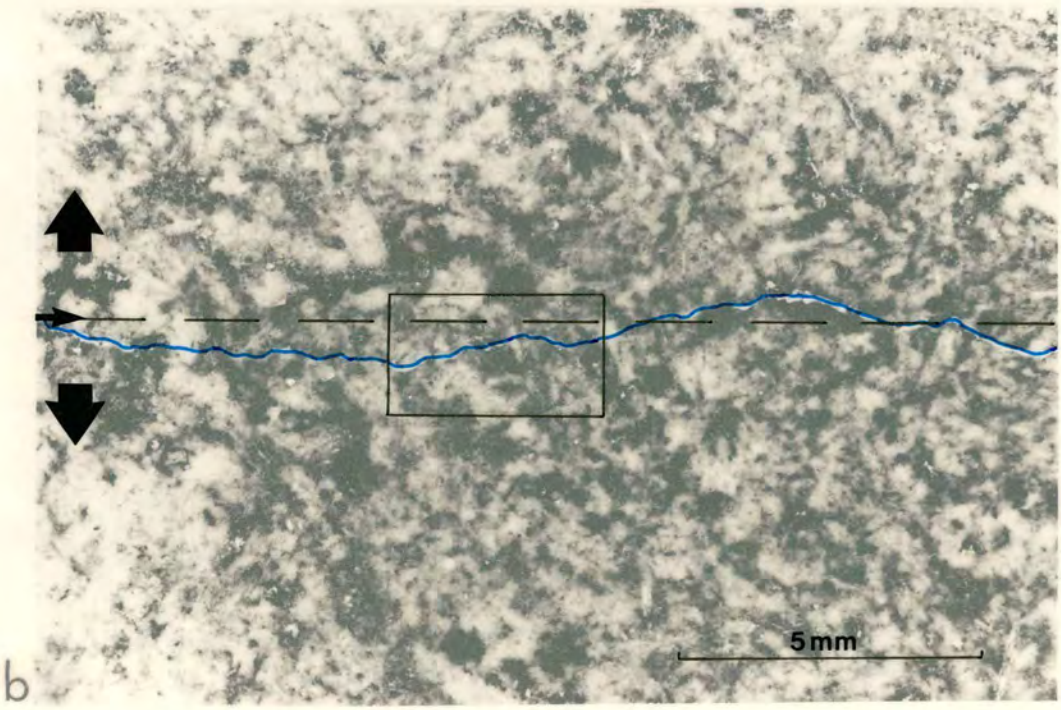

b

specimens at a magnification of x63, representing approximately 15 mm along the centre of the specimen. The tensile load was applied in the direction of the large arrows. Crack propagation is from left to right (shown by the smaller arrow). The main crack, where the specimen broke in two, is marked in blue and may be compared to the centre line of the specimen (dashed black line). Both tests were carried out at the same slow displacement rate, hence the controlling variable in this comparison is the presence or absence of fluid.

Figure 3.7(a) is from a test run at a relatively slow displacement rate of 0.016 x 10^{-6} ms^{-1} in air dry conditions (test #0022). The AE data monitored during the same test is described earlier in section 3.1.1 (figure 3.3). The main macrocrack diverges significantly from the centre line, and comprises relatively straight and transgranular segments with abrupt angular breaks, between the segments, producing a 'jagged' appearance at this scale. This is a general feature of the specimens that were tested 'dry'. This may be compared to the SEM photograph (figure 1.8(a)) of a 'dry' fracture surface at much higher magnification, (Meredith and Atkinson 1983, Main et al., 1990). At the smaller scale, the transgranular nature of the fracture gives a much smoother appearance. This may suggest that the system is not strictly scale invariant over the whole length scale. The higher magnification is reflecting the structure within a single grain, whereas the roughness at lower magnification is due to the angular breaks on a scale of several grains.

This may be contrasted with figure 3.7(b) which is typical of the specimens broken in water (test #0051), The AE data for the same test is shown in figure 3.4. This test was run at the same displacement rate as the example in figure 3.7(a), but it can be seen here that the main crack is much less angular and more irregular due to intergranular cracking. However, the main crack follows a more regular path on a large scale, approximately along the centre line of the specimen. This may also be

compared to the observations of stress corrosion cracking, illustrated in figure 1.8(b), (Meredith and Atkinson 1983; Main et al., 1990). At higher magnification, the crack surface is very rough due to stress corrosion reactions and propagation of the crack around the weaker grain boundaries where fluid can easily penetrate. This is reflected in the irregular nature of the main crack (figure 3.7(b)). However, stress corrosion facilitates propagation of the main crack along the preferentially weakened centre of the specimen.

Although the main crack is evident at this magnification, only a few large subsidiary cracks are visible. To produce a fracture pattern of the smaller scale microcracking, a larger magnification is necessary. The granodiorite specimens required a magnification of x640 and a collage of six to eight photographs to represent a total section of 1.5 to 2 mm along the main crack.

Figure 3.8 shows an example of part of the fracture pattern traced from the specimen illustrated in figure 3.7(a). The direction of crack propagation is from left to right, and again the main crack is marked in blue. The apparent opening displacement of the main crack is artificial and arises from irregularities in the two crack surfaces resulting in an imperfect fit when the two halves of the specimen are reunited. The associated microcracks are marked in black. It should be noted that a difficulty often exists in distinguishing a microcrack from a grain boundary (as discussed in section 1.3.3) where a distinct break is not evident. Most of the microcracks marked on the tracing can be observed clearly on the photograph. The presence of dye penetrant was used to establish the existence of grain boundary cracks. This section of the fracture pattern shows a distinct angular break, or 'jog', in the main crack. Most of the subsidiary microcracking seems to be concentrated in a zone ahead of the jog point. The orientations of the microcracks in this fracture pattern are plotted as a rose diagram, where north (000°) represents the centre line of the specimen. In 148

Figure 3.8 Part of the fracture pattern traced from the 'dry' granodiorite specimen illustrated in figure 3.7(a), (test #0022). The arrow indicates the direction of macrocrack propagation. The subsidiary microcracks are marked in black. The rose diagram is a plot of microcrack orientations measured using N (000°) as the centre line of the specimen.


0°
main crack
0.5 mm

microcracks measured on this section, the mean direction was 058°. Although this deviates significantly from the centre line (which is perpendicular to the tensile stress), the main crack in this section of the specimen has a trend of 045°. Therefore, the microcrack orientations illustrate the local influence of the macrocrack on the growth of the associated microcracks.

In comparison, figure 3.9 shows part of the fracture pattern traced from the 'wet' test specimen illustrated in figure 3.7(b). Here, the structure appears to be characterised by a number of bifurcation points branching off the main crack. This results in more widespread damage and a greater number of smaller microcracks associated with the main macrocrack. The microcrack orientations show a mean direction of 016° (number of cracks measured is 175). This is much closer to the orientation of the centre line. This reflects the path of the main crack approximately along the centre of the specimen, and crack opening perpendicular to the applied tensile stress.

In both figures (3.8 and 3.9), the presence of linear trails of microcrack growth in several directions suggests that the macrocrack may have had a choice of path, before dominant failure along one direction. This has also been shown in previous experimental work on alumina, where in-situ observation of tensile fracture propagation has shown that the final fracture often avoids the previously formed apparent fracture paths (Swanson, 1987).

The granite specimens required a smaller magnification, due to the larger grain size of the rock. Figure 3.10 shows two fracture patterns from different test specimens at a magnification of x63 representing 15 mm along the centre of the specimens. Both the main crack (blue) and subsidiary microcracking (black) are evident at this scale, (comparing this figure to figure 3.7 illustrates clearly the

Figure 3.9 Part of the fracture pattern traced from the 'wet' granodiorite specimen illustrated in figure 3.8(b), (test #0051). The arrow indicates the direction of macrocrack propagation. The subsidiary microcracks are marked in black. The rose diagram is a plot of microcrack orientations measured using N (000°) as the centre line of the specimen.

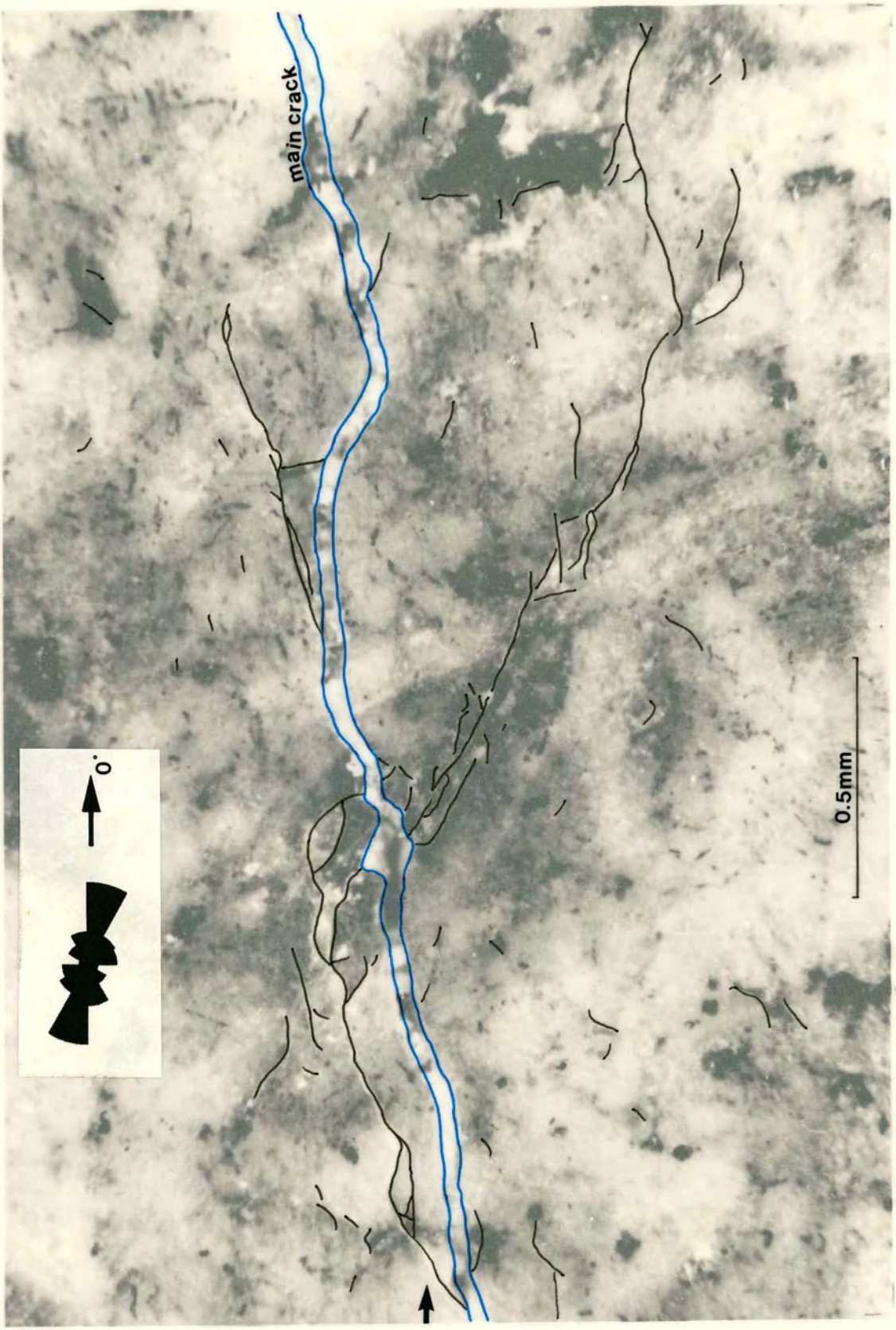
main crack
0°
0.5mm

Figure 3.10 Two fracture patterns traced from granite specimens. Notation as for figures 3.7 to 3.9.

a. 'dry' test #0128.

b. 'wet' test #0126.

a

b

difference in scale and grain size between the granodiorite and granite specimens).

Figure 3.10(a) is part of the fracture pattern traced from a 'dry' specimen that was broken at a relatively fast displacement rate of 5×10^{-6} ms^{-1} (test #0128). This may be compared to figures 3.7(a) and 3.8 of the 'dry' granodiorite specimen. The main crack again comprises relatively straight segments with angular breaks between the segments. The transgranular nature of the main crack is very well illustrated by the large biotite crystal, just left of centre, that is broken by the macrocrack. The microcracks in these specimens must be carefully distinguished from the coarse grain boundaries, either by the presence of dye penetrant or a lack of colour change across the lineament (indicating fracture across a single grain).

In contrast, figure 3.10(b) shows part of the fracture pattern from a 'wet' test granite specimen that was broken at a displacement rate of 1.6×10^{-6} ms^{-1} (test #0126). This contains a main crack similar in appearance to that in figures 3.7(b) and 3.9 (at a different scale), which is less angular and more irregular than in the 'dry' specimen, and also has more smaller related fractures.

In summary, the fracture patterns from 'dry' and 'wet' test specimens illustrate differences in the nature of both the main macrocrack and the subsidiary microcrack arrays. Therefore, the qualitative descriptions of the fracture geometries appear to confirm the importance of fluid presence on the structure. These characteristics are also evident at different scales in both the small granodiorite specimens and larger granite specimens, although possible differences in fractal scaling above and below the grain size have been highlighted.

The process zone

As described in section 1.3.2, a process zone of microcracking ahead of the macrocrack has been suggested as an important component of the crack propagation process. To investigate this possibility, several of the tests were stopped before dynamic failure, but after significant microcrack growth (indicated from AE activity) had occurred. Thus the specimen remained intact, but contained a macrocrack extending into the middle third region of the specimen. Figure 3.11 shows two examples of fracture patterns from the crack tip area from two granodiorite specimens. In both photographs, the arrow indicates the main macrocrack that is continuous in the specimen until it enters the photographed region. There are no more microcracks present in the specimens from the right-hand edge of the photographs onwards. Figure 3.11(a) is taken from a specimen tested in air at a displacement rate of 1.6×10^{-6} ms^{-1} (test #0055). This test was stopped after 325 seconds of loading. This tracing shows a number of small cracks ahead of the main crack, but no regular intense zone of microcracking at the crack tip. The isolated microcracks seem to occur in a relatively narrow band with respect to the main macrocrack. Figure 3.11(b) is from a wet test run at the same displacement rate (test #0048) and stopped after 316 seconds of loading. This fracture pattern also contains microcracks ahead of the main crack, in a slightly narrower zone than those in figure 3.11(a), but again there is no regular zone of intense damage at the crack tip. The microcracks appear to trace out two possible paths that the macrocrack may have taken if loading had continued. This indicates that the presence of water may have an influence on the formation of microcracks ahead of the propagating macrocrack. Stress corrosion may facilitate microcrack growth in a path directly ahead of the main crack in a direction perpendicular to the tensile stress.

Figure 3.11 Two fracture patterns traced from the crack tip region of granodiorite specimens from tests that were stopped before dynamic failure. The arrow indicates the direction of macrocrack propagation.

a. 'dry' test #0055.

b. 'wet' test #0048.

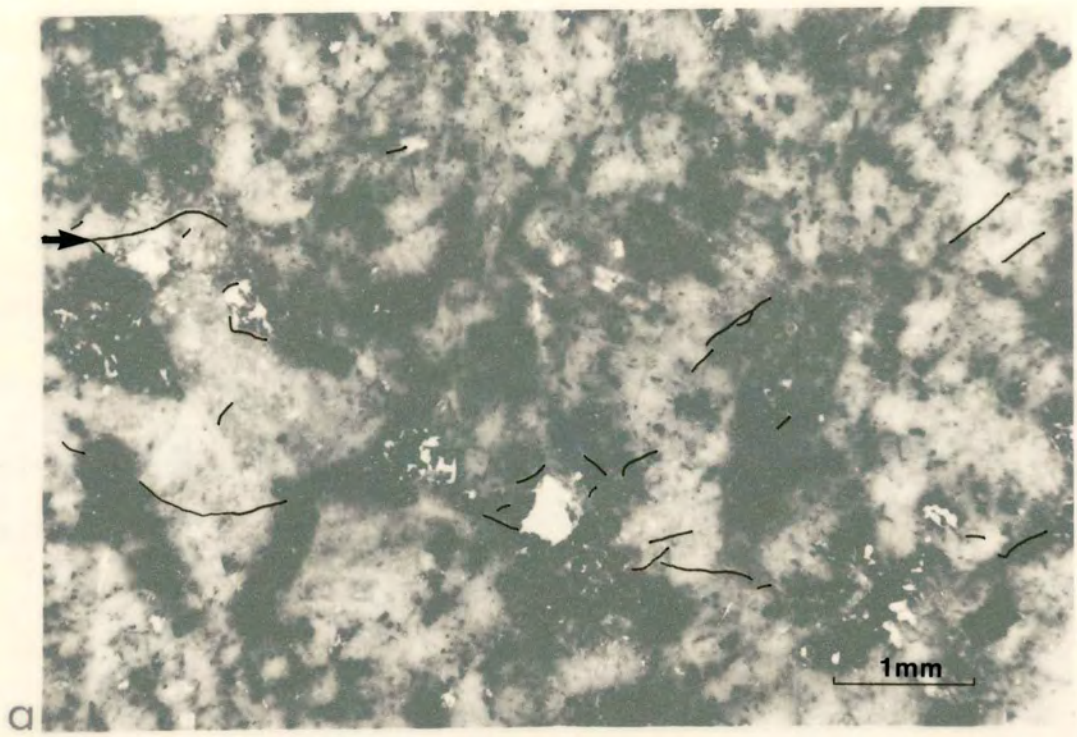

a

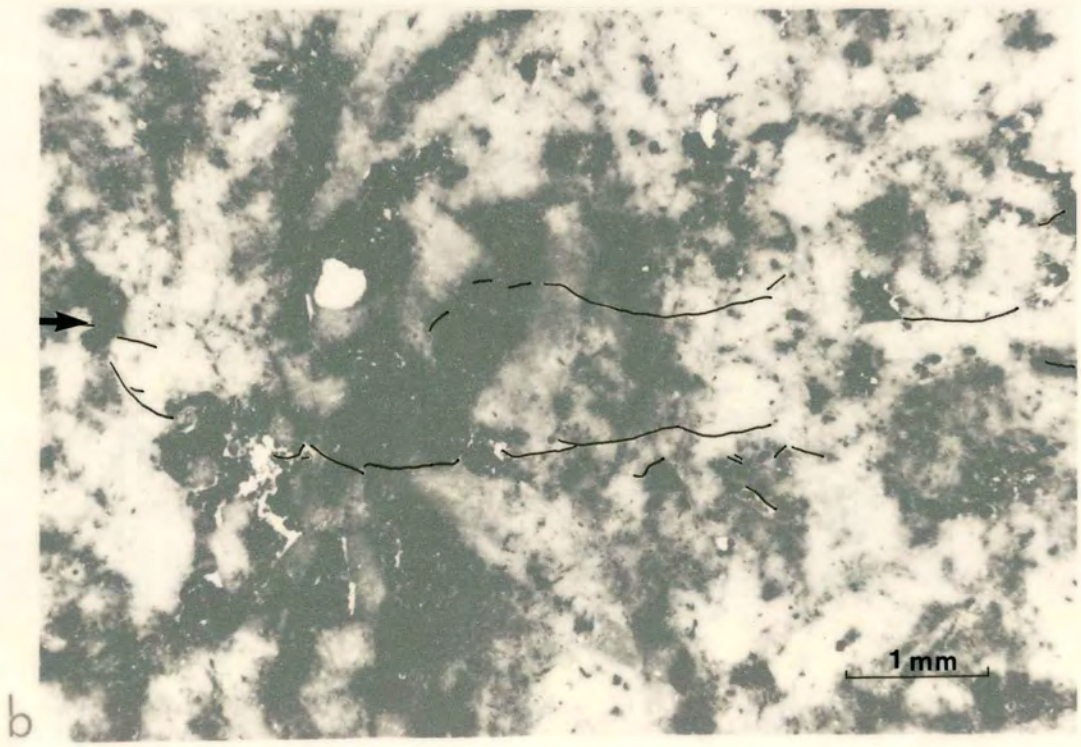

b

The fracture patterns from the tests that were stopped before failure, illustrated in figure 3.11, suggest that a type of process zone mechanism is acting in the brittle crystalline material. Isolated microcracks appear to form ahead of the main crack at some distance, possibly in response to the effect of longer range interactions on the microstructure of the crystal grains. The macrocrack may then propagate into certain microcracks, leaving the remaining microcracks as remnant damage. It is probable that much of the damage adjacent to the macrocrack in the double torsion specimens is due to microcrack growth ahead of the main crack, since the stresses to either side of the macrocrack are relaxed once the material has fractured.

The limited experimental time did not allow for any of the tests on granite to be stopped before dynamic failure of the specimen. However, several granite specimens remained intact after failure, due to the greater specimen thickness. Figure 3.12 shows part of a fracture pattern from specimen #0125 that was tested in wet conditions (at a displacement rate of 0.5×10^{-6} ms^{-1}). The macrocrack propagated into a large crystal of biotite, (since the crystal surface is normal to the crack propagation direction, the macrocrack could not easily meander around the grain), and appears to have attempted unsuccessfully to cross the crystal grain. In three-dimensions, it is probable that the macrocrack is continuous. However, in this two-dimensional section, en echelon tension cracks have formed, creating a damage zone, before the macrocrack continues to propagate from a weakness at the edge of the crystal. Although, this is not firm evidence for damage ahead of the propagating crack tip, it does give an insight into the processes that may occur as the crack propagates through the specimen.

Figure 3.12 Photograph of part of the main crack from a 'wet' granite specimen (#0125). The arrow indicates the direction of macrocrack propagation.


1mm

3.2.2 Quantitative analysis of structure: determination of fractal dimensions

The importance of quantifying both the seismicity of AE and the structure of microfractures from the double torsion test specimens has already been emphasised in Chapter 1. The fracture patterns produced in the specimens tested in this experimental series, as discussed in the previous section, are ideal to allow fractal analysis of the microcrack system, and hence a direct comparison with the microseismicity data recorded during the tests. Thus, for the first time the hypothesis of the relationship between the power-law exponent, D and the AE b-value can be tested by direct observation.

As described in section 1.2, there are several methods that may be used to measure several different fractal dimensions, each of which measures a different aspect of the spatial nature or size distribution of the system. The methods that were considered for application to the double torsion fracture patterns are described below. Due to the scale of the microfractures in relation to the specimen size, each fracture pattern represents only a small part of each whole specimen. However, the amount of time involved in producing each fracture pattern and the subsequent analysis was quite extensive (approximately eight hours per specimen). Therefore, to allow examination of a large number of test specimens in a reasonable time scale, only one representative fracture pattern was taken as a typical example from each specimen. The validity of this sampling procedure is described in Appendix E.

It should be noted that the structural data determined by the analysis of the visible cracks on the polished undersurface of the specimen is from a 2-dimensional slice, whereas the inferred fractal dimension from the b-value is appropriate for the full 3-dimensional crack system in the volume. As mentioned in section 1.2, this is an important consideration if the structure from the test specimen is to be related to the

AE seismicity using equation (1.19). In the following subsections, all dimensions are areal. A possible inferred relation between these two-dimensional measurements and the distribution of microcracks in the volume is discussed further in section 4.3.

Classic determination of a fractal dimension

To obtain a Hausdorff-Besicovitch dimension, D_H, from the fracture patterns, it is possible to measure the roughness of the main macrocrack using the 'yardstick' method, illustrated in figure 1.2(a). Using a pair of dividers set at a known opening r, the length of the main crack, L(r), is measured as r multiplied by the number of yardstick increments required to step along the crack trace.

Figure 3.13 shows two log-log plots of measured length versus r for the two fracture patterns of figures 3.8 and 3.9. The slope is equal to $(1 - D_H)$. Figure 3.13(a) illustrates the roughness of the fracture pattern from the air dry test (#0022). This gives a slope of -0.059, and fractal dimension $D_H = 1.06 \pm 0.008$. Figure 3.13(b) shows the roughness data from the fracture pattern of the wet specimen (test #0051), giving a slope of -0.03, and $D_H = 1.03 \pm 0.004$. Both dimensions are slightly higher than the topological dimension $D_T = 1$, consistant with a fractal set. The fractal dimension of the dry fracture system is slightly higher than that of the wet fracture system. This is reflecting the 'jaggedness' of the main crack on a scale of several grains, as described in section 3.2.1, rather than a rougher microstructure at the sub-granular scale. At smaller scales, it may be postulated that the fracture patterns from the wet tests would produce a higher fractal dimension due to the roughness of the grain boundary and intergranular stress corrosion assisted fracture. This possibility is illustrated in figure 3.14. Eventually at lower scales, the measured length may be expected to level out again at a lower fractal limit.

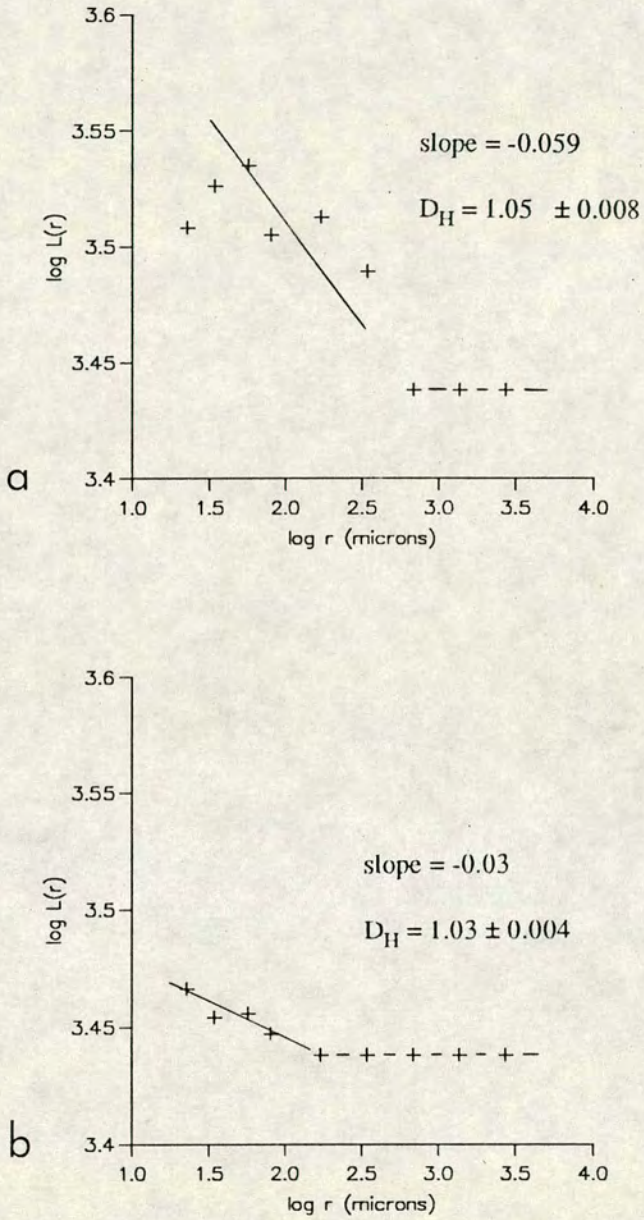

Figure 3.13 The length of the main crack L(r), in microns, as a function of divider (yardstick) length r, in microns.

a. Data measured from the main macrocrack of the 'dry' fracture pattern illustrated in figure 3.8, (test #0022).

b. Data measured from the main macrocrack of the 'wet' fracture pattern illustrated in figure 3.9, (test #0051).

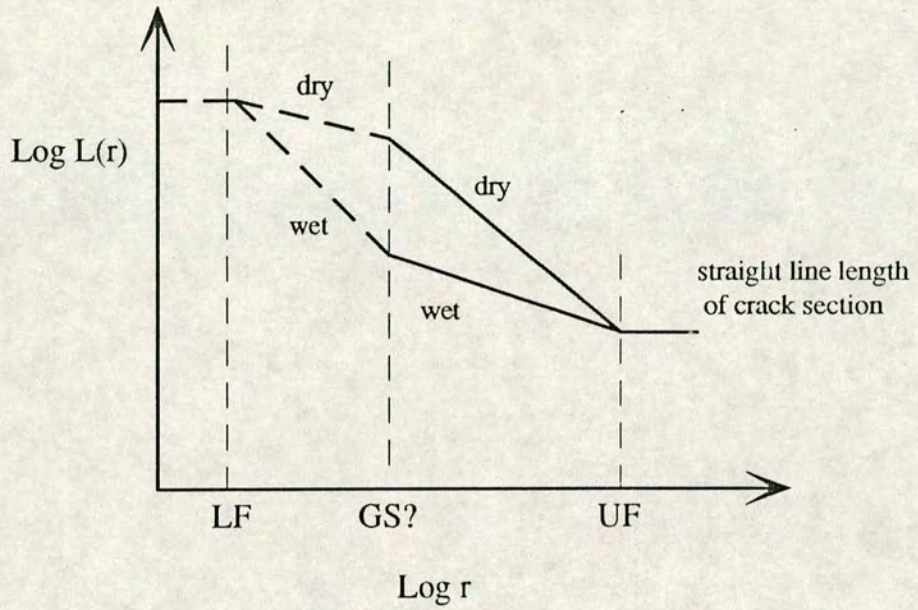

Figure 3.14 Idealised plot of length L(r) as a function of r. The dashed lines are postulated. UF - the upper fractal limit; LF - the lower fractal limit; GS - grain scale.

However, this study is predominantly concerned with the nature and geometry of the system of subsidiary microcracks around the main crack, and so an alternative method to quantify the whole fracture system was necessary.

The box-counting method

The box counting method described in Chapter 1 was applied to several square areas (of 1328 by 1328 microns) from the fracture patterns traced for each specimen. Since the method involves a count of each box containing a fracture, the 'artificial' opening displacement of the main crack in many of the specimens created an artificial increase in the area of fractures within the grid. This was overcome by 'averaging' the trace of the main crack into a single line during the tracing procedure. The box counting fractal dimensions measured in this way from each of the fracture patterns from 15 specimens showed a very similar trend. Figure 3.15 shows two typical graphs of log N(r) versus log r, where the negative slope gives the value of D_{BC}. Although 3.15(a) is from a 'dry' test specimen (#0022) and 3.15(b) is from a 'wet' specimen (#0051), both plots show the same trend. From r = 691 to 186 microns, i.e. the large box sizes, the slope is 1.5 to 2.0, followed by a break in slope, and then a slope of approximately 1.0, measured from the smaller box sizes (to r = 21 microns). This was the case with all the box counting measurements, regardless of environmental conditions and rock type. This result does have some significance. The slope of near 2 suggests that the area of the grid is almost filled, by the fracture system at the scale of the large box size, as illustrated in figure 3.16(a). At smaller box sizes, the fracture pattern, and box counting dimension, is dominated by the single throughgoing main crack, producing a fractal dimension D_{BC} near 1.0, as illustrated in figure 3.16(b). This result indicates a possible flaw in the use of the box counting method to quantify fault or fracture systems, and consequently this method is of limited use in this study.

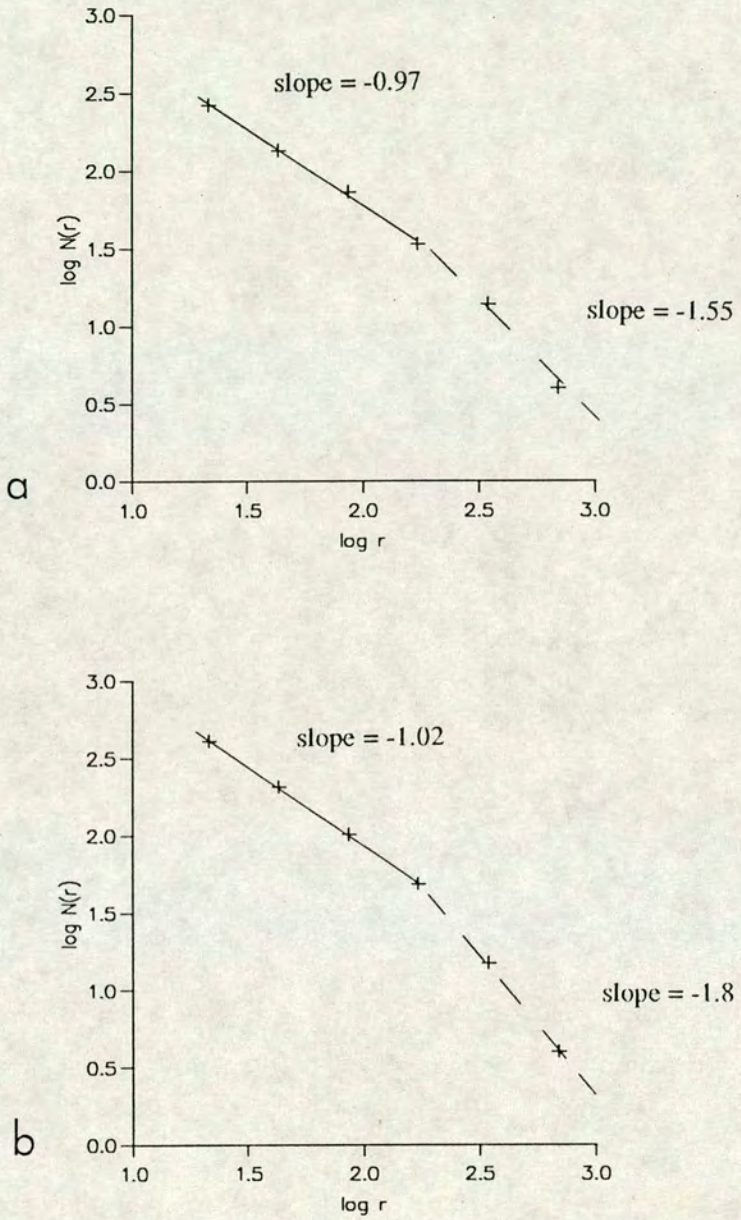

Figure 3.15 Typical plots of box size r (microns) versus the number of boxes entered by the fracture system N(r).

a. 'dry' test #0022.

b. 'wet' test #0051.

Figure 3.16 Illustration of possible problems associated with the box counting technique.

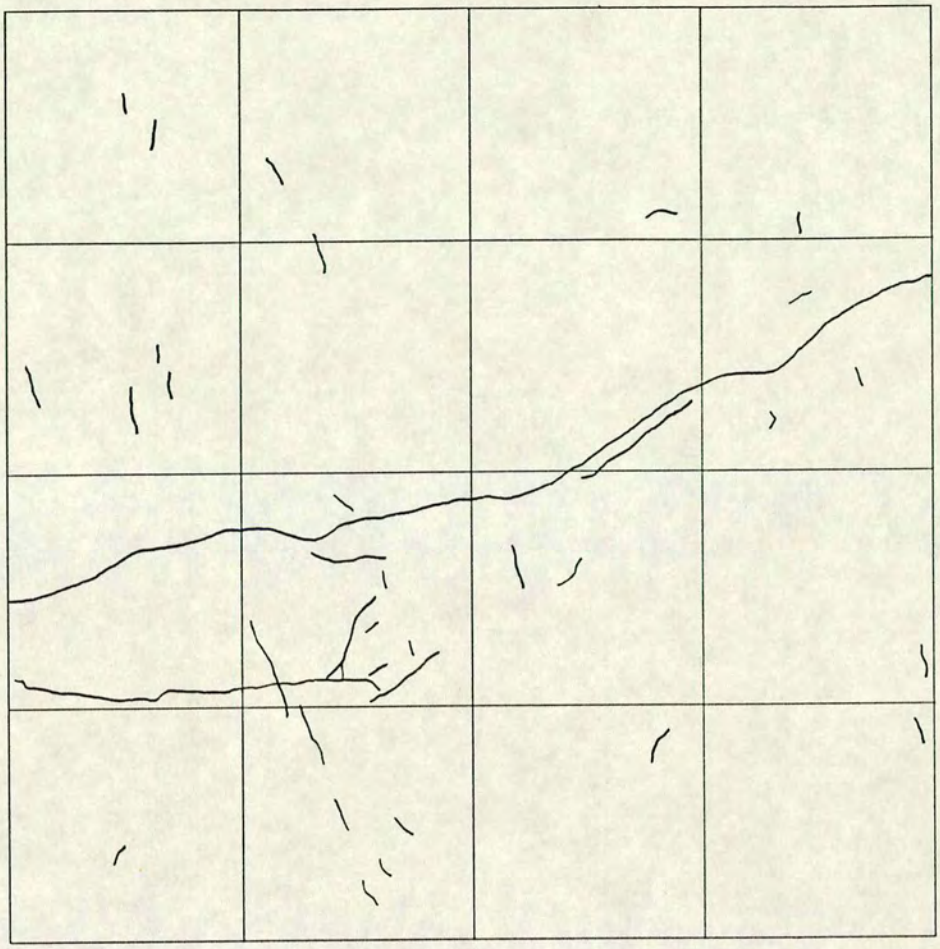

a

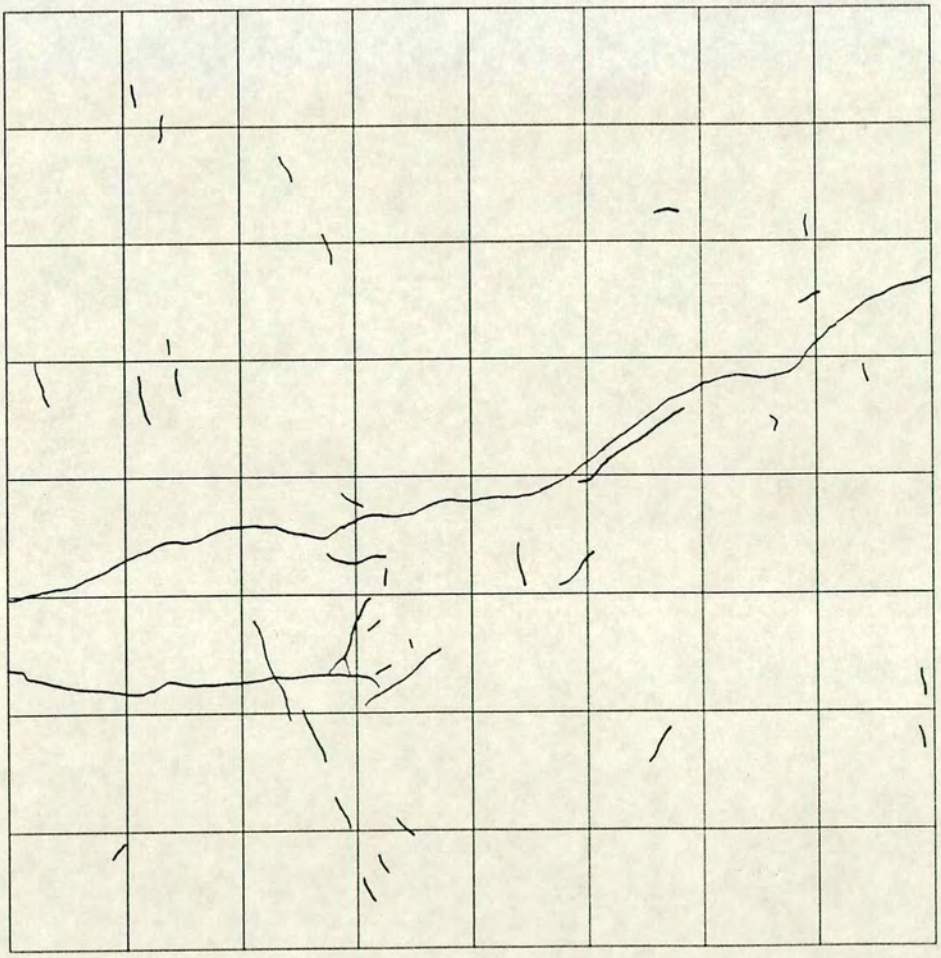

b

Microcrack length distribution exponent

The relation in equation (1.3) describing a fractal distribution may be rewritten as:

$$\text{Log } N(L) = \text{constant} - D \log L \qquad (3.3)$$

and so by plotting Log N versus Log L (a microcrack length-frequency distribution), we obtain an area fractal dimension D_A for the fracture pattern from the negative straight line slope of the distribution. This represents the size distribution of the fracture pattern. It is a length distribution exponent as revealed on a two-dimensional map of fracture traces. For example, figure 1.3(a) shows D = 1.76 for the active faults in the United States (after Shaw and Gartner, 1986).

In this case we are dealing with tensile microcracks which are relatively rough, that is they are fractal (in a similar way to the macrocracks illustrated in figure 3.13). As a result we define the microcrack length in terms of a straight line drawn from tip to tip, (using the approximation that the crack is a straight elliptical fracture and small scale variations in surface topography are not important). Although this method will underestimate the Hausdorff-Besicovitch dimension, it has the advantage of focusing attention on the overall population of cracks rather than the typical roughness of the major crack. The crack lengths are measured from the enlarged tracing to the nearest 0.5 mm and then converted to the actual size in microns by a multiplier obtained from the size of the microscope field of view and photograph size. The granodiorite specimen fracture patterns photographed at x640 were printed onto paper 140 mm by 100 mm, and a multiplier of 11.42 was necessary to convert to microns. The granite specimens photographed at x63 required a multiplier of 57.14.

In measuring the length distribution, the main crack is excluded as the macrocrack length within the field of view does not represent the full length of the crack.

Figure 3.17 shows both the discrete and cumulative length-frequency distributions of the two fracture patterns from the granodiorite specimens illustrated in figure 3.7. To ensure an equal bin size the crack lengths in microns were logged before the histogram was calculated. At progressively smaller crack lengths, the discrete data is seen to peak and then reduce. The most likely explanation is that the data is simply incomplete due to undercounting of the cracks that are not visible or have not reached the surface. A minimum value for the crack length (L_{min}) representing a real or experimentally-controlled lower fractal limit must therefore be introduced, and the data below this disregarded in the calculation of the exponent D. L_{min} varies only slightly in each of the fracture patterns investigated here, and has a typical value of 30 microns (for the granodiorite). Above L_{min} both distributions plot as parallel straight lines on the log-log axes, indicating the expected power law relation in both discrete and cumulative statistics. The fractal range (L_{min} to L_{max}) is typically 1 to 1.5 orders of magnitude. The length distribution exponent D may be estimated from the gradient of the reduced major axis of this distribution (details of the statistical method is given in Appendix C)

Using this method and its error bound, figure 3.17(a), from the air-dry test, gives a relatively low slope and a fractal dimension of 1.16 ± 0.14. However, figure 3.17(b) from the wet test appears to have a relatively higher slope, giving $D = 1.56 \pm 0.18$. This implies that there is a greater relative number of smaller cracks in the latter case, due to the activation of the stress corrosion mechanism by the active environmental fluid. The range of fractal dimensions obtained from the granodiorite specimens using this method was $1.02 < D_A < 1.85$, within the predicted range of $1 <$

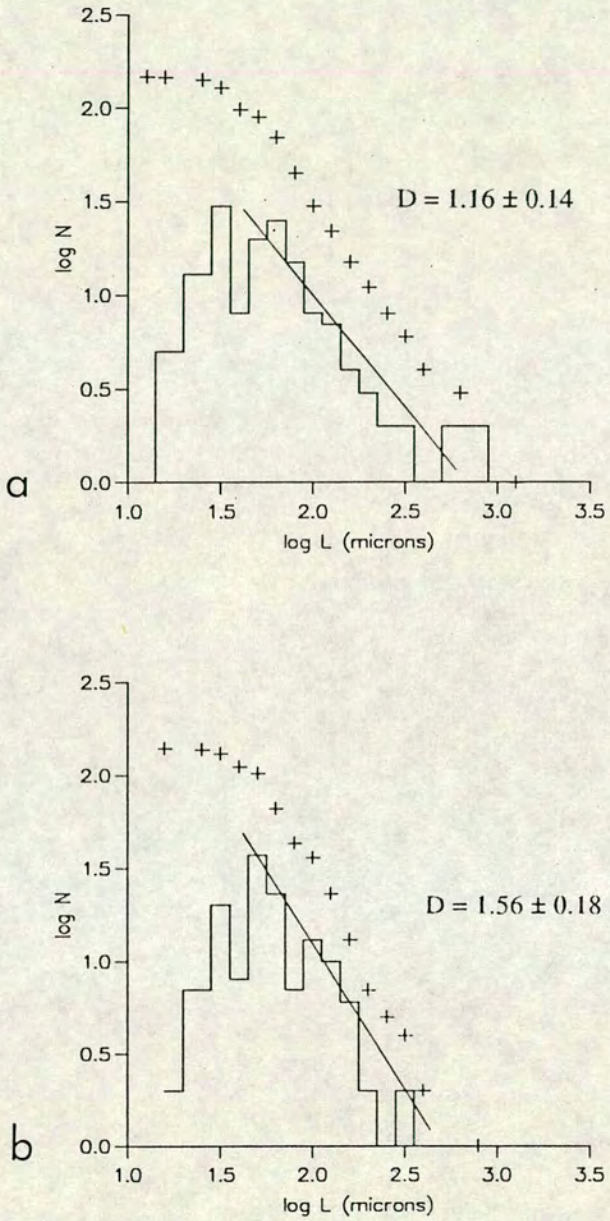

Figure 3.17 Length-frequency distributions of the fracture patterns from the two granodiorite specimens illustrated in figure 3.7. Staircase - discrete data; crosses - cumulative data.

a. 'dry' test #0022

b. 'wet' test #0051.

$D < 2$. Thus the experiments have been successful in covering the possible range of the scaling exponent.

Figure 3.18 shows the discrete and cumulative length-frequency distributions of the two fracture patterns from the granite specimens illustrated in figure 3.10. The granite specimens showed a higher typical value of L_{min} of 200 microns.The number of microcracks in both examples is less compared to the granodiorite, possibly reflecting the larger grainsize. The range in D_A for the granite specimens was $1.45 < D_A < 2.25$. This higher value of D (above 2.0) is possible since it is a length distribution exponent and is fractal only in the sense of Turcotte (1989). It is not a strict Hausdorff-Besicovitch fractal dimension of the range 1.0 to 2.0.

The length distribution exponent D does not appear to suffer from some of the inconsistencies of other methods of quantifying the scale invariance discussed above, and hence allows us to compare the fracture geometries in a quantitative and objective way over a wide range of conditions. As a result, the semantic argument over whether the exponent D is a fractal dimension or not (Turcotte, 1989) is largely irrelevant. In the next chapter, the results of the experiments are analysed, using D as the most consistant structural marker, to test the hypothesis of its relationship to the seismic b-value.

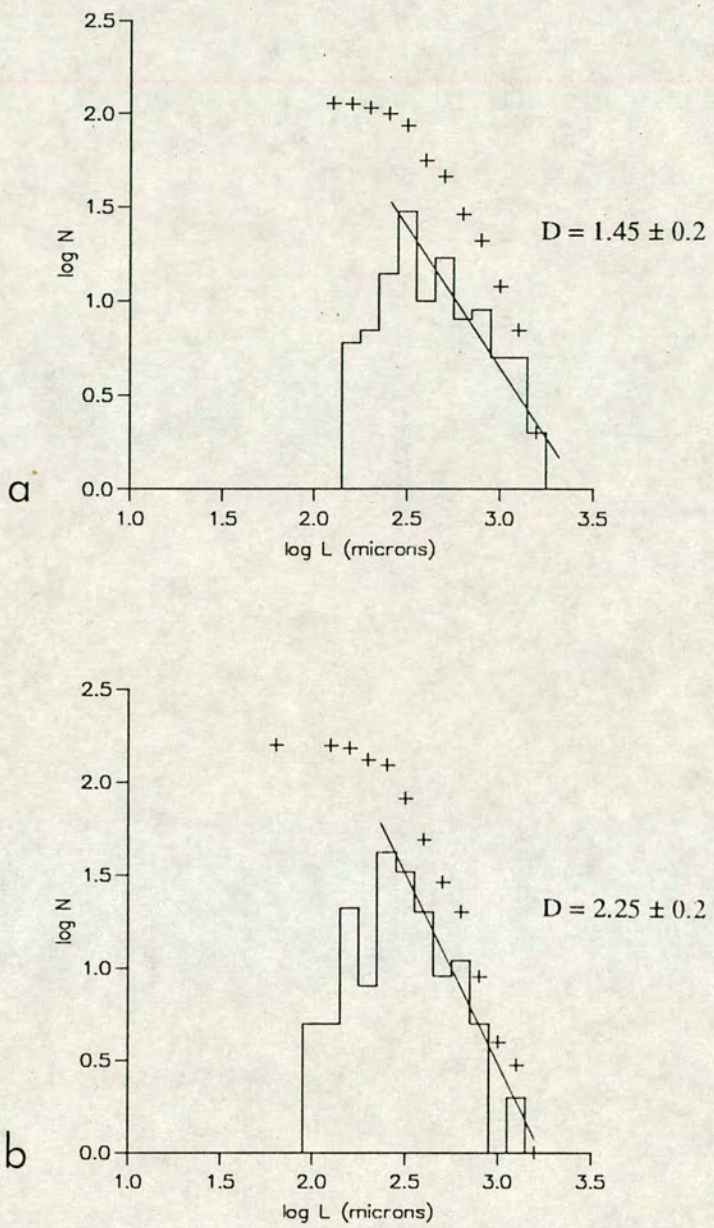

Figure 3.18 Length-frequency distributions of the fracture patterns from the two granite specimens illustrated in figure 3.10. Staircase - discrete data; crosses - cumulative data.

a. 'dry' test #0128

b. 'wet' test #0126

Chapter 4 Synthesis of Experimental Results

4.1 Introduction: summary of results

The previous two chapters have separately described (1) the experimental results from the present study in terms of the physics of crack growth - the stress intensity, K_I; (2) the seismicity of the AE monitored - the AE b-value; and (3) the scaling of microcrack structure - the 'fractal' length distribution exponent D. In this chapter, these results are synthesised for comparison and interpretation. First, table 4.1 comprises two summary tables of results from the tests on the granodiorite and granite specimens respectively. The 'dry' and 'wet' test results are presented separately for each rock type. Several tests using granodiorite specimens were carried out under the same displacement rate in the same conditions to test the reproducibility of the experimental and AE results, (columns 2, 3 and 4). Very similar stress intensity factors are seen in tests run at the same displacement rate, indicating that the test conditions were repeatable. The AE results, (AE b-values), of tests run in the same environment at the same rate show some similarity. However, there are isolated anomalies. For example, test #0006 has a higher b-value, 1.61, relative to the other dry tests. This may well be due to the limited number of AE events recorded above the high cut-off value of 37.5 dB used during this test. Also, test #0035 has a lower b-value than the other wet tests. This may have been an anomalous specimen, since the length distribution exponent D is also much lower than those of the other wet test specimens. The granite specimen #0125 has a very high AE b-value of 2.43. This test was also characterised by a high amount of low amplitude AE. Finally several fracture patterns from some test specimens (#0102, #0055, #0051, #0041) were also examined in order to test the validity of the sampling method of the structural analysis. In general, the length distribution exponents were repeatable

Table 4.1 Summary table of experimental results.

Column 1: assigned test number.

Column 2: macrocrack velocity, in $ms^{-1}x10^{-6}$, calculated from equation 2.6.

Column 3: stress intensity K_I normalised with the fracture toughness K_{IC}.

Column 4: the AE b-value, calculated using a variable cut-off; for individual details see appendix B.2.

Column 5: standard error on b (66% confidence level).

Column 6: number of events N used in b-value calculation, (above the amplitude cut-off).

Column 7: the length distribution exponent D, where applicable. Test results within a box indicate multiple fracture patterns analysed from that specimen. The test results marked test #*tot at the end of each box give the result of the combined length distribution data from all the subsets. Further details of multiple structural analyses are given in appendix E.

Column 8: standard error on D (66% confidence level).

Column 9: number of microcracks used to produce the length distribution.

(a) Results from tests on granodiorite specimens.

(b) Results from tests on granite specimens.

a. Granodiorite

1	2	3	4	5	6	7	8	9
Test	V	K_I/K_{IC}	b	SEb	N (b)	D	SED	N (D)
Dry								
0022	6.9	0.65	1.41	0.08	295	1.16	0.14	70
0104	7.4	0.68	1.31	0.04	3379	-	-	-
0102#1	24.0	0.64	1.35	0.025	2562	1.49	0.16	126
0102#2	"	"	"	"	"	1.56	0.15	126
0102#3	"	"	"	"	"	1.07	0.20	119
0102#4	"	"	"	"	"	1.23	0.15	92
0102#5	"	"	"	"	"	1.34	0.04	145
0102#6	"	"	"	"	"	2.03	0.05	116
0102#7	"	"	"	"	"	1.28	0.16	110
0102tot	"	"	"	"	"	1.54	0.07	780
0006	66.0	0.77	1.61	0.13	143	1.42	0.22	98
0007	56.8	0.82	1.32	0.09	813	-	-	-
0101	66.0	0.61	1.26	0.09	627	-	-	-
0024	670.0	0.87	1.12	0.02	2314	1.02	0.13	91
0055#1	568.0	0.77	1.19	0.04	802	1.38	0.12	226
0055#2	"	"	"	"	"	1.31	0.21	141
0055tot	"	"	"	"	"	1.41	0.08	353
0110	640.0	0.71	1.25	0.08	924	-	-	-
0111	1820.0	0.81	1.06	0.05	1391	-	-	-
Damp								
0052	707.0	0.68	1.59	0.11	189	-	-	-

a. granodiorite continued

1	2	3	4	5	6	7	8	9
Test	V	K_I/K_{IC}	b	SEb	N (b)	D	SED	N (D)
Wet								
0051#1	7.04	0.64	1.95	0.21	81	1.56	0.18	103
0051#2	"	"	"	"	"	1.71	0.16	131
0051#3	"	"	"	"	"	1.78	0.18	189
0051#4	"	"	"	"	"	1.52	0.17	209
0051tot	"	"	"	"	"	1.71	0.12	712
0118	21.3	0.64	1.96	0.36	27	-	-	-
0028	62.6	0.71	1.61	0.16	90	1.24	0.17	131
0117	89.0	0.70	1.75	0.15	121	-	-	-
0037	170.0	0.73	1.99	0.21	82	1.66	0.21	177
0035	660.0	0.68	1.24	0.1	125	1.06	0.11	69
0036	638.0	0.67	1.84	0.15	130	1.37	0.21	104
0040	550.0	0.76	1.62	0.27	34	-	-	-
0116	637.0	0.73	1.43	0.2	45	-	-	-
0041#1	1770.0	0.77	1.42	0.09	197	1.15	0.16	123
0041#2	"	"	"	"	"	1.32	0.13	118
0041#3	"	"	"	"	"	1.85	0.22	91
0041#4	"	"	"	"	"	1.51	0.14	154
0041tot	"	"	"	"	"	1.63	0.12	530
0119	2440.0	0.71	1.85	0.27	42	-	-	-

b. Granite

1	2	3	4	5	6	7	8	9
Test	V	K_I/K_{IC}	b	SEb	N (b)	D	SED	N (D)
Dry								
0122	42.8	0.71	1.07	0.02	1839	1.74	0.23	108
0123	478.0	0.62	1.25	0.04	901	1.45	0.09	96
0128	1047.0	0.85	1.05	0.01	3006	1.45	0.2	100
Wet								
0125	131.0	0.73	2.43	0.31	59	1.79	0.18	151
0126	409.0	0.71	1.68	0.13	157	2.25	0.21	124
0127	1210.0	0.76	1.78	0.17	103	2.00	0.15	289

when taken from different parts of the same specimen. However, some variation was observed. This is discussed further in appendix E.

Since each of these parameters was calculated for each test and test specimen individually, it is now possible to examine the correlations between these three separate aspects of crack growth.

4.2 Relation of seismic scaling to the physics and chemistry of subcritical crack growth

The experimental control parameters of each test may be correlated with the seismic data recorded during the test in the form of a plot of the stress intensity acting during the time period of constant K, against the b-value calculated from the acoustic emissions monitored during the same period. Figure 4.2 is a summary diagram of K_I/K_{IC} versus AE b-value. Normalising the stress intensity by the mode I fracture toughness K_{IC} allows data from the two different rock types to be plotted on the same axes. Each data point on the diagram represents a single test. As already mentioned (section 3.1.2), two different lower cut off amplitudes were used in calculating the b-values for the wet and dry tests to reduce the error in b. It should be noted that if the same value ($a_c = 48.5$) is used for all the tests, the major characteristics of the b versus K_I/K_{IC} plot do not change, apart from introducing more scatter into the dry test results.

Several observations may be made from figure 4.2. Firstly, it appears that the relation between the stress intensity and the AE b-value is independent of rock type and specimen size. Both rock types tested, the Loch Uisg microgranodiorite in its relatively small specimen size (section 2.1.1), and the Ballachulish granite in its larger specimen size, show very similar trends once K_I has been normalised by K_{IC}.

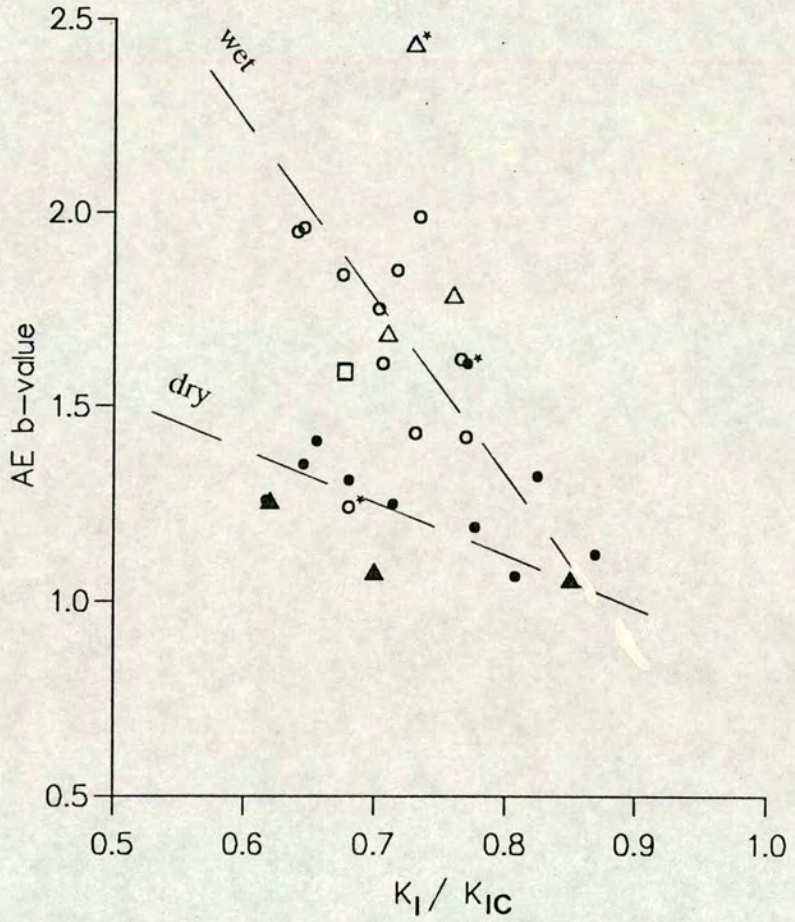

Figure 4.2 Relation of AE b-value with normalised stress intensity K_I / K_{IC} from the present experimental program.

granodiorite: granite:

- ● dry ▲ dry
- □ damp △ wet
- ○ wet

The correlation line plotted for the dry tests has a gradient of -1.3 ± 0.3 and correlation coefficient r = -0.6. The correlation line plotted for the wet tests has a gradient of -4.5 ± 1.0 and correlation coefficient r = -0.6. The lines converge at around b = 1.1 and K_I / K_{IC} = 0.85. The asterixes mark those test results deemed anomalous, and therefore, not included in the correlation line calculations.

Secondly, the data are observed to divide into two populations on the basis of fluid content. The wet tests run at a low displacement rate and low crack velocity with H_2O present in the environment of the crack tip, plot in the low K - high b region of the graph. Wet tests run at a high displacement rate plot with higher K, lower b. Air-dry tests, with no fluid present, run at high displacement rates also plot with high K - low b. However, dry tests run at lower displacement rates plot in the low K - low b region. Correlation slopes may therefore be drawn independently for the wet and dry populations. These are both seen to be negative; the 'dry' slope has a gradient of -1.3 $\pm$ 0.3 (with a significant negative correlation coefficient of r = -0.6), the 'wet' slope has a higher gradient of -4.5 $\pm$ 1.0 (r = -0.6). The two slopes converge at around $K_I/K_{IC} = 0.85$, b = 1.1. (The correlation slopes do not include the anomalous results that are marked with an asterix). The test that was run in 'damp' conditions as an intermediate case plots between these two populations.

Tests run at low displacement rates, with low stress intensities, that is those promoting slow subcritical crack growth, show a first order effect of fluid presence. The wet tests give high AE b-values indicating many small AE events, suggesting that the effect of stress corrosion is to produce a distributed array of smaller microcracks. In constrast, the dry tests give low b-values, indicating a higher proportion of large to small events when there is a smaller quantity of active chemical agent present to initiate stress corrosion reactions. Thus more of the overall crack growth is concentrated on the largest cracks.

Tests run at high displacement rates, with high crack velocities and high K, show less difference between the wet and dry tests. Both give lower b-values suggesting that even if fluid is present there is less time for stress corrosion reactions to occur at the crack tip as crack growth is more dynamic. The physical movement of fluid to the crack tip is also likely to be limited by the high velocity of rupture at the

tip. The correlation lines converge at high K indicating that the mechanism of crack propagation is highly sensitive to fluid presence and environmental conditions at low K and low V. This is less obvious at higher K and dynamic fracture velocities where fluid movement to the crack tip environment is limited.

In summary, figure 4.2 shows the physics of the process on the x-axis (normalised stress intensity and crack velocity), the seismicity of crack propagation (b-value) on the y-axis, and the chemistry involved (activation of stress corrosion as a result of fluid-rock interaction) in the separation of the 'wet' and 'dry' populations. Three important conclusions can be made. First, the presence of an active fluid at the crack tip has a first order influence on seismicity during tensile fracture. Second, the b-value correlates negatively with stress intensity, suggesting that at higher stress concentrations there is a higher proportion of larger seismic sources. Thirdly, these results are independent of rock type and specimen size. These results are consistant with previous work using the double torsion relaxation method (Meredith and Atkinson, 1983; Main et al., 1990).

4.3 Relation of structure to seismicity at microfracture scale

Although it may seem self evident that small microcracks would result in low amplitude AE (with the analogy that small natural fractures would produce low magnitude seismicity), this relation has not until now been observed and tested quantitatively. As described in the previous chapter, for each double torsion test and specimen we have two independant quantitative measurements reflecting (1) the scaling of the seismicity associated with crack growth during the test (the AE b-value), and (2) the structure left in the specimen after the test, (the power-law length distribution exponent, D). Figure 4.3 shows the results from the tests on the granodiorite specimens alone, as a plot of the AE b-value, calculated by the

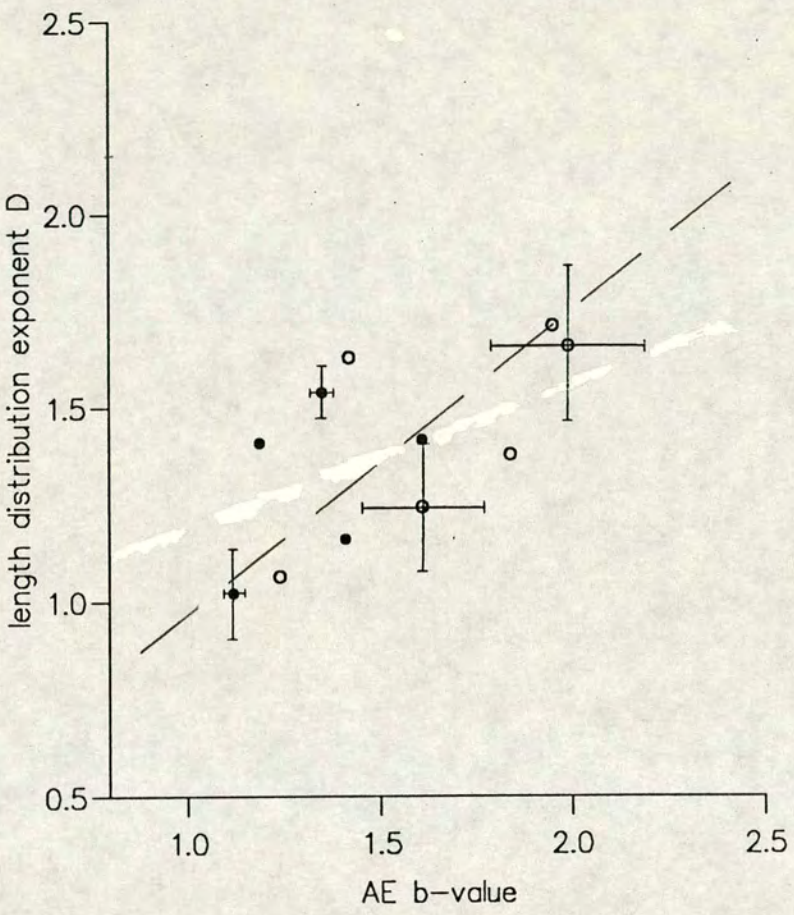

Figure 4.3 Relation of length distribution exponent D with AE b-value from the granodiorite specimens alone from the present experimental program. Error bars represent one standard error to either side of the data point.

● dry

○ wet

The dashed line shows the best fit line through the data, and has a gradient of 0.79 ± 0.18, intercept of 0.18 ± 0.28, and correlation coefficient r = 0.62.

maximum likelihood method (section, 3.1.2; Aki 1965), versus the exponent D, calculated from the gradient of the reduced major axis of the straight line length distribution (section 3.2.2; for statistical method see appendix C). Several typical error bars (of one standard error to either side of the data point, in both b and D) are included, showing the systematically higher errors in b-value associated with the wet tests. The data points for those specimens tested for variation in D (see appendix E) represent the combined length distribution exponents from all the microcrack length data collected from the specimen, (the test#*tot results of figure 4.1 and appendix B.3). Therefore, each point on the graph of figure 4.3 represents a single specimen. The wet and dry test results again plot separately, as in the K_I/K_{IC} vs b diagram of figure 4.2. The wet test specimens generally show high D as well as high b, indicating a higher ratio of small to large cracks, suggesting that the presence of the active environmental agent and fluid-rock interaction is affecting the structure as well as the seismicity during crack growth.

Overall, a positive correlation between D and b from the granodiorite specimens is apparent from this plot, as predicted from equations (1.19) and (3.3), although there is a relatively large scatter. The general scatter in the data may be attributed to the relatively small number of cracks which could be reliably imaged optically in each specimen, the difficulties in maintaining a constant stress intensity at the crack tip (section 2.3.2), and the problem with background noise encountered during the wet tests (section 3.1.2). To test the correlation for the granodiorite results alone, Pearson's product-moment correlation coefficient, r, of D with b was found to be 0.62 indicating that the positive correlation between the AE b-value and length distribution exponent D from the granodiorite specimens is statistically significant. Therefore, a straight line may be drawn on the b vs D plot of figure 4.3, thus giving a gradient and intercept for the relationship. The gradient of the reduced major axis,

given by Williams (1986) (see appendix C), is found to be 0.78 ± 0.18, and the intercept to be 0.18 ± 0.28 so that:

$$D = 0.78\ b + 0.18 \qquad (4.1)$$

Results from tests on both the granodiorite and granite specimens are shown on the same axes in figure 4.4. The granite specimens appear to give higher D exponents from the structure, compared to the granodiorite specimens with similar b-values, although a positive trend in the data is still evident (where the correlation coefficient $r = 0.45$, giving a less significant result than for the granodiorite specimens alone). This may be due to the larger grain size, and higher length cut-off value (Lmin) necessary in dealing with the granite specimens. The slope (reduced major axis) from all the data in figure 4.4, i.e. both the granodiorite and granite results, is 0.84 ± 0.18. This is not significantly different from that obtained from the granodiorite results alone.

In summary, the exponent D obtained from the structure in the granodiorite test specimens is positively correlated with the AE b-value. More tests on granite specimens would be necessary to determine the relationship of D with b for the granite, and the effects of rock type and specimen size on this relationship. The limited tests carried out in this experimental program indicate that the relation would be similar, perhaps with a different scaling factor.

Equation (4.1) approximates within its error bounds to a straight line of slope just less than 1.0 passing near the origin, similar to equation (1.19)* as predicted by a dislocation model of the seismic source (sections 1.4.3 and 1.5) . However, it must be remembered that the exponent D obtained from the test specimen is a measure from a two-dimensional slice, whereas b represents the microseismicity from the three-

*if c=3

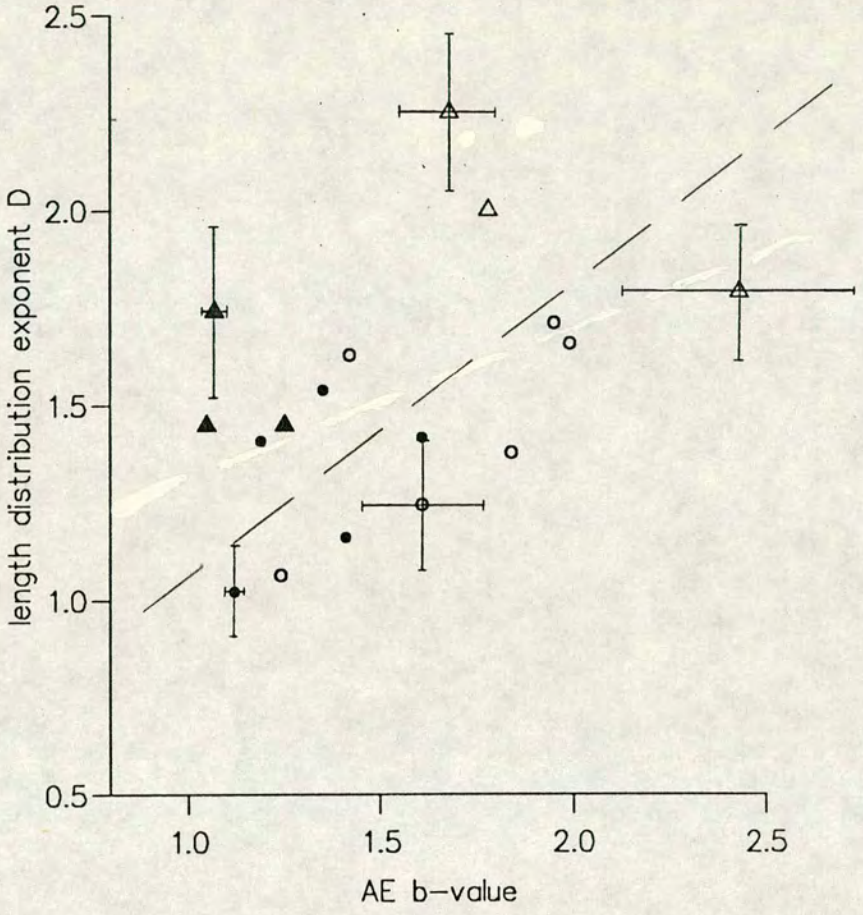

Figure 4.4 Relation of length distribution exponent D with AE b-value from both the granodiorite and granite tests of the present experimental program. Error bars represent one standard error to either side of the data point.

granodiorite: granite:

● dry ▲ dry

○ wet △ wet

The dashed line shows the best fit line through all the data, and has a gradient of 0.84 ± 0.18, intercept of 0.23 ± 0.29, and correlation coefficient r = 0.45.

dimensional specimen (see section 3.2.2). Thus equation (4.1) confirms a positive correlation between these two parameters but cannot be compared directly with equation (1.19). This comparison is discussed further in the next subsection.

Discussion

It should not be expected that the two-dimensional (areal) crack length exponent D_A should correspond directly (one to one) with the three-dimensional (volumetric) crack length exponent D_V, and consequently this will affect its precise relation with b. However, D_V and D_A themselves should be positively correlated (Heffer and Bevan, 1990). In all cases, we would expect $D_V \geq D_A$ by definition. For ideal, self-similar fractal objects formed by a deterministic algorithm (Mandelbrot, 1982):

$$D_V = D_A + 1 \qquad (4.2)$$

but it is clear that this simple relation does not hold in general for the power-law exponent of fault and fracture length distributions. For example, it is observed that $1 < D_V < 3$ (Main et al., 1990), whereas $D_A > 1$ by definition for the case of the 1-dimensional interception on a 2-dimensional surface for a fractal array of cracks. In particular, the condition for dynamic failure is marked by $D = 1$, both in direct observation of throughgoing fault systems and as inferred from the seismic b-value of foreshock sequences (Main et al., 1990). If a more general correlation is linear and positive, then:

$$D_V = \alpha D_A + \phi \qquad (4.3)$$

where $\alpha = 1.0$ and $\phi = 1.0$ for deterministic fractals. This may then be applied to equation (1.19), so that the predicted relationship between the AE b-value and the area exponent measured on the polished surface is:

$$D_A = \frac{3b}{\alpha c} - \frac{\phi}{\alpha} . \qquad (4.4)$$

Thus equation (4.1) may be interpreted with respect to the generalized equation (4.4). From equation (4.4), where $3/\alpha c$ = slope and $-\phi/\alpha$ = intercept, and assuming c=3 (see section 1.5), this result gives $\alpha = 1.28$ and $\phi = -0.23$. This gives $D_V > D_A$, but not in the manner suggested by deterministic fractals (equations 4.2 and 4.3). Thus D may be a fractal dimension in the sense of Turcotte (1989), but it is not equivalent to a Hausdorff-Besicovitch dimension with strict self-similarity.

If c is different from this estimate then we would expect different ranges for D_V: for $c = 1.5$, $3.02 < D_V < 5.58$; and for $c = 1$, $4.54 < D_V < 8.39$. These values of c produce unacceptably high inferred values of D_V, which proves self-consistency at least. There is no value of c consistant with the self-similar scaling of deterministic fractals.

The difference between D_A and D_V may arise because of mode I cracking being concentrated on the free polished surface in the double torsion loading arrangement. Microcracks will then tend to preferentially grow into the plate from the initial flaws on the free surface. The upper surface fails with some compressive component and will tend to resist mode I cracking. Therefore, the microcrack array produced is anisotropic. This might imply that the fractal scaling is self-affine (different in different directions) rather than self-similar, with D_A varying from a maximum on the polished undersurface, to a minimum on the upper surface, and with

the smallest microcracks preferentially confined to the outer surface with the greatest mode I stress concentration and greater fluid presence. This suggests that although only a single value of D_V exists for any sample, D_A can have an infinity of values within its limiting bounds, depending on the orientation of the 2-dimensional section. Since natural stress fields are predominantly anisotropic, natural fracture patterns will also tend to be self-affine rather than strictly self-similar. Thus it will be very difficult to measure a single true fractal dimension from a two-dimensional map or outcrop.

An additional complication may arise if seismic moment does not scale with length cubed, for example for seismic sources large compared to the specimen thickness, (with the analogy of the finite seismogenic depth in the brittle crust, section 1.4.4). In the general case we might have $M_o \propto L^{\eta}$, so that the slope of equation (4.1) would be equal to $\eta / \alpha c$, where η need not necessarily be equal to 3. This discussion highlights the importance of establishing the seismic scaling exponents η and c independantly in future studies. This would require more accurate, broadband recording of the seismic sources, as well as accurate determination of source locations and path effects between the seismic source and the receiver.

Therefore, although a definite positive correlation between b and D_A has been established, it is not possible at present be more precise about the relationship between D_A and D_V than in the preceding discussion, other than to say that field results (D_A) should not simply be treated as self-similar fractal dimensions. Nevertheless, the relations obtained here may be used to justify the previously assumed linear scaling of b with D.

Chapter 5 Natural Tensile Fracture

The structural element of this study would be incomplete without a comparison between the laboratory derived data and data from natural fracture patterns in the earth. Iceland was chosen as the ideal locality to study pure tensile fracture in the field since it is situated on a divergent plate boundary that is currently experiencing extensional stress. This tensional stress produces both normal faulting and tensile fissuring. The aim of the fieldwork was to investigate quantitatively the geometry of tensile fractures in the field within the active rift zone of north east Iceland. Since the laboratory experiments are an attempt to produce an artificial analogy to natural tensile fracture in the earth, this fieldwork was to test the validity of this analogy. Also, since Iceland is active tectonically at present, there was also the possibility of obtaining natural seismicity data from the same region.

5.1 Brief tectonic history of field area: Krafla Fissure Swarm, north east Iceland

The structure of Iceland, as well as its seismicity and volcanism, is dominated by the Mid Atlantic Ridge, which crosses the country from north to south, and marks the divergent plate boundary between the American and European plates. Iceland is also situated over the site of a major mantle hot spot that has been aiding lava production for the past 16 million years. The area of Iceland that is currently active is known as the Neovolcanic Zone, and is defined by seismic activity and volcanic rocks younger than 0.7 million years. This zone may be divided into an axial rift zone and flank (or lateral) zones, as illustrated in the inset of figure 5.1 (after Saemundsson, 1978). The axial rift zones are areas of active plate movement and are affected by tensional stresses parallel to the spreading direction. The evolution of the rift zones

Figure 5.1 Simplified map of the axial rift zone of north east Iceland (after Björnsson, 1985). The dark arrows indicate the direction of movement of the American and European plates.

Index:


lava older than 0.7 My.


central volano


fissure swarm:

T: Theistareykir

Kr: Krafla

F: Fremrinámur

A: Askja

Kv: Kverkfjöll

TFZ: Tjörnes Fracture Zone

Inset. Map of Iceland showing the Neovolcanic Zone and inferred stress distributions (after Saemundsson, 1978). The dark arrows indicate the spreading direction.


axial rift zone


lateral rift zone


inferred shear systems

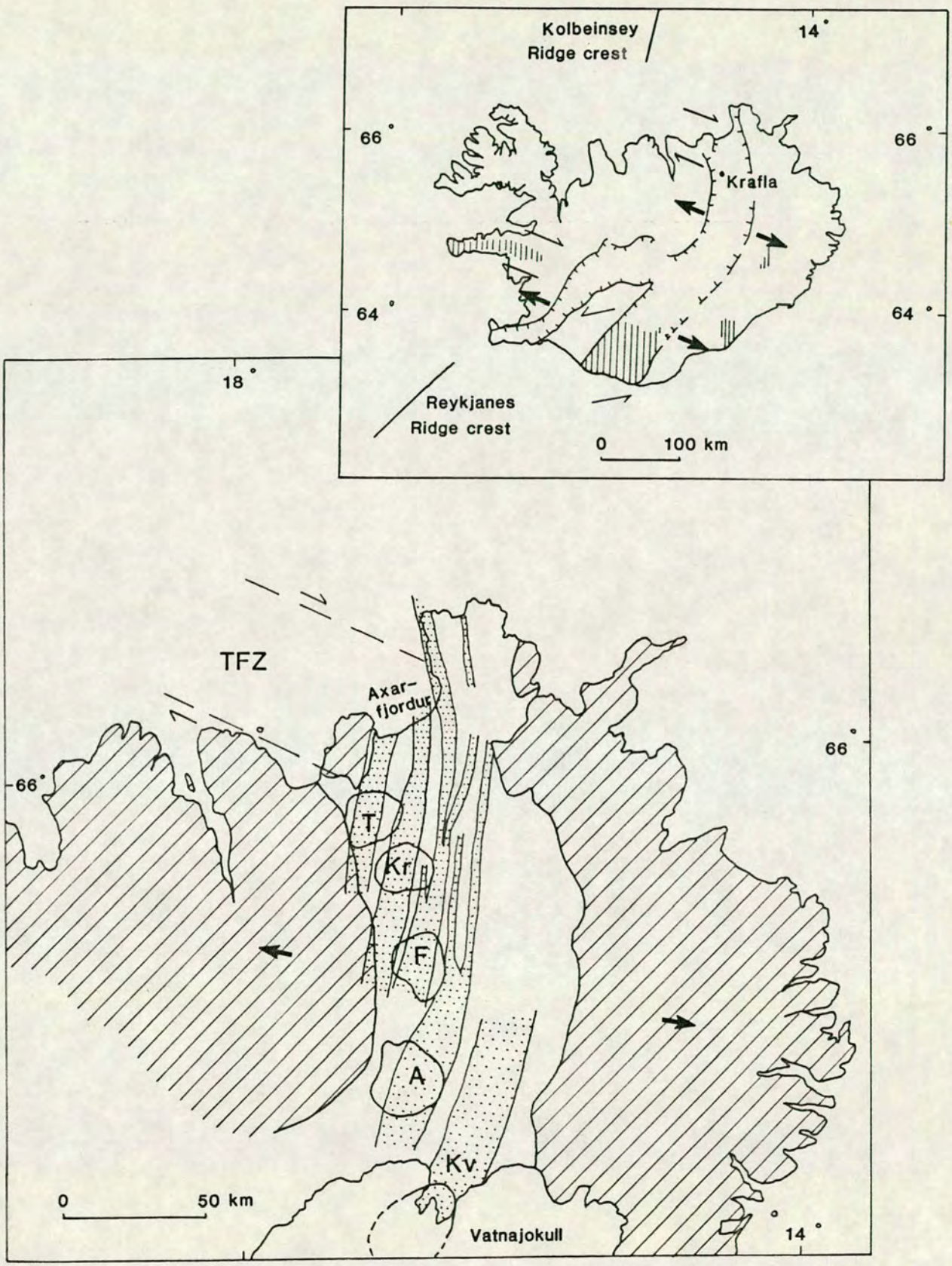
Kolbeinsey
Ridge crest
14°
66°
66°
Krafla
64°
64°
18°
Reykjanes
Ridge crest
0 100 km
TFZ
Axar-
fjordur
66°
66°
T
Kr
F
A
Kv
0 50 km
Vatnajokull
14°

has been shown to involve a jump in the location of the spreading ridge from the west to the east of the island (Saemundsson, 1974). This is thought to be caused by a westward drift of the plate boundary, and propagation of the new rift zone above the 'stationary' hot spot (Saemundsson, 1974; Einarsson, 1991). The flank zones are characterised by horizontal shear stresses (Saemundsson, 1978), and are possibly related to the shifts of the axial rift zones.

The rift zone in north Iceland consists of five volcanic systems, each containing a central volcano with an associated en echelon fissure swarm oriented 10° E, perpendicular to the spreading direction, as illustrated in the main part of figure 5.1 (after Björnsson, 1985). In the north, the rift zone connects with the transverse Tjörnes Fracture Zone, and offshore with the Kolbeinsey Ridge. Rifting within the northern rift zone is episodic, with major events occuring every 100-150 years, affecting only one system at a time (Björnsson et al, 1977; Saemundsson, 1978).

The Krafla Fissure Swarm extends 80 km from south of Mývatn to Axarfjördur in the north, figure 5.2 (adapted from Jóhannesson and Saemundsson, 1989, Geological Map of Iceland, 1:5000 000). The zone of fractures and fissures varies from 4 to 10 km wide. The area was active in 1724-1729, and again most recently in 1975-1984 with some activity continuing until 1989. This most recent volcano-tectonic episode began in December 1975. It was initiated by the accumulation of extensional tectonic stress built up from plate movements, and additionally an increase in pressure due to an inflow of magma into the Krafla magma chamber (Tryggvason, 1984; Einarsson, 1991). This combination leads to local stresses which are effectively tensile ($\sigma_{3e} < 0$) where $\sigma_e = \sigma_3 - p$ (where p is the pore-fluid (magma) pressure). Individual events over the nine years were characterised by repeated inflation (uplift) and subsidence of the Krafla central volcano, rifting of the

Figure 5.2 Simplified map of the Krafla Fissure Swarm (adapted from Jóhannesson and Saemundsson, 1989, Geological Map of Iceland, 1:5000 000). Several of the major fractures are marked in black. The main fractures measured for this study are marked in blue.

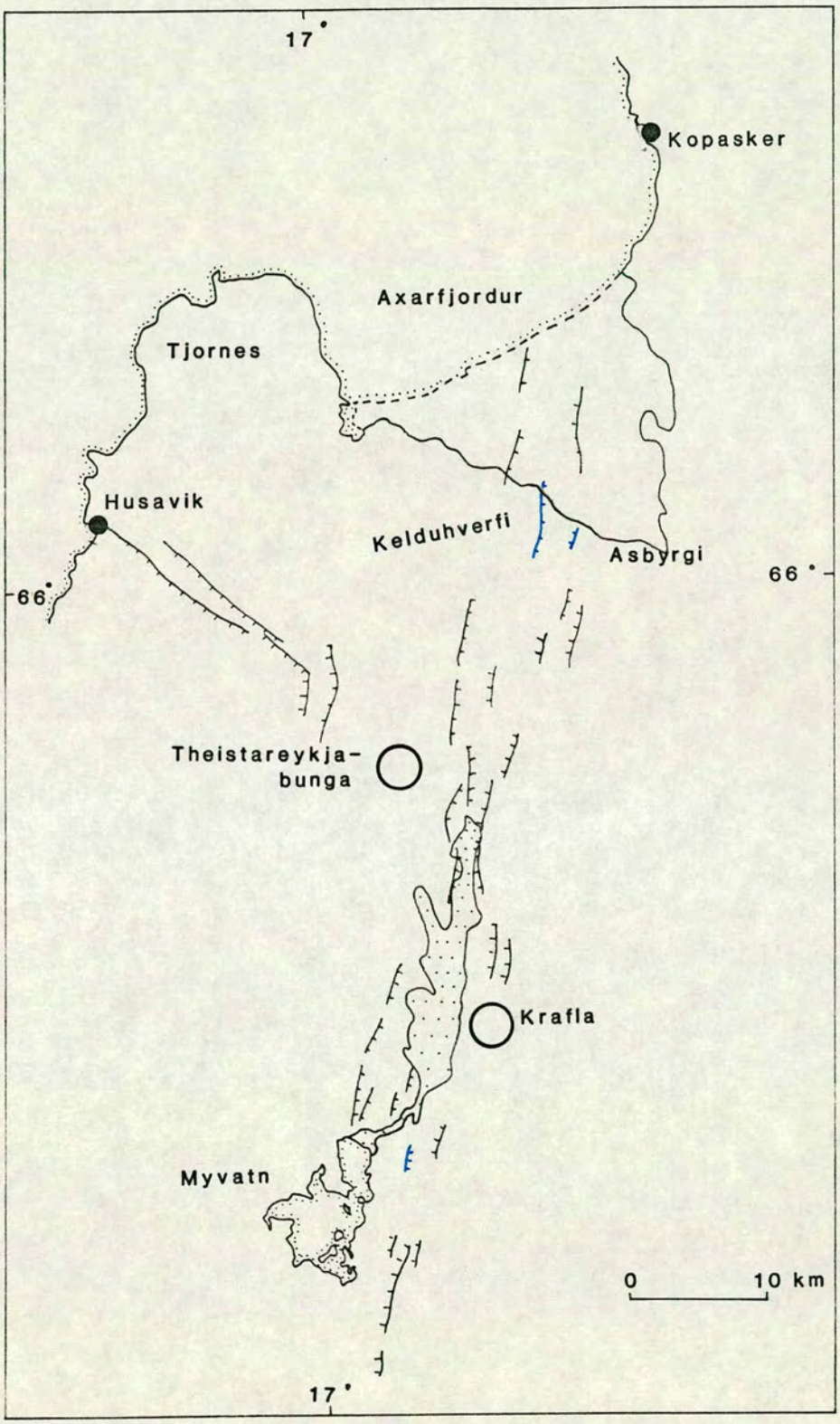
17°
Kopasker
Axarfjordur
Tjornes
Husavik
Kelduhverfi
Asbyrgi
66°
66°
Theistareykja-
bunga
Krafla
Myvatn
0
10 km
17°

fissure swarm and associated seismic activity. Several models of the dynamics of rifting have been proposed. Seismic evidence from earthquake migration supports a model of lateral magma flow from the magma chamber into dykes north and south along the fissure swarm (Einarsson, 1991). Fissuring and fracturing is proposed to occur above the dyke intrusion. An alternative model proposes migration of magma along cracks in the lower crust, thus lowering the failure stress and initiating rifting (Björnsson, 1985). It is probable that a combination of mechanisms is responsible.

Rifting within the fissure swarm during the most recent episode involved both the opening of new ground fissures and the reactivation of existing ones. Levelling, tiltmeters and displacement meters were used during the activity to monitor ground displacements and surface deformation (Björnsson et al., 1979; Sigurdsson, 1980; Hauksson, 1983). The total amount of widening of the fissure swarm during the whole episode varied from south to north. A maximum widening of 8 m was observed at Leirhnjúkur above the Krafla magma chamber. This decreased to zero widening at a distance of 15 to 20 km south of Leirhnjúkur. In the north, dilation also decreased to 2 m at Axarfjördur (Tryggvason, 1984).

As well as monitoring of the seismic activity (Brandsdóttir and Einarsson, 1979; Einarsson and Brandsdóttir, 1980), and ground movements during the activity (Björnsson et al., 1979; Sigurdsson, 1980; Hauksson, 1983), a study of the geometry of the fractures in the fissure swarm was also carried out from fieldwork and aerial photographs (Opheim and Gudmundsson, 1989). The length distribution of measured fractures showed a higher proportion of short fractures to long fractures, and a preferred orientation of between 03°E and 18°E, i.e. approximately perpendicular to the minimum principal tectonic stress (σ_3), although a detailed study of any individual fractures was not included. This background appeared to encourage the planned fieldwork for this project.

5.2 Method and details of field measurements

Two areas within the Krafla Fissure Swarm of north east Iceland were chosen for the field study, due to (1) good exposure, and (2) the recent spreading event in this region (1975-1984), which provided a chance to measure new and recently reactived fractures.

The main aim of this fieldwork was to find a natural analogy to the double torsion test specimens and their fracture geometry, as illustrated in figures 3.8 to 3.10. It was decided to choose a single major fracture in an area of good exposure, and to measure all of the smaller associated tension fractures in the areas directly adjacent to it. Since the stratigraphy in this area consists of relatively thick (1-2 m), approximately horizontal lava flows, as close a comparison as possible may be made to the specimens.

Several operational rules were necessary in carrying out the field measurements:

1. The most significant measurement to be made was the length of the fracture, for comparison with the artificial microfracture length distributions. In the field, as in the laboratory, the length of the fracture was measured as a straight line from tip to tip with a tape measure. This avoided the complications of fracture roughness, as discussed earlier in Chapters 1 and 3. An estimated error of 10% was also unavoidable due to irregularities of the lava surface.
2. Columnar jointing was present in almost all of the lava flows. This had a characteristic dimension of 20-50 cm main cross sectional diameter. The joints were usually closed with no appreciable width. However, open fractures occasionally would terminate within a damage zone taking advantage of the weakness of the columnar jointing, as shown in figure 5.3(a). A systematic rule was used that if the

joint showed any recent opening, that is with relatively unweathered surfaces and no significant infill of sediment or vegetation, then a tectonic cause was inferred and the length included.

3. Several fractures were observed to diverge into three or more smaller fractures at one end, as illustrated in figure 5.3(b). In this case, the length of the fracture was measured from end to end including the smaller fractures. The length of each smaller fracture was also measured individually for completeness.

4. Fractures that terminated in a free edge were excluded, since an accurate measure of their full length was not possible.

5. Discontinuous en echelon fractures were counted and measured as separate fractures if distinct ends to the fractures could be observed, figure 5.3(c).

6. The width of the fracture was taken as the maximum width along its length and measured with a tape. This was usually near the centre of the fracture. Care was taken to record the true width if collapse had occured within the fracture producing a graben structure, as illustrated in figure 5.3(d). An estimated error of 10% was also unavoidable.

7. Orientations of the fractures in plan view were measured as the orientation of a straight line drawn from tip to tip.

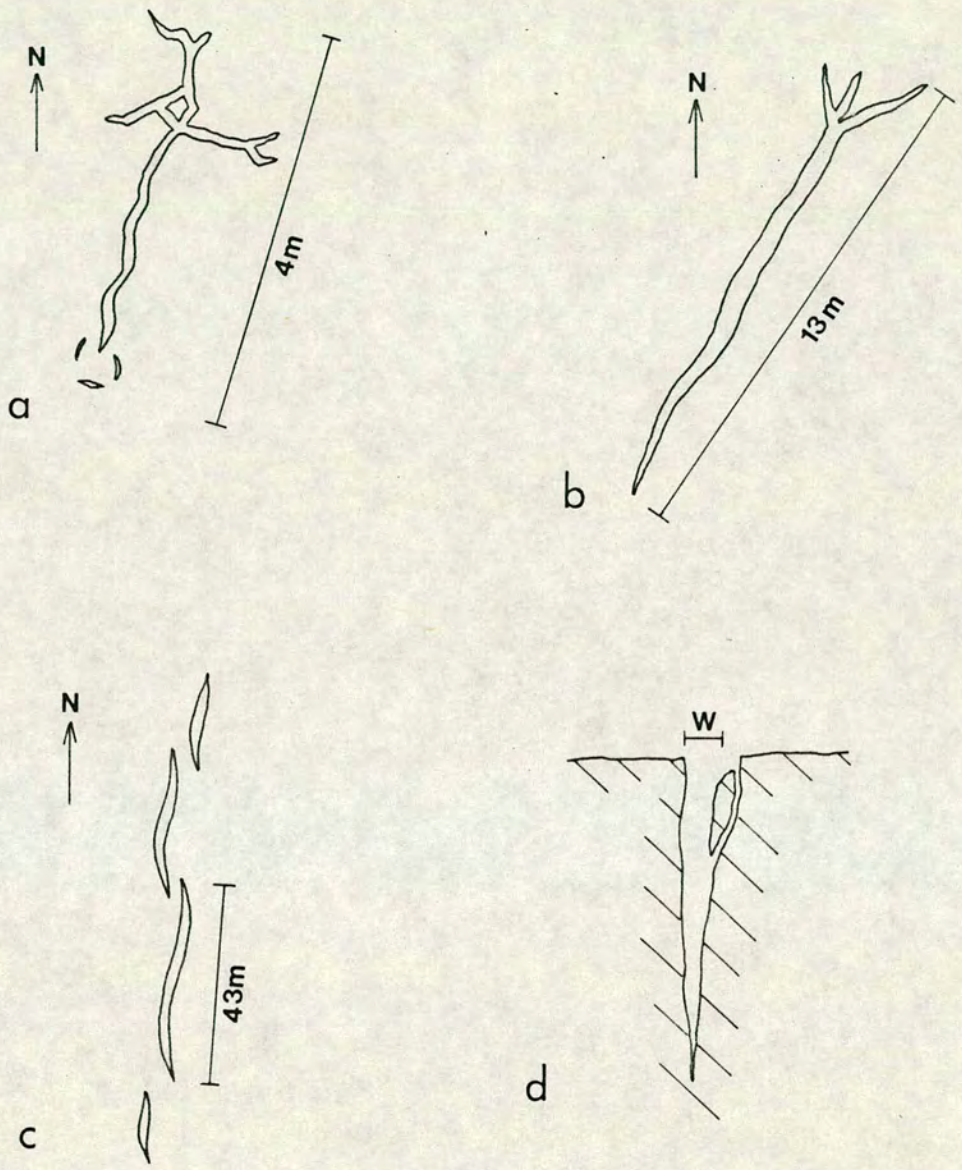

Figure 5.3 Field sketches of fractures measured in the Krafla Fissure Swarm.

a. Open tensile fracture terminating in a damage zone within open columnar jointing at the northern end of the fracture.

b. Fan structure at one end of a tensile fracture.

c. Discontinuous fractures.

d. Width measurement of open fracture, avoiding infallen block.

5.3 Results of structural analysis of natural tensile fracture populations

Two major fractures and their associated populations of smaller fractures were measured; one in the north of the fissure swarm at Kelduhverfi, and one in the south at Mývatn. Several other large fractures and populations were measured in both areas.

Kelduhverfi

In the north of the fissure swarm, near the coast at Axarfjördur, the lavas are 10,000 year old pahoehoe flows from the Theistarykjabunga centre to the south. This area experienced the beginning of the recent activity in 1975, and was also affected by several of the later events. The major fracture chosen, F1, is marked in blue on figure 5.2. The area is also shown in more detail in figure 5.4, (from an aerial photograph), where the major fractures studied are also marked in blue. The F1 population proved to be the most useful in the field, due to good exposure on both sides of the normal fault along its total length. Several other large fractures, including F128 marked on figure 5.4, were also measured with their populations of smaller fractures. However, relatively poor exposure due to vegetation limited the total amount of fractures measured. In the analysis of the field results, the F1 population is examined as a specific case, followed by the results from all the fractures measured in Kelduhverfi grouped as a more general population.

The total number of fractures measured in the F1 population was 80, including F1 itself. F1 is the surface expression of a normal fault with a significant tensile opening, of length 2275 m, trending approximately north-south with a strike of 011° E. The maximum width, representing the tensile component, was 18 m. The fault downthrows to the west, with a throw that varies along its length from 9 to 11 metres

Figure 5.4 Aerial photograph of the Kelduhverfi area. The main fractures measured, including F1, are marked in blue. The rose diagrams illustrate the orientations of the fracture populations measured. The class interval is 30°. The number of fractures included in the rose diagram for the F1 population alone is 80 (the radial scale is 0.25 mm per fracture), giving a mean direction of 9.6°. The number of fractures included in the rose diagram for the Kelduhverfi area is 182 (the radial scale is 0.2 mm per fracture), giving a mean direction of 15.4°.

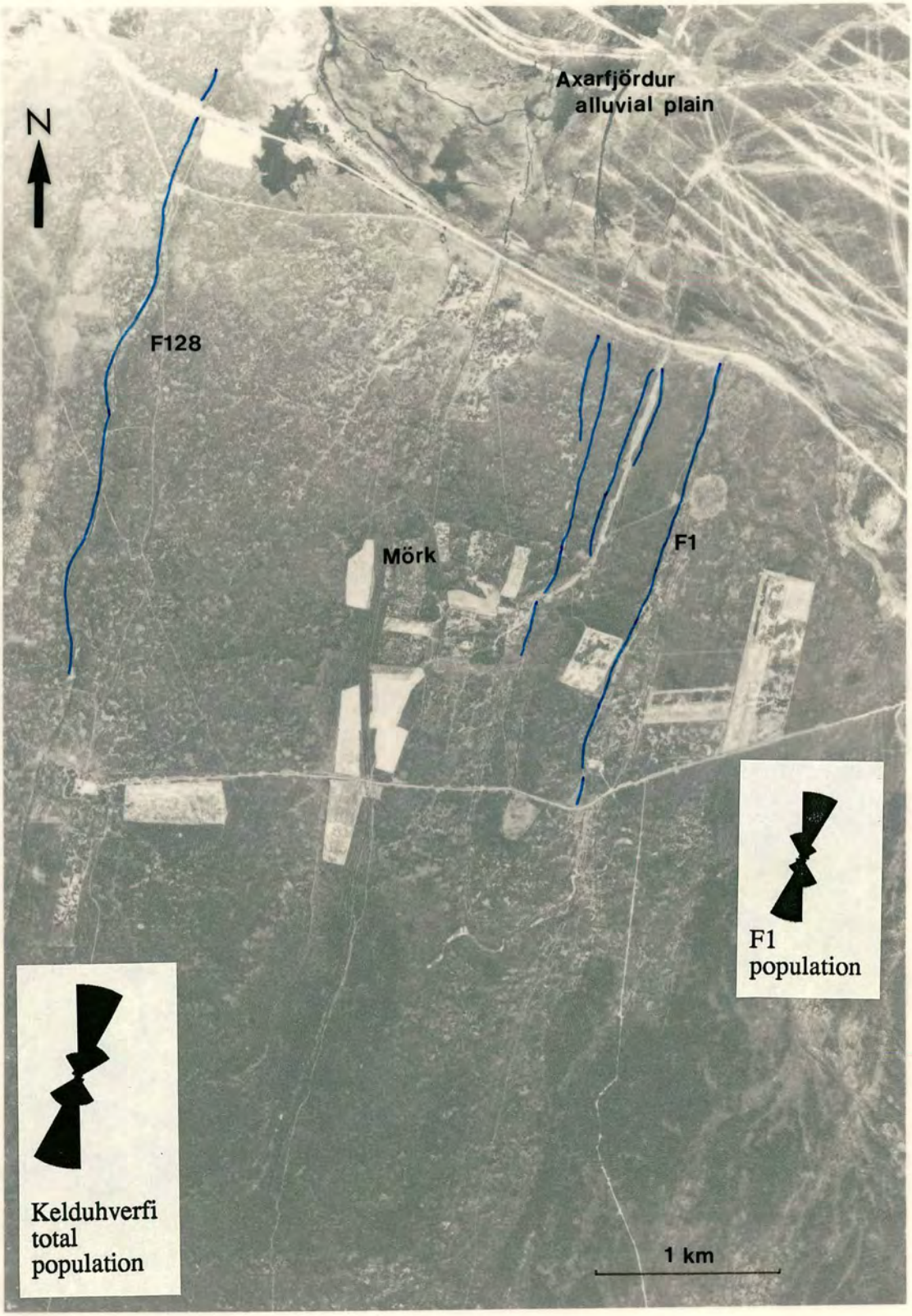
Axarfjördur
alluvial plain
N
F128
Mörk
F1
F1
population
Kelduhverfi
total
population
1 km

at each end, shown in figure 5.5(a), to 0 metres near the centre of its length where the deformation appears to be purely tensile, figure 5.5(b). One other fracture of the population may be termed a normal fault, since it showed a throw of 0.4 m down to the east. All the other fractures in the F1 population were pure tension fractures. This is illustrated very well by one fracture that was seen to follow the weakness of the columnar jointing, figure 5.6(b). A pure tensile movement is evident from the position of the blocks. A small scale transform movement between the blocks of the columnar jointing may also be observed. The associated fractures in this population varied in length from 0.2 m to 300 m. Figures 5.6 (a) and (c) show examples of intermediate scale tension fractures from the F1 population. Figure 5.6(d) shows the smallest scale of fracture that it was possible to measure. A small recent opening of 3 mm was evident. All the fractures measured were vertical or near vertical. The orientations of the fractures are illustrated in the rose diagrams in the inset of figure 5.4. The mean direction is 09.6°E. This fits in very well with the orientation of 10°E that is observed for the spreading ridge (Björnsson, 1985). A minority of fractures were observed to have a trend perpendicular to this direction, and commonly showed a high width to length ratio. Some shear movement may have been involved.

To provide a direct comparison with the laboratory results, the length distributions from the fracture populations are plotted on log-log axes. Figure 5.7(a) shows the length distribution of fractures of the F1 population. The distribution does not appear to be well fit by a single power-law, since there appear to be peaks in the data that prevent a good single straight line fit. This may be real, or more likely may be due simply to the sampling technique. Three peaks are evident, at around 1 m, 25 m and 500 m. This indicates possible preferential measuring of fractures at these scales. Furthermore, the slope D from the discrete data of 0.37 ± 0.06 is also too low for a fractal nature is to be assigned to this population, since a fractal distribution for one-dimensional fracture traces strictly requires $D > 1$ (see section 1.2).

Figure 5.5 Field photographs of the F1 major fracture, Kelduhverfi area. Both photographs were taken looking north.

a. F1 illustrating normal fault morphology, with a throw of 11 m down to the west. The width of the fault at this locality is 17 m. The pale area in the centre of the photograph is water at the bottom of the fault.

b. Further to the south, approximately at the centre of its length, F1 shows no throw. Here it is vertical and has the appearance of a tension fracture. The width of the fault at this locality is 17 m.

a

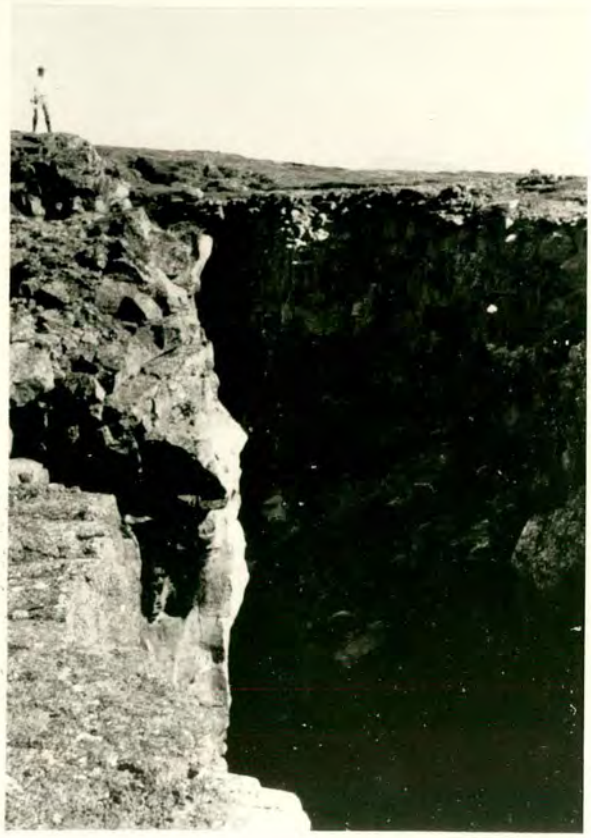

b

Figure 5.6 Field photographs of tension fractures measured in the Kelduhverfi area.

a. Relatively large intermediate scale fracture of measured length 21 m.

b. Intermediate scale fracture of length 2.7 m and width 0.12 m.

c. Relatively small intermediate scale fracture of length 1.3 m.

d. Small scale fracture of length 0.4 m.

a

b

c

d

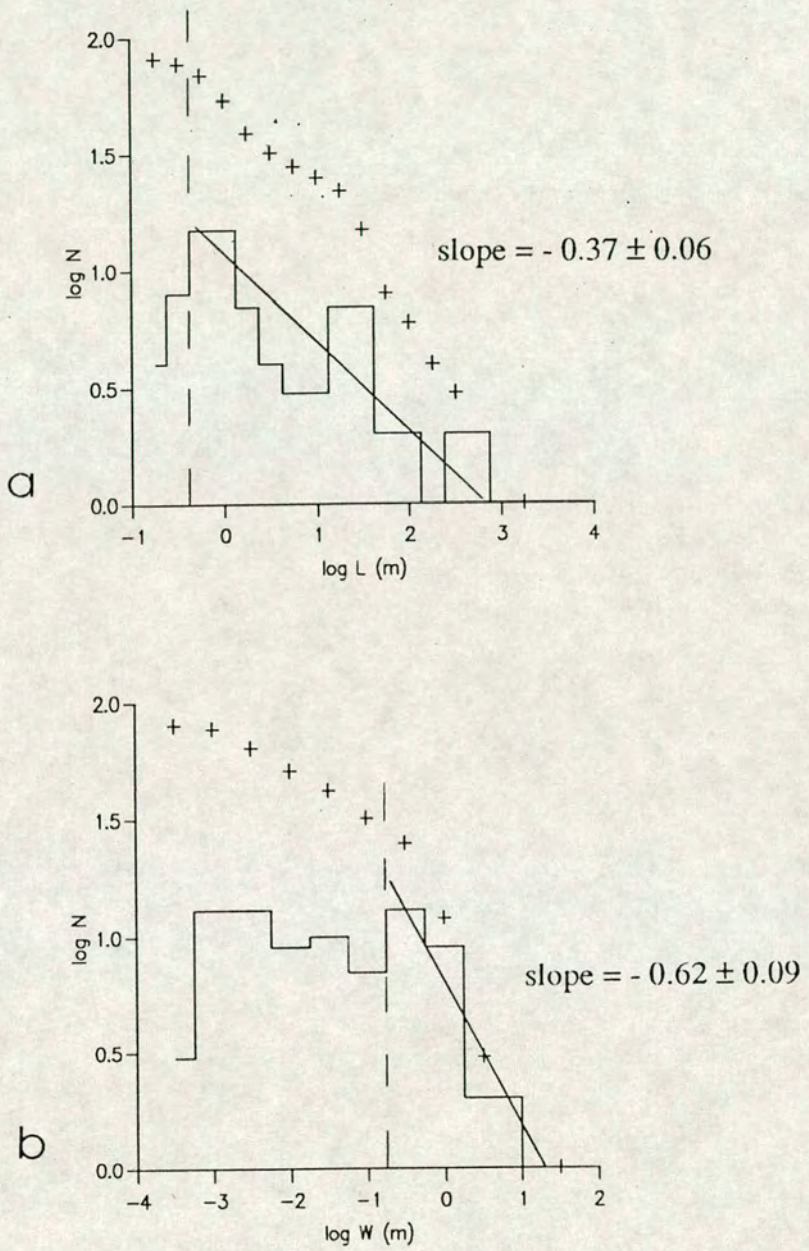

Figure 5.7 Results from the F1 fracture population (staircase - discrete data; crosses - cumulative data).

a. Length frequency distribution. Approximate straight line power-law gives slope of 0.37 ± 0.06 (from the reduced major axis).

b. Width frequency distribution. Shows a power-law distribution above a width of 0.17 m, giving a slope of 0.62 ± 0.09 (from the reduced major axis).

Figure 5.7(b) shows the frequency distribution of fracture widths from the F1 population. This illustrates a power-law with a slope of 0.62 ± 0.09 in the data above a width of 0.17 m. Below this the data levels out. The longer fractures tended to be wider than the shorter fractures implying a tendency to self-similarity. The relation between fracture length and width for the fractures of the F1 population is shown in figure 5.8. The data plot with a distinct break in slope at a length of 3 m. At lengths less than 3 m the data show a linear relation with slope of 2.16 ± 0.23 (with a significant positive correlation coefficient $r = 0.66$). Above this limit, the data plot with a slope of 0.88 ± 0.08 (where $r = 0.86$). This result is discussed further in the discussion section 5.5 of this chapter. Several short fractures showed uncommonly large widths (width:length ratio of 1:20), possibly due to some shear movement.

A rose diagram is also included in figure 5.4 to illustrate the orientations from all the fractures measured in the Kelduhverfi area. The total number of fractures was 182, and the mean orientation was 15.4°E.

The accumulated length measurements for the total Kelduhverfi population are plotted in figures 5.9 (a) and (b). The data plot with a distinct break in slope at around 22 m. If two separate trends are considered, as shown in figure 5.9(a), then the data above 22 m show a straight line power law distribution, with a slope of 0.65 ± 0.06. An undercounting of fractures with a length less than 22 m may be inferred, due to either poor exposure or the volume effect of the smaller fractures not reaching the surface. Alternatively, a lower limit may be drawn at the peak of 0.3 m length, figure 5.9(b), and the average slope is then 0.41 ± 0.04. However, this slope from the discrete data does not correspond well with the cumulative data. Whichever method is used, the slope obtained from the length distribution is too low for a fractal set to be defined, (since $1 < D < 2$, as described in section 1.2).

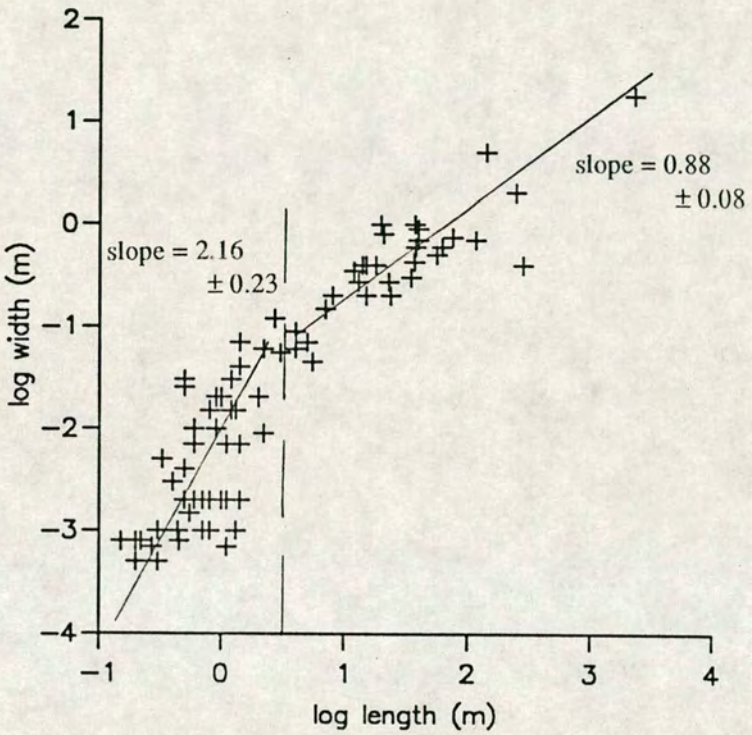

Figure 5.8 F1 population; fracture length-width relation plotted on log-log axes. A break of slope occurs at a length of 3 m. Above the break, the slope is around 1.0; below the break, the slope is around 2.0.

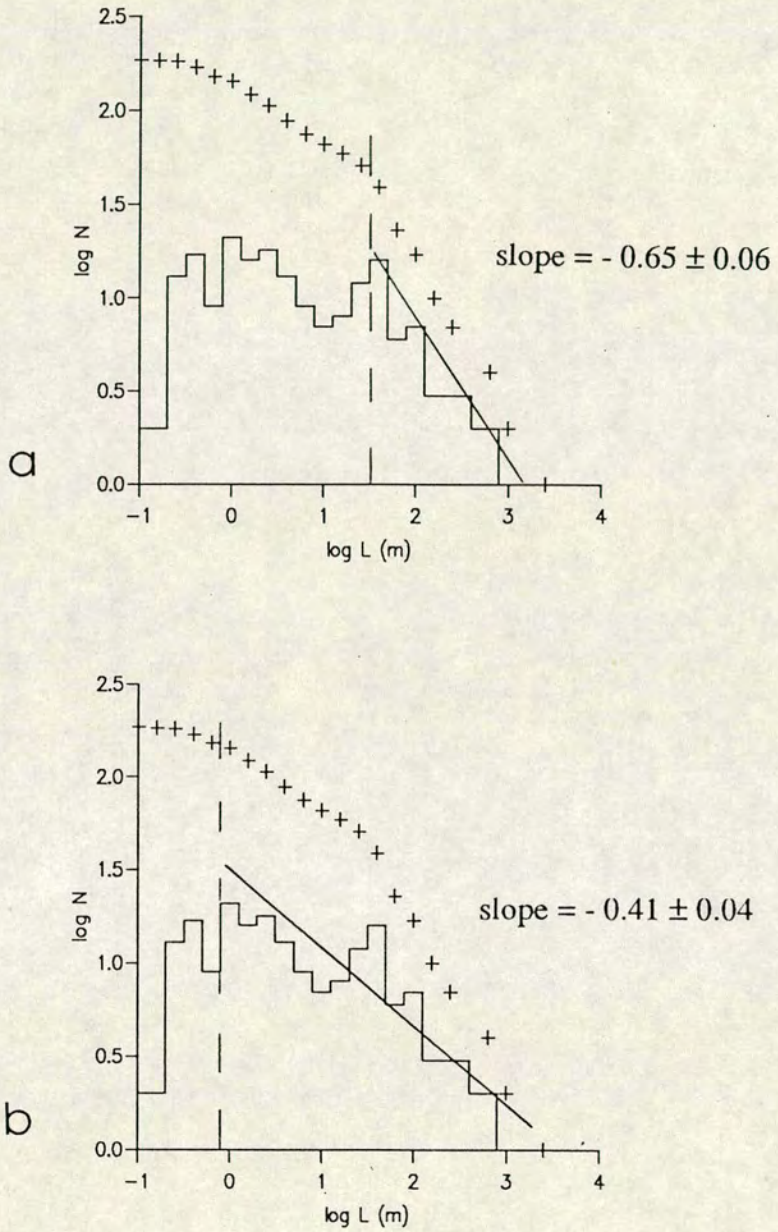

Figure 5.9 Length-frequency distribution of all the fractures measured in the Kelduhverfi area. Two possible distributions are evident:

a. Using a cut-off of 22 m, the data plots as a good straight line, with slope of 0.65 ± 0.06 (from the reduced major axis).

b. If a lower cut-off of 0.3 m is used, a slope of 0.41 ± 0.04 is found (from the reduced major axis).

Mývatn

At Mývatn to the south, marked on figure 5.2, the lavas are also basaltic pahoehoe, but here they are younger and from the Krafla centre. Fractures in this area were reactivated and created during 1984. The main fractures measured were F187 and F217, (which together form an almost continuous fracture, named Grjótagjá), marked in blue on figure 5.2 and shown in detail in figure 5.10, (from the aerial photograph). Several smaller fractures and active fissures were also measured in this area.

The total number of fractures measured in this population was 48. Both F187 and F217 are large scale tension fractures of length around 100 m and width 2 m, that show no throw, as illustrated in figure 5.11(a). The associated fractures in this population varied in length from 0.4 m to 14.8 m, and are significantly less than those of the F1 population of Kelduhverfi. This follows since the main fracture in this population is much shorter than F1. Figure 5.11(b) shows an example of the smaller scale fractures measured in this population. All the fractures measured were vertical or near vertical. The orientations of the fractures are illustrated in the rose diagram, in the inset of figure 5.10. The mean direction is 17.23°E, still consistently parallel to the orientation of the spreading ridge and fissure zone.

The length distribution from the F187/F217 population is shown in figure 5.12(a). This plots as a good straight line power-law with a slope of 1.14 ± 0.19, with a lower limit of 1.2 m. This suggests that this fracture system is consistent with a fractal set.

The width distribution, figure 5.12(b), also shows a good straight line with a slope of 0.61 ± 0.1, for data above 0.03 m. The length-width relation for fractures of

Figure 5.10 Aerial photograph of the Mývatn area, showing the main fractures measured in blue. The rose diagram illustrates the fracture orientations measured from the F187/F217 population. The number of fractures included in the rose diagram is 48 (radial scale of 0.35 mm per fracture), giving a mean direction of 17.2°.


N
F217
F187
Mývatn
Hverfell
1 km

Figure 5.11 Field photographs of fractures in the Mývatn area.

a. Major tension fracture, F187 showing no throw.

b. Associated intermediate scale tension fracture of length 2.3 m.

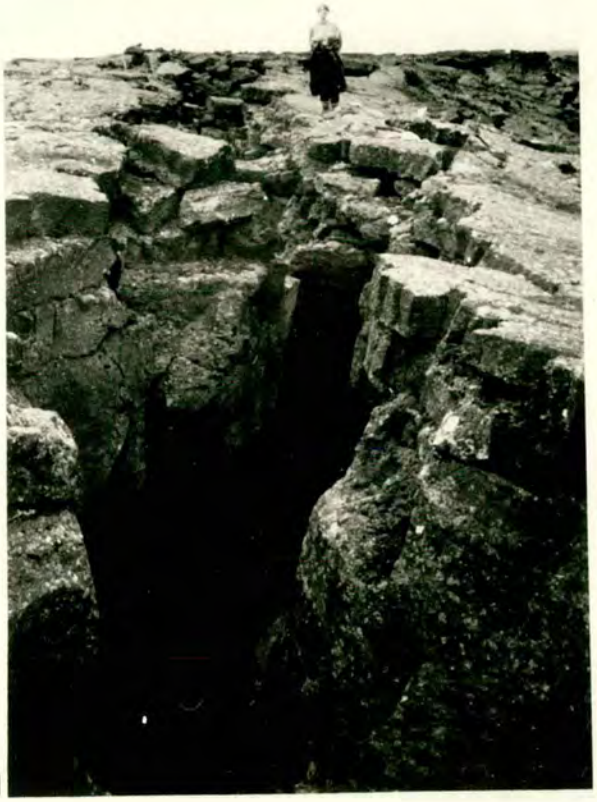

a

b

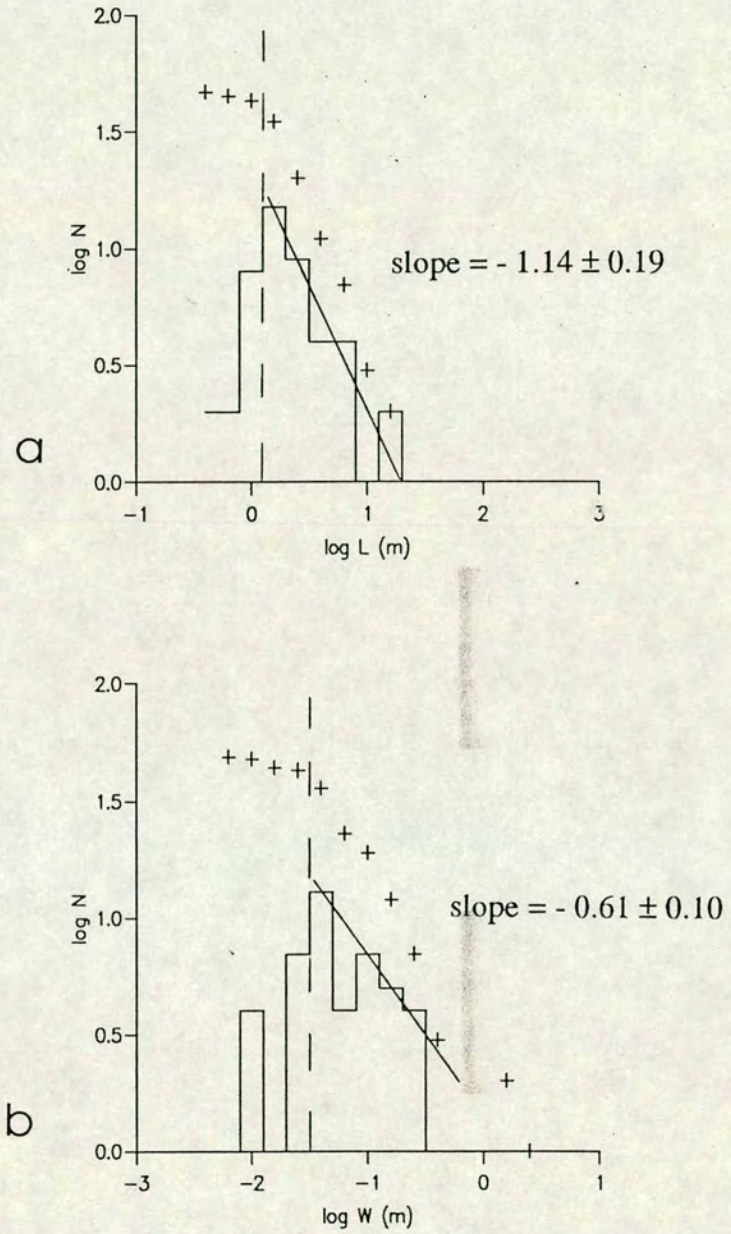

Figure 5.12 Results from the F187/F217 fracture population.

a. The length-frequency distribution plots as a good straight line, with a slope of 1.14 ± 0.19 (from the reduced major axis), using a lower cut-off of 1.2 m.

b. Width-frequency distribution, giving a slope of 0.61 ± 0.1 (from the reduced major axis), for data above 0.03 m.

the Mývatn population is shown in figure 5.13. This data plots with a similar trend to that of the Kelduhverfi F1 population data, i.e. a break of slope is evident at a length of 3m. Below this, the data plots with a slope of 1.53 ± 0.17 (where $r = 0.75$); above 3 m the data plots with a slope of 0.91 ± 0.18 (where $r = 0.78$). This result is also discussed in section 5.5.

In summary, the tensile fracture populations observed in north east Iceland appeared to provide a potentially good natural analogy to the artificial microfracture systems produced in the laboratory test specimens. The measured length distributions from the Kelduhverfi area plotted as approximate power-law sets, where the average exponent D was 0.6, i.e. lower than the lower fractal limit of 1.0. The length distribution from the Mývatn area plotted as a good straight line power-law, with exponent $D = 1.14$, consistent with a fractal set. The fracture length-width relations from both sets of data appear to show two distinct slopes, of 1.0 and 1.5 - 2.0. The break in slope appears to occur at around 3 m in both cases.

5.4 Natural seismicity of north east Iceland

As well as providing an area of natural tensile fracture for structural analysis, the Krafla Fissure Swarm also presented the chance to obtain natural seismicity data from the recent tectonic events. Thus producing a natural comparison for both the structure of microfractures and AE microseismicity from the laboratory tests.

The seismicity monitored in the Krafla Fissure Swarm since 1975 has been summarised by Einarsson (1991). Several characteristic types of seismic activity occurred at different stages in the rifting episode. Inflation and deflation earthquakes occured in the region of the Krafla magma chamber and caldera. Shortly after a deflation of the magma chamber, lateral magma flow is proposed to have produced a

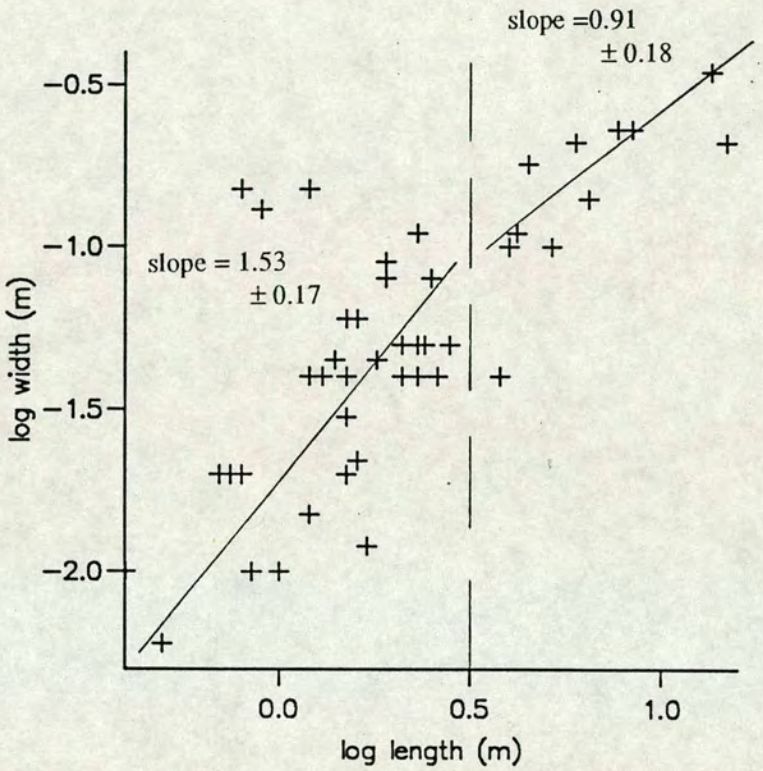

Figure 5.13 Mývatn population; fracture length-width relation plotted on log-log axes. A break of slope occurs at a length of 3 m. Above the break, the slope is around 1.0; below the break, the slope is around 1.5.

propagating dyke. Rifting earthquakes were observed to migrate away from the caldera and along the fissure swarm, accompanying the faulting above the dyke. The rifting earthquakes were usually of a magnitude less than 4.

On 20th December 1975, the recent rifting episode began with a small eruption near Leirhnjúkur, at the centre of the Krafla caldera. This was accompanied by a strong seismic tremor and swarm of earthquakes, within the area of the fissure swarm. The epicentres were observed to migrate in a few hours away from the caldera to the north coast at Axarfjördur (Tryggvason, 1984). During this activity, fissures were seen to open in the north. Processed seismic data for the Kelduhverfi area has not been available. However, some preliminary data on earthquake events and magnitudes has been obtained from the preliminary catalogue of current events, Skjálftabréf (in Icelandic). From 2nd December 1975 to 2nd January 1976, the Kelduhverfi area experienced three events of magnitudes 1.9, 4.4 and 4.7. The strongest event, of magnitude 6 - 6.5, monitored during the early activity occurred on 13th January 1976 at Kópasker, north east of Kelduhverfi.

A rifting event also occured in Kelduhverfi in March 1978 with new fissures opening (Tryggvason, 1984), although no magnitude data are available.

In September 1977, a deflation and associated rifting event affected the southern part of the fissure swarm, from Krafla southwards to near Mývatn. Seismicity from this event has been analysed, and provides evidence for the lateral migration of magma along the fissure swarm (Brandsdóttir and Einarsson, 1979). More significantly for this study, a magnitude-frequency distribution for this earthquake sequence has been published, and is shown in figure 5.14(a). This distribution shows a distinct non-linearity. This was interpreted as a superposition of two earthquake sequences with different b-values (Brandsdóttir and Einarsson, 1979).

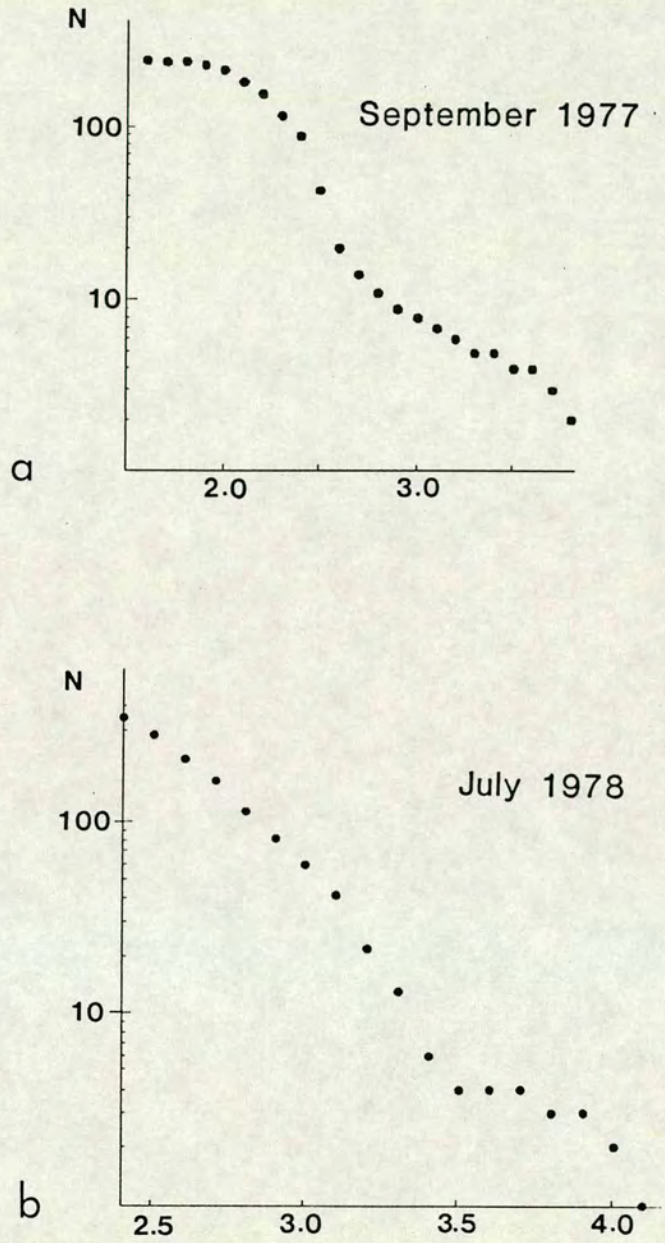

Figure 5.14 (a) Magnitude-frequency distribution for the earthquake sequence of September 1977, Krafla Fissure Swarm (Brandsdóttir and Einarsson, 1979). The data can be fit by two straight lines corresponding to seismic b-values of 3.0 for the smaller events and 0.6 for the larger events.

(b) Magnitude-frequency distribution for the earthquake swarm of July 1978, Krafla Fissure Swarm (Einarsson and Brandsdóttir, 1980). Below a magnitude of 3.5, the seismic b-value is 1.7 ± 0.2.

The authors proposed that the high b-value of about 3 indicates a low effective stress, and that an isolated event associated with a high stress build up produced the lower b-value of about 0.6. The work presented in this thesis and by Meredith et al. (1990) would suggest that this interpretation, though broadly correct, might be better cast with stress concentration or stress intensity replacing the stress alone.

A further magnitude-frequency distribution has been published for a later deflation episode that occured in July 1978 (Einarsson and Brandsdóttir, 1980). This event affected the northern part of the fissure swarm, although it did not extend to the coast at Kelduhverfi. This distribution, shown in figure 5.14(b), also shows a break from linearity, at a magnitude of about 3.5, although it is less pronounced than that of the 1977 event. A seismic b-value of 1.7 ± 0.2 was assigned to this earthquake swarm for events with magnitudes less than 3.5 (Einarsson and Brandsdóttir, 1980).

If it is assumed that we can apply the simple theoretical relation $D = 2\,b$ (see section 1.5) to these data sets, then the seismicity data imply that length distribution exponents (D) lies in the range 1.2 (1977), 3.4 (1978) to 6.0 (1977). A fractal set should by definition be in the range $1 < D < 2$ or 3, and so only the lower b-value of the 1977 data is consistant with a fractal interpretation. This result may be complicated by the changes in slope of the magnitude-frequency data, as shown in figure 5.14. The moment-magnitude relation of equation (1.16) may be assumed, with constants $c = 1.5$ and $d = 9$ (Kanamori and Anderson, 1975) to find the moment from the magnitudes at the observed breaks in slope (figure 5.14). Using the assumption of a circular fault, equation (1.14), the length of fracture may then be found from the moment. Using these assumptions, a magnitude of 3.5 is found to correspond to a fault length of 300 m, and this is approximately equivalent to the observed peak in the length-frequency data of figure 5.7(a) at 500 m. A magnitude 2.0 corresponds to a fault length of 50 m, which may roughly correspond to the peak of 25 m of figure

5.7(a). However, the constants assumed in this calculation are very approximate and so the evidence for any relation between the seismicity data and the measured length distributions can only be tentative.

5.5 Discussion

The intention of this field study was mostly just to provide a natural extension to the experimental work, to illustrate that the results from the artificial fracture in the laboratory specimens did have some real relation to the natural fractures that were being simulated. The field areas chosen, in the Krafla Fissure Swarm of north east Iceland, were ideal for this purpose. The fractures were shown (apart from two specific examples) to be pure tension fractures due to the combination of an extensional tectonic stress from spreading plate motion, and high pore pressures from injected magmas and their volatile components.

The length distributions measured from the fracture populations showed a linear power-law relation, although only the population from Mývatn could be referred to accurately as a fractal set, with a power-law exponent D = 1.14. Gaps in the field data from the Kelduhverfi area may have been due to sampling problems, vegetation cover or an abundance of small fractures beneath the ground surface.

An additional inevitable problem was that of fracture length accumulation over time. The rift zone in NE Iceland has experienced many phases of rifting. In each episode, many of the existing fractures and fissures are reactivated and opened further, adding to their length and width. Even new fractures may be opened over several events within a single episode. Thus, any measurement is likely to overestimate increments of natural fracture unless it is measured contemporaneously with the activity and seismicity (as is the case in the laboratory experiments).

However, a significant result was found from the length-width relations measured for both fracture populations. If a system is scale invariant, the length and width dimensions should scale as 1:1, with a slope of 1.0 on log-log axes. An ongoing debate concerns this relation with respect to fault growth models based on length-slip data, (Scholz and Cowie, 1990; Walsh and Watterson, 1991; see section 1.2). The result from the present study, plotted in figures 5.8 and 5.13, indicates that a limit to scaling may exist, in this case at 3 m. This produces a non-fractal distribution below the limit, giving a relation of width ~ $L^{1.5 \text{ to } 2.0}$; and a scale-invariant, i.e. fractal, distribution above the limit, producing a relation of width ~ L. This suggests that the two competing models mentioned above may simply be observing different parts of the same system. The change in scaling is evident in this data since the data set spans a wider length range than the data used in previous models.

Another area of difficulty involved the problems of assigning seismic data to specific fractures, or even areas of fracture. An ideal experiment would involve contemporaneous field mapping and seismic monitoring during or immediately after an active episode.

In summary, this study has illustrated that tensile fracture associated with seismic emission does occur naturally, and with similar populations to those produced in the laboratory specimens. Therefore, the laboratory tests produce a good analogy to natural fracture in the earth.

Chapter 6 Conclusions and Discussion

The work completed for this thesis has included a series of tensile fracture mechanics laboratory tests, subsequent data analysis including AE and structural data collection and interpretation, and a field study of natural tensile fractures. The main objectives of the work were to study the effects of fluid-rock interaction on tensile subcritical crack growth; to test the scale invariance of tensile fracture systems; to test the hypothesis of a relationship between the scaling parameters of seismicity and structure using the laboratory results; and to test the relevance of these laboratory studies to interpreting natural tensile fracture in the earth.

The preceding chapters have described the experimental technique, laboratory AE and structural results - including a synthesis of these results, and the natural fracture systems observed in the field. Although separate discussions have been given concerning these results, the purpose of this chapter is to summarise the final conclusions found from these studies, and to discuss these results in a wider context. A brief description of the major problems encountered is also given, together with recommendations for future work arising from this project.

6.1 Conclusions

The following conclusions may be made from the results obtained during this study.

Acoustic emission microseismicity is seen to reflect microcrack propagation in the laboratory. Crack growth in a 'dry' environment is characterised by bursts of high amplitude AE events, representing large increments of crack growth; whereas crack propagation in 'wet' conditions is more stable producing fairly uniform lower amplitude AE, from small increments of crack growth.

AE b-values calculated for the microseismicity monitored during periods of constant stress intensity (K_I) are seen to vary depending upon fluid content at the crack tip. Fluid presence, therefore, has a first order influence on AE seismicity during tensile crack growth, inferred to be due to the activation of the stress corrosion mechanism. The greater the fluid-rock interaction, the greater the relative proportion of smaller seismic sources (thus producing a higher b-value). The AE b-values correlate negatively and linearly with the normalised stress intensity (K_I / K_{IC}). This implies that the greater the stress concentration, the greater the relative proportion of larger seismic sources.

At low K_I and low rupture velocity, the mechanism of crack propagation is highly sensitive to fluid presence and environmental conditions. At higher K_I and rupture velocities close to dynamic, fluid movement to the crack tip region may be transport limited and hence the chemical environment of less influence to the crack propagation.

The above results appear to be independent of rock type and specimen size for the limited range tested, implying a type of 'universality' to the fluid-rock system once the results are normalised by the fracture toughness.

Following crack propagation, a system of microfractures around the main macrocrack is evident on the polished undersurface of the test specimens. Fluid presence is observed, from qualitative differences in the fracture patterns, to have a first order effect on the geometrical nature of these fracture systems. Specimens tested in water show less angular, more irregular main cracks characterised by a number of bifurcation points, producing a greater relative proportion of subsidiary microcracking. Tests that were stopped before failure, but after significant microcrack growth, produced macrocracks that terminated within the middle third of the specimen length. A damage zone of isolated microcracks was evident ahead of the main crack in these specimens. Although, no regular intense zone of microcracking was observed, this may be termed a macrocrack 'process zone', produced due to the tensile stress field ahead of the main crack tip. The power-law microcrack length distribution exponent D was found to be the most suitable diagnostic quantitative measure of differences in the structure of tensile microfracture systems produced during tensile subcritical crack growth under different conditions. The length distribution exponent D correlates positively with the AE b-value, as predicted from the dislocation model of a seismic source. This relation implies that small fractures produce low amplitude AE. Rock type and specimen size appear to have a second order effect on this relation.

Observations from the Krafla Fissure Swarm, north east Iceland, show that tensile fracture associated with seismic emission does occur naturally, and in similar populations to those produced in the laboratory specimens. Length distribution measurements of the populations examined show a linear power-law relation. Length-

width relations measured from the natural fracture populations suggest a lower limit to the scale invariance of such fracture systems.

6.2 Discussion and recommendations for future work

The main body of work carried out for this thesis has involved the laboratory experiments and subsequent analysis of the data produced. Therefore, the choice of laboratory test was of considerable importance. The double torsion test provided the most suitable specimen geometry to allow the post-test examination of the structural system of microfractures. The constant displacement rate method allowed application of a constant load, and hence stress intensity, providing uniform conditions over much of the specimen. Therefore, the loading conditions were controlled, and reduced to one parameter, K, for each test.

The validity of the experimental method was tested using a compliance calibration that produced an experimentally derived value within 20% of that derived from theory, thus confirming the validity of the test set-up. Subcritical crack growth indices obtained from the stress intensity and rupture velocity results also compared well with previous experimentally derived values (Atkinson and Meredith, 1987b).

The program of tests carried out was slightly limited due to the time involved in specimen preparation and availability of the test equipment (at University College, London). Since the controlling variables were displacement rate (and hence stress intensity) and fluid presence, a programme that included a range of displacement rates in different environmental conditions (including 'dry' and 'wet'), with several repeat tests of each type, was carried out. With more time, more repeat experiments should be carried out and a more complete programme using the Ballachulish granite specimens would be valuable. A further program of tests might include a more extensive range

of rock types, for example basalt, or metamorphic rocks containing different grades of tectonic fabric to test the effect of fabric and preferred orientation on crack propagation, up to the limit where the crack is 'stopped' and diverted along the weakness. Variations in the environmental test conditions may also be added to the test program, using heated water to test the effects of temperature, or different fluids, for example, brine.

The results and conclusions concerning the AE and stress intensity have been established in previous experimental work (for example, Meredith and Atkinson, 1983; Main et al., 1990). Therefore, the results found from the present experimental program both confirm the previous conclusions of fluid influence, and also validate the present results in comparison to previously published work. (The new aspects of the present work relate to the establishment of similar properties for structural scaling exponents, and their relationship to the seismological parameters).

The main problem encountered with the monitoring of AE was that of background noise during the 'wet' tests, (sections 2.4 and 3.1.2). An attempt was made to filter out the noise using an active high pass filter (of 300 kHz) in several of the tests. This did reduce the background noise slightly. In future work, more sophisticated equipment may be available to cancel out the vibrations from the servo-valve, thus alleviating the problem.

Another area of future work may be to use multiple transducers to investigate AE source locations within the specimen. It may then be possible to assign AE events to periods of crack growth along the specimen, and also to test the amount of microcracking ahead of the propagating main crack tip. It would also be useful to record the complete waveform of the AE events, as well as the parametrics such as

amplitude. This would allow direct examination of the type of emissions produced during crack growth.

The results concerning the structural analysis of the fracture patterns from the double torsion specimens are specific to this project. Since such analysis had not been carried out before, techniques of observation and measurement had to be assessed. Optical microscopy, after enhancement of the undersurface by a dye penetrant, proved to provide good images of the microfracture systems to be analysed by hand. Digital image processing of the fractures directly from the specimen was considered, however a major problem in programming a machine to distinguish between fractures and crystal grain boundaries seemed to produce too many complications. This may be an area for future work, using the specimens that have already been tested.

Testing the scale invariance of fracture systems at laboratory scale proved to be inconclusive, since the microfractures did not show any determinable width to test the length-width relation. It may be suggested that the systems appear to be scale invariant since the small granodiorite specimens show a similar structure to the larger granite specimens. However, this is merely a subjective conclusion at this stage, but worthy of further investigation.

The quantitative analysis of the fracture patterns using the various concepts of fractals produced varying results. The box-counting technique that has frequently been used in the literature (for example, Hirata, 1989; Vignes-Alder et al., 1991) appeared to give a single result depending on box-size, regardless of stress intensity, environmental conditions or rock type, (section 3.2.2) and consequently was discarded as a useful method in this study. The microcrack length distribution exponent, although not strictly a Hausdorff-Besicovitch fractal dimension, was found to show significant variation between specimens depending on the test conditions, and

so was found to be the most suitable measure of differences in the structure. However, this method also produced problems, specifically in the fine grained granodiorite specimens, where a single fracture pattern represented only a fraction of the specimen length. It was found that the length distribution exponent varied considerably with position along the macrocrack in some specimens (see appendix E). This may be due to the natural inhomogeneity of rock, or gross fluctuations in applied load due to sudden crack extension increasing the compliance of the specimen. Those tests with approximately constant load application showed less variation. A number of multiple fracture pattern analyses from single specimens produced single average length distribution exponents from an increased data set, representing more of the macrocrack length. It is suggested that this more detailed process would substantially improve the quality of the structural analysis of all the specimens. For the present study, time was a limiting factor.

Further work could be carried out by digitising the tracings made from the fracture systems in this study. A Fourier Transform could then be applied to examine the geometry of the fracture system in the space domain. If the fracture pattern is digitised, a clustering analysis may also be carried out. This is an alternative method of measuring a dimension D_{CL} that considers the positioning of the fractures in space, (Henderson et al., 1992). It has recently been suggested that scaling laws may be used to relate the various 'fractal' dimensions such as D_{BC}, D_{CL} and D, (Davy et al., 1992). Although not part of the original scope of this project, this hypothesis may be tested using data from the present study, once the fracture patterns are digitised. Once again, lack of time has prevented this work at present, and so it is suggested as a piece of future work.

The observation that the length distribution exponent D is positively correlated to the AE b-value is possibly the most significant result from this study.

This implies that small microcracks result in low amplitude AE. Although this relation may seem self-evident, and has often been inferred in previous work (for example, Main et al., 1990), this is the first time that the relation has been directly and quantitatively examined for a single increment of crack growth in time in a controlled environment. Therefore, this result is significant to the justification of any of the models that infer a linear relation between D and b. Further tests and analyses, including structural analysis of an increased proportion of the specimen length, may be required to establish the precise relation more firmly. Further future work may also establish the exact nature of the second order effect of rock type (and grain size) and specimen size on the relation between D and b.

The relation between the two-dimensional length distribution exponent D_A and the three-dimensional volume exponent D_V remains inconclusive. It is evident that an anisotropic stress field would result in an anisotropic array of distributed fractures, thus producing self-affine scaling, i.e. a different fractal scaling in different directions. As a result, field results (D_A) from a two-dimensional outcrop or map represent only one possible scaling value and should not be treated as self-similar Hausdorff-Besicovitch dimensions in order to infer a volume distribution (D_V).

Although a relation between the length distribution exponent D and stress intensity K_I should be expected, (since K is related to the AE b-value, and the b-value is related to D), a significant correlation cannot be inferred from the present results. This may be due to the limited range in K_I studied, or the limited range and number of fracture sizes which could be observed (see appendix E). A different experimental procedure may be able to extend both ranges, but with attendent increased difficulty in experimentation and higher optical resolution.

The intention of the field study carried out as part of this project was to examine a natural occurrence of tensile fracture to validate the assumption that artificial fracture in the laboratory provides an analogy to natural fracture in the earth. The Krafla Fissure Swarm of north east Iceland provided an excellent field area, where pure tensile fracture populations in thick basalt lava flows showed that the laboratory specimens do indeed provide a good analogy to natural tensile fracture. Length distribution measurements of the fracture populations show some linear power-law relations, although the exponents were usually lower than those obtained from the laboratory specimens. More extensive measurements to produce a larger data set may improve the distributions. An alternative method would be to use aerial photographs or satellite images, to map the large scale fractures in the whole fissure swarm. Digital processing of such natural fracture patterns could then be carried out in a way similar to that suggested above for the laboratory specimens.

The most significant result from the field work was found from the length-width relations measured from the natural fracture populations. A distinct break in slope was evident between two scaling factors, producing a non-fractal distribution below the limit (at 3.0 m), and a scale invariant fractal distribution above the limit. This result has significance to fault growth models (Walsh and Watterson, 1988; Scholz and Cowie, 1990; Marret and Allmendinger, 1990, 1991; Walsh et al., 1991; Cowie and Scholz, 1992a, b) that assume a constant scaling factor in the accumulation of fault length, since it suggests that a change in scaling occurs at some critical point. The change in scaling is evident in the data from this study since the measurements taken span a wider range of scale than the data used in any previous models. This is because the aim of the fieldwork was to measure all the fractures at all scales in a single area. Further work to test this relation may involve detailed measurement of the large fracture itself, such as a width profile along its entire length, to examine the nature of the accumulated fracture growth.

Originally it was also hoped to examine natural seismological data from the same field areas. However, this proved to be impossible with the available data. It is suggested that an ideal experiment, as an analogy to the laboratory tests, would involve contemporaneous field mapping of tectonic fractures and seismic monitoring during or immediately after an active episode, in an area such as the Krafla Fissure Zone.

In summary, field studies have shown that the artificial fractures produced in the laboratory specimens do provide a good analogy to natural tensile fracture as it occurs in the earth. Therefore, the results found from the laboratory experiments, concerning stress intensity, environmental conditions, microseismicity and structure, may be applied to natural fracture systems. With all their complexity, fracture systems in the laboratory and the earth do appear to have a degree of universality after appropriate consideration for changes in scaling and fracture toughness.

References

Aki, K. 1965. Maximum likelihood estimates of b in the formula log N = a - bm and its confidence limits. Bulletin of the Earthquake Research Institute of Tokyo University. **43**, 237-239.

Aki, K. 1981. A probabilistic synthesis of precursory phenomena. In: Earthquake prediction: an international review (edited by Simpson, D. W. & Richards, P. G.). American Geophysical Union, Maurice Ewing series, **4**, 566-574.

Aki, K. & Richards, P. 1980. Quantitative seismology: theory and methods. Freeman, San Fransisco.

Anderson, E. M. 1951. The dynamics of faulting. Oliver and Boyd, Edinburgh.

Anderson, O. L. & Grew, P. C. 1977. Stress corrosion theory of crack propagation with application to geophysics. Rev. Geophys. Space Phys. **15**, 77-104.

Atkinson, B. K. 1979. A fracture mechanics study of subcritical tensile cracking of quartz in wet environments. Pure Appl. Geophys. **117**, 1011-1024.

Atkinson, B. K. 1982. Subcritical crack propagation in rocks: Theory, experimental results and applications. J. Struc. Geol. **4**, 41-56.

Atkinson, B. K. 1984. Subcritical crack growth in geological materials. J. Geophys. Res. **89**, 4077-4114.

Atkinson, B. K. 1987. Introduction to fracture mechanics and its geophysical applications. In: Fracture mechanics of rock (edited by Atkinson, B. K.). Academic Press, London, 1-26.

Atkinson, B. K. & Meredith, P. G. 1987a. The theory of subcritical crack growth with applications to minerals and rocks. In: Fracture mechanics of rock (edited by Atkinson, B. K.). Academic Press, London, 111-166.

Atkinson, B. K. & Meredith, P. G. 1987b. Experimental fracture mechanics data for rocks and minerals. In: Fracture mechanics of rock (edited by Atkinson, B. K.). Academic Press, London, 477-525.

Bailey, E. B., Clough, C. T., Wright, W.B., Richey, J. E. & Wilson, G.V. 1924. Tertiary and Post-Tertiary Geology of Mull, Loch Aline and Oban. Memoirs of the Geological Survey of Scotland.

Björnsson, A. 1985. Dynamics of crustal rifting in NE Iceland. J. Geophys. Res. **90**, 10,151-10,162.

Björnsson, A., Saemundsson, K., Einarsson, P., Tryggvason, E. & Grönvold, K. 1977. Current riftin gepisode in north Iceland. Nature. **266**, 318-323.

Björnsson, A., Johnsen, G., Sigurdsson, S. and Thorbergsson, G. 1979. Rifting of the plate boundary in North Iceland 1975-1978. J. Geophys. Res. **84**, 3029-3038.

Brandsdöttir, B. and Einarsson, P. 1979. Seismic activity associated with the September 1977 deflation of the Krafla central volcano in North Eastern Iceland. J. Volc. and Geoth. Res. **6**, 197-212.

Charles, R. J. 1958. Static fatigue of glass. J. Appl. Phys. **29**, 1549-1560.

Cowie, P. A. & Scholz, C. H. 1992a. Physical explanation for displacement-length relationship for faults using a post-yield fracture mechanics model. J. Struc. Geol. (in review).

Cowie, P. A. & Scholz, C. H. 1992b. Growth of faults by accumulation of seismic slip. J. Geophys. Res. **97**, 11085-11095.

Cox, S. J. D. & Scholz, C. H. 1988. On the formation and growth of faults: an experimental study. J. Struc. Geol. **4**, 413-430.

Das, S. & Scholz, C. H. 1981. Theory of time-dependent rupture in the earth. J. Geophys. Res. **86**, 6039-6051.

Davy, P., Sornette, A & Sornette, D. 1992. Experimental discovery of scaling laws relating fractal dimensions and the length distribution exponent of fault systems. Geophys. Res. Letts. **19**, 361-363.

Delaney, P. T., Pollard, D. D., Ziony, J. I. & McKee, E. H. 1986. Field relations between dykes and joints: emplacement processes and paleostress analysis. J. Geophys. Res. **91**, 4920-4938.

Einarsson, P. 1991. Earthquakes and present-day tectonism in Iceland. Tectonophysics. **189**, 261-279.

Einarsson, P. and Brandsdöttir, B. 1980. Seismological evidence for lateral magma intrusion during the July 1978 deflation of the Krafla volcano in NE Iceland. J. Geophys. **47**, 160-165.

Engelder, T. 1987. Joints and shear fractures in rock. In: Fracture mechanics of rock (edited by Atkinson, B. K.). Academic Press, London, 27-69.

Etheridge, M. A. 1983. Differential stress magnitudes during regional deformation and metamorphism: upper bound imposed by tensile fracturing. Geology. **11**, 231-234.

Evans, A. G. 1972. A method for evaluating the time-dependent failure characteristics of brittle materials - and its application to polycrystalline alumina. J. Mats. Science. 7, 1137-1146.

Feder, J. 1988. Fractals. Plenum Press.

Freiman, S. W. & Swanson, P. L. 1990. Fracture of polycrystalline ceramics. In: Deformation processes in minerals, ceramics and rocks, (edited by Barber, D. J. & Meredith, P. G.). Unwin Hyman, London.

Fuller, E. R. 1979. An evaluation of double torsion testing - Analysis. In : Fracture mechanics applied to brittle materials, ASTM, STP **678**, 3-18.

Griffith, A. A. 1920. The phenomenon of rupture and flow in solids. Phil. Trans. R. Soc. London, Ser. A. **221**, 163-198.

Gordon, J. E. 1976. The new science of strong materials. Penguin, London.

Gudmundsson, A. 1987. Geometry, formation and development of tectonic fractures on the Reykjanes Peninsula, southwest Iceland. Tectonophysics. **139**, 295-308.

Gutenberg, B. & Richter, C. F. 1954. Seismicity of the earth and associated phenomina. 2nd Ed. Princeton University Press, Princeton.

Hancock, P. L. 1985. Brittle microtectonics: principles and practice. J. Struc. Geol. **7**, 437-457.

Hauksson, E. 1983. Episodic rifting and volcanism at Krafla in North Iceland: growth of large ground fissures along the plate boundary. J. Geophys. Res. **88**, 625-636.

Heffer, K. J. & Bevan, T. G. 1990. Scaling relationships in natural fractures - data, theory and applications. Society of Petroleum Engineers. SPE 20981.

Henderson, J., Main, I. G., Meredith, P. G. & Sammonds, P. R. 1992. The evolution of seismicity at Parkfield: observation, experiment and a fracture mechanical interpretation. J. Struc. Geol. **14**, 905-913.

Howard, K. A., Aaron, J. M., Brabb, E. E., Brock, M. R. et al. 1978. Preliminary map of young faults in the United States as a guide to possible fault activity. U. S. Geol. Surv. MF-916.

Hirata, T. 1989. Fractal dimension of fault systems in Japan: fractal structure in rock fracture at various scales. Pure Appl. Geophys. **131**, 157-170.

Ingraffea, A. R. 1987. Theory of crack initiation and propagation in rock. In: Fracture mechanics of rock (edited by Atkinson, B. K.). Academic Press, London, 71-110.

Irwin, G. R. 1958. Fracture. In: Handbüch der Physik, (edited by Flügge, S.), Vol. 6. Springer, Berlin.

Jaeger, J. C. & Cook, N. G. W. 1979. Fundamentals of rock mechanics. Third edition, Chapman and Hall, London.

Jóhannesson, H. & Saemundsson, K. 1989. Geological map of Iceland, 1:5000 000, Bedrock Geology, Icelandic Museum of Natural History and Icelandic Geodetic Survey, Reykjavik.

Kanamori, H. 1978. Quantification of earthquakes. Nature. **271**, 411-414.

Kanamori, H. & Anderson, D. L. 1975. Theoretical bases of some empirical relations in seismology. Bull. Seis. Soc. Am. **65**, 1073-1095.

Kerrich, R., La Tour, T. E. & Barnet, R. L. 1981. Mineral reactions participating in intragranular fracture propagation: implications for stress corrosion cracking. J. Struc. Geol. **3**, 77-87.

Kies, J. A. & Clark, A. B. J. 1969. Fracture propagation rates and times to fail following proof stress in bulk glass. In: Fracture (edited by Pratt, P. L.). Chapman and Hall, London, 483-491.

King, G. C. P. 1983. The accommodation of large strains in the upper lithosphere of the earth and other solids by self-similar fault systems: the geometrical origin of b-value. Pure Appl. Geophys. **121**, 761-815.

King, G. & Cisternas, A. 1991. Do little things matter? Nature. **351**, 350.

Kranz, R.L. 1983. Microcracks in rocks: a review. Tectonophysics. **100**, 449-480.

Labuz, J. F., Shah, S. P. & Dowding, C. H. 1985. Experimental analysis of crack propagation in granite. Int. J. Rock Mech. Min. Sci. & Geomech. Abstr. **22**, 85-98.

Lama, R.D. & Vutukuri, V. S. 1978. Handbook on mechanical properties of rocks - Volume II. Trans Tech Publs, Germany.

Lambe, C. G. 1967. Statistical methods and formulae. English University Press. London.

Lawn, B. R. & Wilshaw, T. R. 1975. Fracture of brittle solids. Cambridge University Press, Cambridge.

Main, I. G. 1988. Prediction of failure times in the earth for a time-varying stress. Geophys. J. **92**, 455-464.

Main, I. G. 1991. A modified Griffith criterion for the evolution of damage with a fractal distribution of crack lengths: application to seismic event rates and b-values. Geophys. J. Int. **107**, 353-362.

Main, I. G. 1992. Earthquake scaling. Nature. **357**, 27-28.

Main, I. G. & Burton, P. W. 1986. Long term earthquake recurrence constrained by tectonic seismic moment release rates. Bull. Seis. Soc. Am. **76**, 297-304.

Main, I. G., Meredith, P. G. & Jones, C. 1989. A reinterpretation of the precursory seismic b-value anomaly using fracture mechanics. Geophys. J. **96**, 131-138.

Main, I. G., Meredith, P. G., Sammonds, P. R. and Jones, C. 1990. Influence of fractal flaw distributions on rock deformation in the brittle field. In: Deformation mechanisms, rheology and tectonics (edited by Knipe, R. J. & Rutter, E. H.). Spec. Publ. Geol. Soc. Lon. **54**, 81-96.

Mandelbrot, B. B. 1982. The fractal geometry of nature. W. H. Freeman, San Francisco.

Marret, R. & Allmendinger, R. W. 1990. Kinematic analysis of fault slip data. J. Struc. Geol. **12**, 973-986.

Marret, R. & Allmendinger, R. W. 1991. Estimates of strain due to brittle faulting: sampling of fault populations. J. Struc. Geol. **13**, 735-738.

Mastin, L. M. & Pollard, D. D. 1988. Surface deformation and shallow dyke intrusion processes at Inyo Craters, Long Valley, California. J. Geophys. Res. **93**, 13,221-13,235.

Matsumoto, N., Yomogida, K. & Honda, S. 1992. Fractal analysis of fault systems in Japan and the Philippines. Geophys. Res. Letts. **19**, 357-360.

Meredith, P. G. 1983. A fracture mechanics study of experimentally deformed crustal rocks. Unpublished Ph.D. thesis, University of London.

Meredith, P. G. 1990. Fracture and failure of brittle polycrystals: an overview. In: Deformation processes in minerals, ceramics and rocks, (edited by Barber, D. J. & Meredith, P. G.). Unwin Hyman, London.

Meredith, P. G. & Atkinson, B. K. 1983. Stress corrosion and acoustic emission during tensile crack propagation in Whin Sill dolerite and other basic rocks. Geophys. J. R. astr. Soc. **75**, 1-21.

Meredith, P. G. & Atkinson, B. K. 1985. Fracture toughness and subcritical crack growth during high-temperature tensile deformation of Westerly granite and Black gabbro. Phys. Earth Planetary Ints. **39**, 33-51.

Meredith, P. G., Main, I. G. & Jones, C. 1990. Temporal variations in seismicity during quasi-static and dynamic rock failure. Tectonophysics. **175**, 249-268.

Michalske, T. A. & Freiman, S. W. 1982. A molecular interpretation of stress corrosion in silica. Nature. **295**, 511-512.

Nur, A. 1982. The origin of tensile fracture lineaments. J. Struc. Geol. **4**, 31-40.

Opheim, J. A. and Gudmundsson, A. 1989. Formation and geometry of fractures, and related volcanism, of the Krafla fissure swarm, northeast Iceland. Geol. Soc. Am. Bull. **101**, 1608-1622.

Okubo, P. G. & Aki, K. 1987. Fractal geometry in the San Andreas fault system. J. Geophys. Res. **92**, 345-355.

Outwater, J.O. & Gerry, D. J. 1966. On the fracture energy of glass. Vermont Univ. Burington. NONR 3219(01)(X).

Pacheco, J. F., Scholz, C. H. & Sykes, L. R. 1992. Changes in frequency-size relationship from small to large earthquakes. Nature. **355**, 71-73.

Paterson, M. S. 1978. Experimental rock deformation- the brittle field. Springer-Verlag, Berlin.

Pattison, D. & Harte, B. 1985. A petrogenic grid for pelites in the Ballachulish and other Scottish thermal aureoles. J. Geol. Soc. Lond. **142**, 7-28.

Pletka, B. J., Fuller, E. R. & Koepke, B. G. 1979. An evaluation of double torsion testing - experimental. In: Fracture mechanics applied to brittle materials, ASTM STP 678, 19-37.

Pollock, A. A. 1988. Practical guide to acoustic emission. In: LOCAN-AT Handbook. Physical Acoustics Corp., U.S.A.

Raju, K. R. 1981. Effect of depth of side grooves in double torsion specimens on plane strain fracture toughness. Int. J. Fracture. R189-R190.

Ramsay, J. G. & Huber, M. I. 1987. The techniques of modern structural geology. Vol. 2: folds and fractures. Academic Press, London.

Read, H. H. 1961. Aspects of Caledonian magmatism in Britain. Liv. Manchr. Geol. J. 2, 653-683.

Richter, C. F. 1958. Elementary seismology. Freeman, San Francisco.

Saemundsson, K. 1974. Evolution of the axial rifting zone in Northern Iceland and the Tjörnes Fracture Zone. Geol. Soc. Am. Bull. 85, 495-504.

Saemundsson, K. 1978. Fissure swarms and central volcanoes of the neovolcanic zones of Iceland. In: Crustal evolution in NW Britain and adjacent regions, (edited by Bowes, D. R. & Leake, B. E.). Seel House Press, Liverpool.

Sano, O. 1988. A revision of the double torsion technique for brittle materials. J. Mats. Science. 23, 2525-2511.

Scholz, C. H. 1968a. Mechanism of brittle creep in rock. J. Geophys. Res. 73, 3295-3302.

Scholz, C. H. 1968b. The frequency-magnitude relation of microfracturing in rock and its relation to earthquakes. Bull. Seism. Soc. Am. 58, 399-415.

Scholz, C. H. 1982. Scaling laws for large earthquakes: consequences for physical models. Bull. Seis. Soc. Am. 72, 1-14.

Scholz, C. H. 1990. The mechanics of earthquakes and faulting. Cambridge University Press, Cambridge.

Scholz, C. H. & Cowie, P. A. 1990. Determination of geologic strain from fault slip data. Nature. **346**, 837-839.

Scholz, C. H., Sykes, L. R. & Aggarwal, Y. P. 1973. Earthquake prediction: a physical basis. Science. **181**, 803-809.

Segall, P. 1984. Formation and growth of extensional fracture sets. Geol. Soc. Am. Bull. **95**, 454-462.

Segall, P. & Pollard, D. D. 1983. Joint formation in the granitic rock of the Sierra Nevada. Geol. Soc. Am. Bull. **94**, 563-575.

Shaw, H. R. & Gartner, A. E. 1986. On the graphical interpretation of palaeoseismic data. United States Geological Survey Open File Report. 86-394.

Sigurdsson, O. 1980. Surface deformation of the Krafla Fissure Swarm in two rifting events. J. Geophys. **47**, 154-159.

Simmons, G. & Richter, D. 1976. Microcracks in rocks. In: The physics and chemistry of minerals and rocks, (edited by Strens, R. G. J.). Wiley, New York.

Sornette, A., Davy, P. & Sornette, D. 1990. Growth of fractal fault patterns. Phys. Rev. Letts. **65**, 2266-2269.

Strecheisen, A. L. 1967. Classification and nomenclature of igneous rocks. Neues Jahrb. Mineral. Abhandlungen. **107**, 144-214.

Swanson, P. L. 1984. Subcritical crack growth and other time- and environment-dependent behavior in crustal rocks. J. Geoph. Res. **89**, 4137-4152.

Swanson, P. L. 1987. Tensile fracture resistance mechanisms in brittle polycrystals: an ultrasonics and in situ microscopy investigation. J. Geophys. Res. **92**, 8015-8036.

Tchalenko, J. S. 1970. Similarities between shear zones of different magnitudes. Geol. Soc. Am. Bull. **81**, 1625-1640.

Tryggvason, E. 1984. Widening of the Krafla Fissure Swarm during the 1975-1981 volcano-tectonic episode. Bull. Volcanol. **47**, 47-69.

Turcotte, D. L. 1989. Fractals in Geology and Geophysics. Pure Appl. Geophys. **131**, 171-196.

Turner, F. J. & Weiss, L. E. 1963. Structural analysis of metamorphic tectonites. McGraw-Hill, New York.

Vignes-Adler, M., Le Page, A. & Adler, P. M. 1991. Fractal analysis of fracturing in two African regions, from satellite imagery to ground scale. Tectonophysics. **196**, 69-86.

Walsh, J. & Watterson, J. 1988. Analysis of the relationship between displacements and dimensions of faults. J. Struc. Geol. **10**, 239-247.

Walsh, J., Watterson, J. & Yielding, G. 1991. The importance of small scale faulting in regional extension. Nature. **351**, 391-393.

Wiederhorn, S. M. 1973. Subcritical crack growth in ceramics. In: Fracture mechanics of ceramics, Volume II (edited by Bradt, R. C., Hasselman, D. P. H. & Lange, F. F.). Plenum Press, New York, 613-646.

Williams, D. P. & Evans, A. G. 1973. A simple method for studying slow crack growth. J. T. Eval. **1**, 264-270.

Williams, R. G. B. 1986. Intermediate Statistics for Geographers and Earth Scientists. London, Macmillan.

Wise, D. U. 1964. Microjointing in basement, Middle Rocky Mountains of Montana and Wyoming. Geol. Soc. Am. Bull. **75**, 287-306.

Appendix A Specimen collection and preparation

The experimental program reported here was carried out on two types of crystalline rock. These were: (1) the fine-grained Loch Uisg microgranodiorite; and (2) the slightly coarser-grained Ballachulish granite, both from North West Scotland. The difference in grain size provided the opportunity to determine any possible effects of specimen size on the test results, since the specimen dimensions are dependent upon and scaled with the grain size, (see section 2.1.2).

A.1 Test materials

Loch Uisg microgranodiorite

The fine grained test material chosen was the green-grey Loch Uisg microgranodiorite of Tertiary age from the Isle of Mull, North West Scotland. The samples were collected from an exposure on the south eastern shore of Loch Buie in the south of the island (grid reference: NM 6223). The granodiorite is intruded into the Plateau and Central Group of Mull lavas (Bailey et al., 1924), and is unaffected by the tectonic activity which folded the surrounding country rock in an earlier phase of deformation. The exposure of granodiorite on the shore of Loch Buie is cut by several sets of subvertical, subparallel joints. At several localities the joints are closely spaced (1.5 cm apart) with a trend of 118°. At other localities, the joints are more widely spaced (16 - 45 cm) with a trend of 096°. It is probable that these are cooling joints. The test specimens were collected as blocks from between the wider spaced joints.

The rock consists of acicular augite, now altered to chlorite, plagioclase (albite) and orthoclase, in a micrographic groundmass containing only a small proportion of quartz. The average grain size of the groundmass is less than 0.5 mm with phenocrysts of up to 1 mm, requiring a specimen thickness of approximately 5 mm, and a width of 60 mm for the design criteria of the double torsion test specimens, as described section 2.1.2. The rock does not show any visible tectonic fabric in either hand specimen or thin section.

Ballachulish granite

The relatively coarser grained rock type was the black and white Ballachulish 'granite' of Devonian age from North West Scotland, classified as a Newer Granite of the Caledonian Orogen by Read (1961). The 'granite' is intruded into Lower Dalradian metasediments. The intrusion shows no post-emplacement tectonic fabric (Pattison and Harte, 1985). The granite may be divided into two phases, an outer tonalite/quartz diorite zone which is cross cut by a central pink granite/quartz monzonite (Strecheisen, 1967). The test samples were collected from a quarry north east of Kentallen (grid reference: NN0259) from the outer tonalite zone. The rock samples collected contained some small (average 20 mm diameter) xenoliths of sedimentary and igneous origin, but these were specifically avoided when preparing the test specimens.

The rock consists of plagioclase (andesine), biotite, hornblende and subordinate microcline and quartz. The average grain size of the samples of Ballachulish granite collected is 1-2 mm, requiring a larger test specimen of thickness 6.5 mm, and width 80 mm. The rock does not show any tectonic fabric in either hand specimen or thin section.

A.2 Specimen preparation

Several stages were necessary in the preparation of the double torsion test specimen that is illustrated in figure 2.1(a):

1. The oriented samples collected from the field were cut into slices slightly thicker than the required size, using a diamond edged Clipper saw (at the University of Edinburgh).

2. Each slice was then ground down to the required thickness, with a parallelism of 0.01 to 0.02 mm across each specimen surface, using the Abwood surface grinder (at U.C.L., London) with diamond edged grinding wheel.

3. One side of each specimen was then lapped for approximately 7 hours on a Vibrolap (Highland Park 27") using 600 grit silicon carbide, and polished for a further 7 hours using Highland Park rapid polish.

4. A groove was then cut into the unpolished surface of each specimen using a small pedestal grinding machine (the Herbert Junior surface grinder, at U.C.L.) fitted with a 2 mm wide diamond wheel, ensuring that the groove was central and parallel to the sides of the length of the specimen. The groove was cut to 1/3 thickness of the specimen (each measured individually).

5. A notch was cut in the centre of the groove at one end of each specimen using a 0.5 mm wide diamond wheel to a depth of approximately 10 mm on the polished surface.

6. Finally each specimen was then washed with ordinary detergent, rinsed in water and then dried in an oven at not more than 65-70°C for at least 24 hours. The temperature was not raised above 75-80°C, since thermal cracking occurs in these rocks above this temperature.

7. Several specimens were photographed before testing to ensure the absence of any pre-existing small scale fractures.

Appendix B Summary of results

This appendix consists of three tables containing complete data sets from the experimental program carried out during this study. In all the tables the results from tests on the granodiorite and granite specimens are given separately. The test number refers to the number assigned to the test and specimen during the experimental program.

Table B.1

This table gives the experimental data and fracture mechanics results.

Column 1: the reference number assigned to the test and specimen. This column also indicates the environmental conditions active at the crack tip, i.e. 'dry', 'damp' or 'wet'.

Column 2: the displacement rate is the constant rate at which the loading ram was operated during the entire test.

Column 3: the time interval is the total time (in seconds) during which the test showed an approximately constant load.

Column 4: the average load (in Newtons) is the average load operating on the specimen during this time interval. Column 5 gives the standard error on the average load, (this is the measure of confidence in that value of the average load, not a measure of standard deviation).

Column 6: the stress intensity factor K_I for the time interval of constant load, calculated using equation (2.3)

Column 7: the rupture velocity V, calculated using equation (2.6).

The boxes indicate tests that were run at the same displacement rate in the same environmental conditions. Tests were repeated on different specimens to check the repeatability of test conditions and results.

Table B.1 Experimental data and fracture mechanics results

Granodiorite

1	2	3	4	5	6	7
Test	displ rate $x10^{-6}ms^{-1}$	time interval (s)	Average load (N)	SE Load	K_I MPa $m^{1/2}$	V $x10^{-6}ms^{-1}$
Dry						
0022	0.016	2160	207.87	0.20	1.9	6.9
0104	0.016	3307	195.88	0.11	1.98	7.4
0102	0.05	1731	186.81	0.11	1.87	24.0
0006	0.16	1002	219.65	0.498	2.25	66.0
0007	0.16	288	255.94	0.12	2.39	56.8
0101	0.16	394	219.06	0.14	1.79	66.0
0024	1.6	107.7	216.68	0.18	2.52	670.0
0055	1.6	40	255.84	0.21	2.25	568.0
0110	1.6	37	226.31	0.16	2.07	640.0
0111	5.0	11	248.56	0.20	2.34	1820.0
Damp						
0052	1.6	88	205.65	0.31	1.98	707.0
Wet						
0051	0.016	9493	206.57	0.52	1.86	7.04
0118	0.05	2945.1	213.15	0.72	1.87	21.3
0028	0.16	1555	232.19	0.77	2.05	62.6
0117	0.16	924	162.80	0.44	2.04	89.0
0037	0.5	270	255.05	0.56	2.13	170.0

1	2	3	4	5	6	7
test	displ rate	time interval	Average	SE Load	K_I	V
	$x10^{-6}ms^{-1}$	(s)	load (N)		MPa $m^{½}$	$x10^{-6}ms^{-1}$
Wet	cont...					
0035	1.6	60	219.58	0.51	1.97	660.0
0036	1.6	105	227.74	0.55	1.96	638.0
0040	1.6	63	262.95	1.14	2.22	550.0
0116	1.6	38	228.40	0.54	2.12	637.0
0041	5.0	32	255.92	0.46	2.23	1770.0
0119	5.0	31	186.25	0.49	2.08	2440.0

Granite

1	2	3	4	5	6	7
Test	displ rate	time interval	Average	SE Load	K_I	V
	$x10^{-6}ms^{-1}$	(s)	load (N)		MPa $m^{½}$	$x10^{-6}ms^{-1}$
Dry						
0122	0.16	269	191.37	0.15	1.41	42.8
0123	1.6	40	171.41	0.27	1.24	478.0
0128	5.0	24.5	244.81	0.17	1.71	1047.0
Wet						
0125	0.5	1907	195.39	0.85	1.46	131.0
0126	1.6	52	200.18	0.54	1.41	409.0
0127	5.0	29	211.51	0.47	1.53	1210.0

Table B.2

This table contains details of the acoustic emission data monitored during the time interval of constant load and results of AE analysis.

Column 1: as table B.1.

Column 2: the experimental threshold (E. T.) operating during the test to cut out background noise. F signifies that an active high pass filter was operative during the test.

Column 3: the initial amplitude cut-off value, a_{c1} (dB), used to calculate the AE b-value of the test (given in column 4) from equation (3.1). Column 5 gives the error, σ_b, at the 90% confidence limit (two standard errors), (equation 3.2). Column 6 gives the number, N, of AE events of an amplitude above a_c that were monitored during the time interval of constant load (column 3 of table B.1) and used to calculate the b-value.

Column 7: the variable cut-off a_{c2} ; two main values were used, 37.5 dB for the dry tests and 48.5 dB for the wet tests. This was to uniform the data as much as possible, whilst using the maximum available data. Column 8 gives the b-value, $b(a_{c2})$, calculated using the variable cut-off. Columns 9 and 10 give the error and number of events (as in columns 5 and 6) for $b(a_{c2})$.

Table B.2 Results of AE analysis

Granodiorite

1	2	3	4	5	6	7	8	9	10
Test	E.T. (dB)	a_{c1} (dB)	b (ac_1)	σ_b	N (a_{c1})	a_{c2} (dB)	b (a_{c2})	σ_b	N(a_{c2})
Dry									
0022	31	32.5	1.31	0.10	626	37.5	1.41	0.16	295
0104	29	30.5	1.21	0.02	8831	37.5	1.31	0.04	3379
0102	29	30.5	1.23	0.02	6914	37.5	1.35	0.05	2562
0006	29	30.5	1.40	0.13	433	37.5	1.61	0.26	143
0007	29	33.5	1.38	0.06	1589	37.5	1.32	0.09	813
0101	37	37.5	1.18	0.05	1844	37.5	1.26	0.09	627
0024	40	41.5	1.12	0.04	2314	-	-	-	-
0055	37	37.5	1.19	0.08	802	-	-	-	-
0110	35	35.5	1.19	0.06	1167	37.5	1.25	0.08	924
0111	37	37.5	1.06	0.05	1391	-	-	-	-
Damp									
0052	39	40.5	1.42	0.11	652	48.5	1.59	0.22	189
Wet									
0051	45	46.5	1.77	0.32	111	48.5	1.95	0.42	81
0118	41 F	40.5	1.79	0.34	106	48.5	1.96	0.73	27
0028	46	46.5	1.69	0.28	137	48.5	1.61	0.33	90
0117	41 F	40.5	1.75	0.31	121	-	-	-	-
0037	47	47.5	2.10	0.39	110	48.5	1.99	0.43	82
0035	43	43.5	1.23	0.15	256	48.5	1.24	0.21	125

1	2	3	4	5	6	7	8	9	10
Test	E.T. (dB)	a_{c1} (dB)	b (ac_1)	σ_b	N (a_{c1})	a_{c2} (dB)	b (a_{c2})	σ_b	N(a_{c2})
Wet	cont.								
0036	47	48.5	1.84	0.31	130	-	-	-	-
0040	47	47.5	1.94	0.53	50	48.5	1.62	0.54	34
0116	42 F	42.5	1.29	0.25	99	48.5	1.43	0.41	45
0041	47	48.5	1.42	0.19	197	-	-	-	-
0119	41 F	41.5	1.55	0.24	148	48.5	1.85	0.55	42

Granite

1	2	3	4	5	6	7	8	9	10
Test	E.T. (dB)	a_{c1} (dB)	b (ac_1)	σ_b	N (a_{c1})	a_{c2} (dB)	b (a_{c2})	σ_b	N(a_{c2})
Dry									
0122	38	39.5	1.07	0.04	1839	-	-	-	-
0123	38	38.5	1.25	0.08	901	-	-	-	-
0128	38	40.5	1.05	0.03	3006	-	-	-	-
Wet									
0125	41 F	41.5	2.43	0.62	59	-	-	-	-
0126	50	50.5	1.68	0.26	157	-	-	-	-
0127	41 F	41.5	1.78	0.34	103	-	-	-	-

Table B.3

This table lists the structural results from the 'fractal' analysis of the fracture patterns from the test specimens, and also acts as a summary table of results by inclusion of the AE b-value and its standard error (at the 66% confidence limit) (columns 6 and 7) and the normalised stress intensity K_I / K_{IC} (column 8).

Column 1: as table B.1.

Column 2: L_{min} is the lower microfracture length limit used in determining the power-law length distribution exponent D.

Column 3: the exponent D, and its standard error (column 4), were calculated using equations (C.3) and (C.4) respectively.

Column 5: N (D) is the number of microfractures used in the calculation, i.e. only those with a length greater than L_{min}.

The results surrounded by boxes indicate multiple structural analyses of several fracture patterns from the same specimen. Test#*tot indicates the length distribution result obtained by combining the crack lengths measured in all the fracture patterns from that specimen, (see appendix E).

Table B.3 Results of structural analysis

Granodiorite

1	2	3	4	5	6	7	8
Test	L_{min} (microns)	D	SED	N (D)	b (a_{c2})	SEb	K_I / K_{IC}
Dry							
0022	56.2	1.16	0.14	70	1.41	0.08	0.65
0102#1	44.6	1.49	0.16	126	1.35	0.02	0.64
0102#2	44.67	1.56	0.15	126	"	"	"
0102#3	22.38	1.07	0.20	119	"	"	"
0102#4	56.2	1.23	0.15	92	"	"	"
0102#5	31.62	1.34	0.04	145	"	"	"
0102#6	44.67	2.03	0.05	116	"	"	"
0102#7	44.67	1.28	0.16	110	"	"	"
0102tot	44.67	1.54	0.07	780	"	"	"
0006	44.6	1.42	0.22	98	1.61	0.13	0.77
0024	44.6	1.02	0.13	91	1.12	0.02	0.87
0055#1	44.6	1.38	0.12	226	1.19	0.04	0.77
0055#2	35.5	1.31	0.21	141	"	"	"
0055tot	44.67	1.41	0.08	353	"	"	"
Wet							
0051#1	44.6	1.56	0.18	103	1.95	0.21	0.64
0051#2	44.6	1.71	0.16	131	"	"	0.64
0051#3	28.18	1.78	0.18	189	"	"	"
0051#4	28.18	1.52	0.17	209	"	"	"
0051tot	28.18	1.71	0.12	712	"	"	"

1	2	3	4	5	6	7	8
Test	L_{min} (microns)	D	SED	N (D)	b (a_{c2})	SEb	K_I/K_{IC}
Wet	cont...						
0028	44.6	1.24	0.17	131	1.61	0.16	0.71
0037	28.18	1.66	0.21	177	1.99	0.21	0.73
0035	44.6	1.06	0.11	69	1.24	0.1	0.68
0036	56.2	1.37	0.21	104	1.84	0.15	0.67
0041#1	28.18	1.15	0.16	123	1.42	0.09	0.77
0041#2	28.18	1.32	0.13	118	"	"	"
0041#3	44.6	1.85	0.22	91	"	"	"
0041#4	28.18	1.51	0.14	154	"	"	"
0041tot	28.18	1.63	0.12	530	"	"	"

Granite

1	2	3	4	5	6	7	8
Test	L_{min} (microns)	D	SED	N (D)	b (a_{c2})	SEb	K_I/K_{IC}
Dry							
0122	223.8	1.74	0.23	108	1.07	0.02	0.70
0123	223.8	1.45	0.09	96	1.25	0.04	0.62
0128	223.8	1.45	0.20	100	1.05	0.01	0.85
Wet							
0125	233.8	1.79	0.18	151	2.43	0.31	0.73
0126	223.8	2.25	0.21	124	1.68	0.13	0.71
0127	223.8	2.00	0.15	289	1.78	0.17	0.76

Appendix C Statistical methodology

C.1 Constant load calculation

The load data recorded by the LOCAN-AT may be obtained from the data file in two ways. If the test lasted longer than about 30 seconds, a mean load may be calculated at a set period of time, for example every 5 or 10 seconds. An average mean load for the time interval of approximately constant load may then be calculated by the usual method (where $L = \sum L/n$). However, if the test lasted less than 30 seconds, this method would produce very few data points, and an alternative method is to use the load data recorded for each AE event monitored. This method calculates a time-weighted mean load L from the following equation:

$$\bar{L} = \sum_{n_i=1}^{n_i=n} \left(\frac{W_n \bar{L_n}}{t_n} \right) \qquad (C.1)$$

where n is the number of time intervals, of time t, between recorded events, W_n is the weighting factor ($W_n = t_n - t_{n-1}$), $\bar{L}_n$ is the mean load of that interval ($\bar{L}_n = (L_n + L_{n-1})/2$) (Lambe, 1967). The standard error SE is given by:

$$SE = \left(\frac{\sum_{n_i=1}^{n_i=n} \left(W_n \left(\bar{L_n} - \bar{L} \right)^2 \right)}{(n-1)(t_n - t_0)} \right)^{0.5} \qquad (C.2)$$

where t_0 is the initial time (Lambe, 1967).

C.2 Reduced major axis method to calculate a gradient

The usual method to calculate a gradient or 'best fit' line between two sets of data is the least squares method. However, this method assumes that one data set is varying dependant upon the other which is measured to a high accuracy. In most of the data in this thesis, both data sets are subject to errors of measurement. Therefore, the reduced major axis method is the most suitable to find the gradient of the 'best-fit' line to the data. In this method the gradient is given by:

$$\text{gradient} = \frac{\text{stdev}(y)}{\text{stdev}(x)} \qquad \text{(C.3)}$$

where stdev is the standard deviation (Williams, 1986). The standard error SE of this gradient is given by:

$$SE = \text{gradient} . \left(\frac{1 - r^2}{n} \right)^{0.5} \qquad \text{(C.4)}$$

where r is Pearson's product-moment correlation coefficient, and n is the number of data points. The intercept of the reduced major axis is:

$$\text{intercept} = \bar{y} - \text{gradient} . \bar{x} \qquad \text{(C.5)}$$

where $\bar{y}$ is the mean value of the data on the y-axis and $\bar{x}$ is the mean value of the data on the x-axis, (Williams, 1986).

The standard error SE of the intercept (based on bivariate normal theory) is:

$$SE = stdev(y)\left[\left(\frac{1-r^2}{n}\right)\left(1+\frac{\bar{x}^2}{stdev(x)^2}\right)\right]^{0.5}. \qquad (C.6)$$

C.3 'Standard error of goodness of fit' of a classical regression

This method produces a measure of how closely data points are approximated by a best fit line, that is the degree of vertical scatter about the line (Williams, 1986). In this thesis, this method has been used to compare the variation in load data during the time period of linear-elastic behaviour and approximately constant load.

The gradient is given by:

$$gradient = \frac{n\sum(x.y) - \sum x.\sum y}{n\sum x^2 - \left[\sum x\right]^2} \qquad (C.7)$$

where n is the number of points. The intercept is given by:

$$intercept = \frac{\sum y - gradient.\sum x}{n}. \qquad (C.8)$$

The 'standard error of goodness of fit' is then given by:

$$SE = \frac{\sum y^2 - intercept.\sum y - gradient.\sum x.y}{n-2}. \qquad (C.9)$$

Appendix D Details of experimental equipment

The testing machine used in the present series of tests essentially comprised a 10 kN capacity servo-hydraulic actuator mounted on a stiff loading frame, supplied by Servo-technique Ltd. This is illustrated in figure 2.3 and in the photograph of figure D.1.

The specimen locating jig was constructed from aluminium alloy ('Duralumin'), and consisted of an open ended tray, with positioning screws (two on each of three sides). Two grooves on the upper surface of the jig base were positioned a fixed distance apart to provide the semi-moment arm distance between the two rollers on which the specimen was supported and the respective loading point. Two jigs of the same design but different dimensions were constructed to allow testing of the two different specimen sizes. The jig was fixed inside a perspex box to provide the water bath during the 'wet' tests. The jig and box were positioned exactly under the load actuator of the testing machine and fixed in place. Two 'ears' on the loading ram could be lowered precisely down into two vertical grooves machined into the sides of the jig, thus ensuring that the load was applied exactly centrally at one end of the specimen. Figure D.2 shows a photograph of the specimen jig and water bath.

Figure D.3 shows a copy of the calibration certificate issued for the single transducer used in this experimental program, and illustrates the essentially flat response curve between 300 kHz and 1 MHz.

Figure D.1 Photograph of the 10 kN double torsion test machine at University College, London.

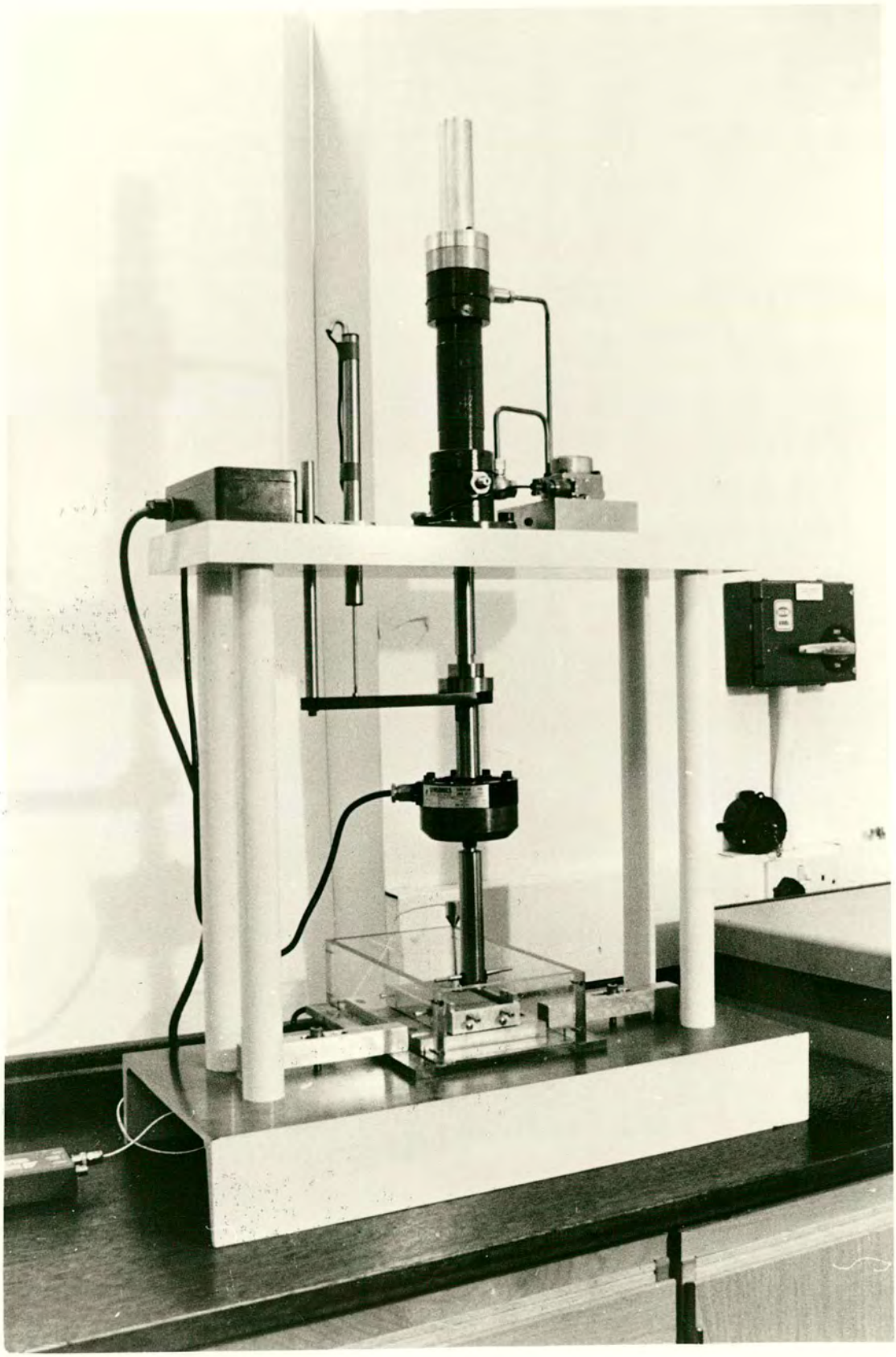

Figure D.2. Photograph of the double torsion specimen jig and water bath.

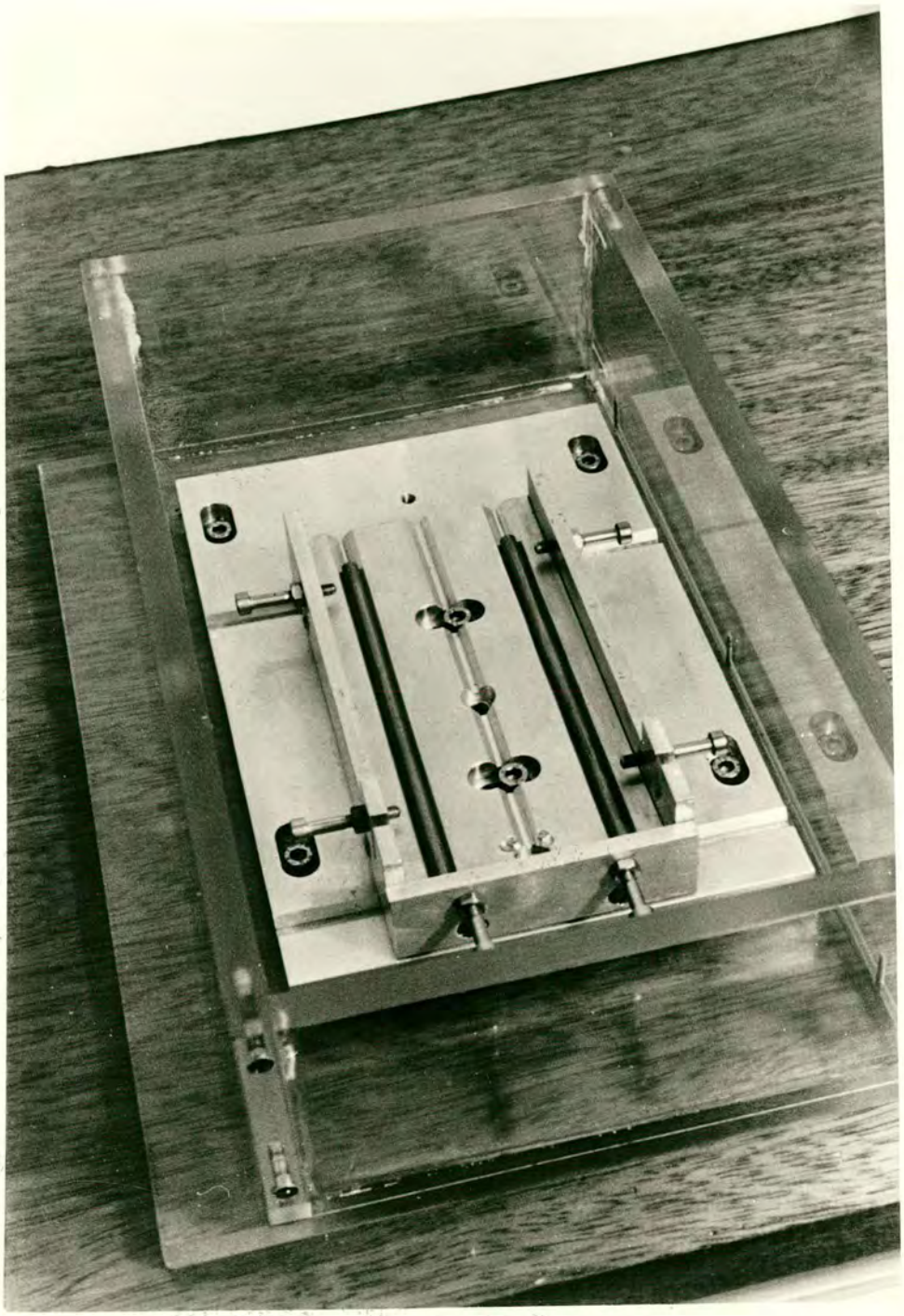

Figure D.3 The calibration certificate issued for the single tranducer used in the present experimental program.

PHYSICAL ACOUSTICS CORPORATION

CALIBRATION CERTIFICATE

DUNEGAN CORPORATION

''Sound Technology for Productivity and Safety''

MODEL NUMBER: WD

DATE: 03/15/89

SERIAL NUMBER: 739

TESTED BY: H.M.

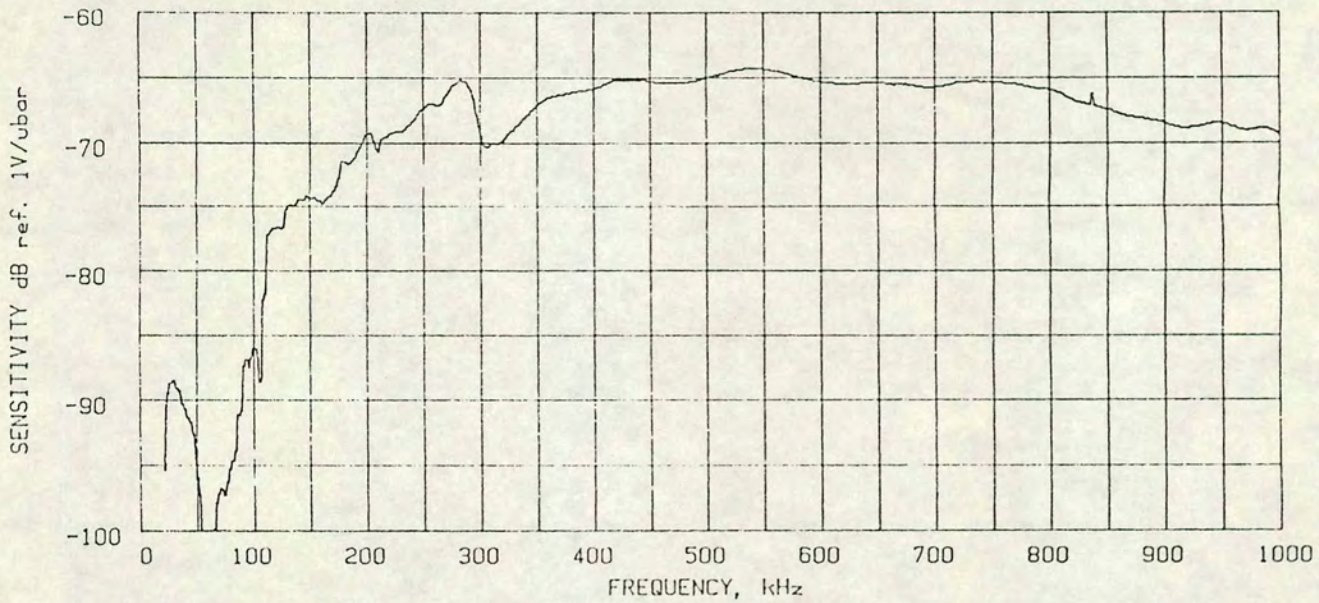

This certifies that this sensor meets all performance environmental, and physical characteristics listed in applicable PAC/DUNEGAN specifications.

Appendix E Method of structural analysis: critique

As described in section 3.2.2, the process of quantitative structural analysis that has been carried out for each test specimen involved measurement of a representative fracture pattern photographed from the specimen. In the case of the fine grained granodiorite specimens, each photographic collage represents just 4.5 - 6 mm along the central third of the specimen length. Due to the extensive amount of time involved in producing each fracture pattern and the subsequent analysis, only one fracture pattern was taken from each specimen to allow examination of a reasonable number of test specimens. In order to test the validity of this sampling method, and to study any possible variation in crack length distribution across a single specimen, several test specimens chosen at random have been examined in greater detail. Two to four fracture patterns were taken from random sites along the main crack in the central third region of each of the chosen specimens, thus replicating the length distribution exponent measurement for those specimens. One specimen (test #0102) was chosen as a test case for an almost complete analysis, the results of which are given below.

Variation in D across a single specimen

Test #0102 was carried out in ambient air-dry conditions, at a loading ram displacement rate of 0.05×10^{-6} ms^{-1}. Seven sets of photographs were taken of areas along the total trace of the main crack, and the fracture patterns traced individually for each area. Length distribution exponents were then calculated for each area (using the method described in section 3.2.2, and the reduced major axis calculation, appendix C). Figure E.1 shows a schematic diagram of the central third region of the specimen. The arrow shows the direction of macrocrack propagation. The seven

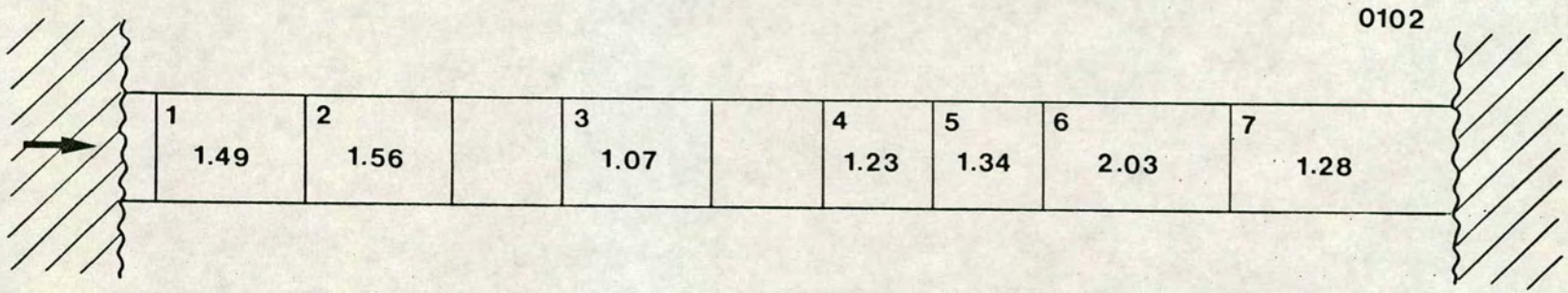

Figure E.1 Schematic diagram of the central third region of specimen #0102.

The arrow indicates the direction of crack propagation. The seven individual areas for which fracture patterns were analysed are marked, together with their individual length distribution exponents.

individual areas for which fracture patterns were analysed are marked, with the relevant length distribution exponent D also shown. D is seen to vary from 1.03 to 2.03, and covers the whole range of possible exponents ($1 < D < 2$, see section 1.2). The only pattern to the variation in D appears to be one of high-low-high-low values.

The most likely explanation for this variation is inhomogeneity of the rock specimen. However, it is possible that fluctuations in the applied load will have affected the growth of the microfractures. Figure E.2(a) shows the load curve for this test, with the limits of the time interval of approximately constant load marked by T_1 and T_2. It is evident that the load was not entirely constant during this time period, even allowing for noise in the signal. A 'standard error of goodness of fit' (see appendix C) to a regression line of the data between T_1 and T_2 gives a value of 86 Newtons, which is relatively high indicating a high level of variation (see section 2.3.2). There appears to be two peaks of high load (h_1 and h_2) followed respectively by two lows (l_1 and l_2). This may be compared to the variation in length distribution, illustrated in figure E.1. The anomalously high length distribution exponents may be correlated approximately to periods where the load is climbing steadily (i.e. just before h_1 and h_2), thus causing slow crack growth and the nucleation of small cracks. The low values of D would be expected to occur at times of high load, and hence high K, where the macrocrack propagates in dynamic spurts. The lows in the load curve (l_1 and l_2) suggest that significant sudden crack growth has increased the specimen compliance, thus causing a drop in load. The period just before the lows in load would then correspond to low values of D. This appears to confirm a relation between variation in load and variation in D.

This may be illustrated further by examination of a test that showed very little variation in applied load over the period of 'constant' load. For example, during test #0051, the load was fairly constant throughout the test, (figure 3.4(a)). A 'standard

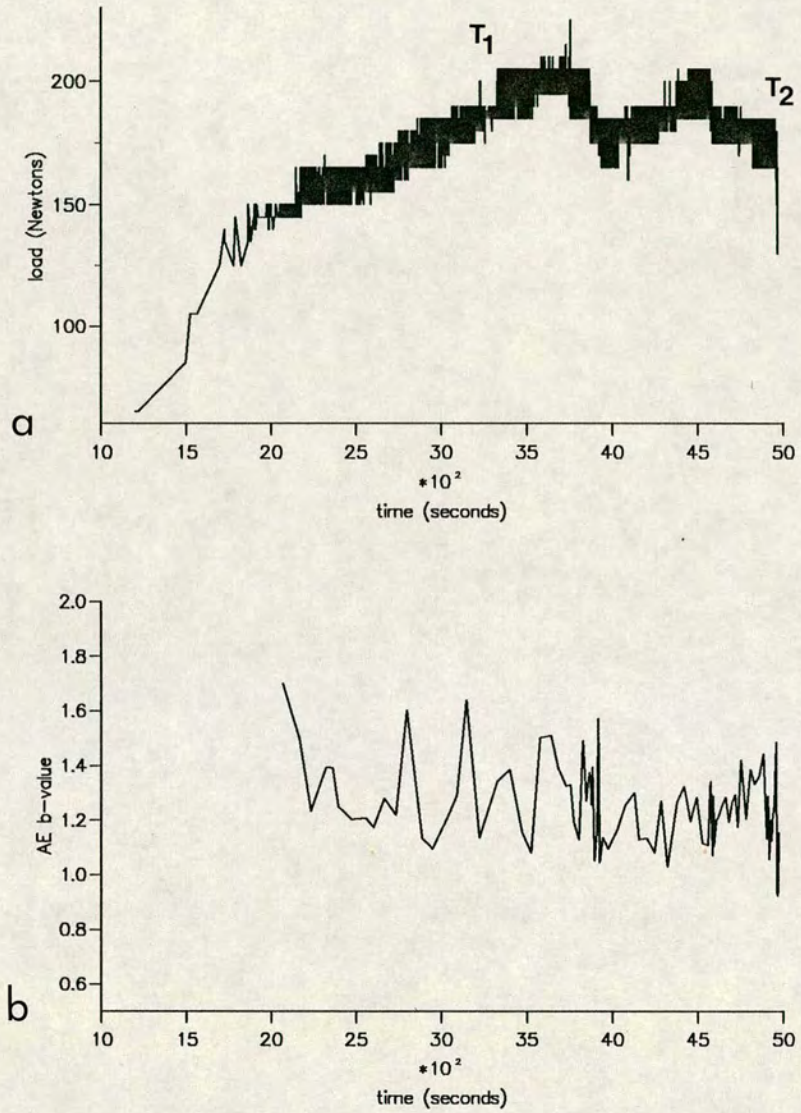

Figure E.2 Data from test #0102.

(a) The load time curve. The limits of the time interval of approximately constant load are marked by T_1 and T_2.

(b) Plot of AE b-value versus time. The b-value is calculated in bins of 75 events.

error of goodness of fit' to this data between T_1 and T_2 gives a value of 45 Newtons, which is relatively low. Photographs were taken from four areas along the trace of the main crack. The individual length distribution exponents obtained from these patterns show a variation of 0.26 in a range from 1.52 to 1.78. This is significantly less than the variation observed in specimen #0102. Therefore, a relatively good constant load appears to produce less variation in D across the specimen.

Figure E.2(b) illustrates the variations in AE b-value in time for test #0102. The b-value calculation used in section 3.1.2 uses all the data from the time interval to produce an 'average' value. It therefore seems appropriate to use all the length distribution data to produce a single length distribution histogram for the specimen. When this is done for specimen #0102, the resulting length distribution exponent is found to be 1.54 ± 0.07, as illustrated in figure E.3. The fractal range covers 1.5 - 2 orders of magnitude, and the increased data set gives a much smoother straight line power-law distribution (and correlation coefficient, $r = -0.98$). The discrete data is also very similar to the cumulative data, until the cumulative data curves off at higher crack lengths in a similar way to the seismic data illustrated in figure 1.12.

Summary

Ideally, the total middle third of the specimen length should be used to obtain a length distribution for each specimen, in order to reflect the structure from the whole specimen and to produce larger more significant data sets. However, due to the limited time available and amount of work involved, this was not possible for each specimen. Multiple analyses of two to four fracture patterns were carried out for several test specimens. This data is given separately in appendix B, together with the combined length distribution exponents obtained from the data of the multiple analyses. The consistancy of the structure across the specimens varies from test to

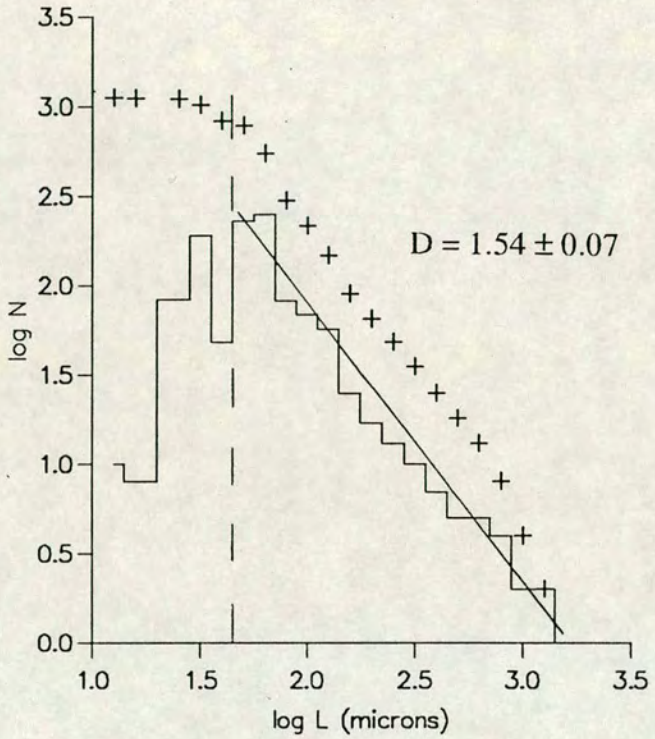

Figure E.3 Length-frequency distribution for the combined microcrack length data from the total central length of specimen #0102. The slope from the discrete data (staircase) gives D = 1.54 ± 0.07 (where the correlation coefficient r = -0.98). The cumulative data (crosses) gives a very similar slope.

test, possibly depending on the inhomogeneity of the rock sample, or the degree of fluctuation in applied load. It has been shown using two examples that the influence of fluctuation in applied load on the structure may be important.

Although the variation in D may seem to be a significant problem, the overall result of the relationship between D and b (figure 4.3) is not totally different if the individual fracture pattern results are plotted instead of the combined results where applicable. Much of the scatter in this diagram may now be attributed to the inevitable problems of small data sets and variations in D across the specimen length as well the inevitable errors in AE b-value. Increased data sets for each specimen, and possibly a systematic rejection of any test results from tests showing very high fluctuation in load during the 'constant load' period, may contribute to a reduction in this scatter.